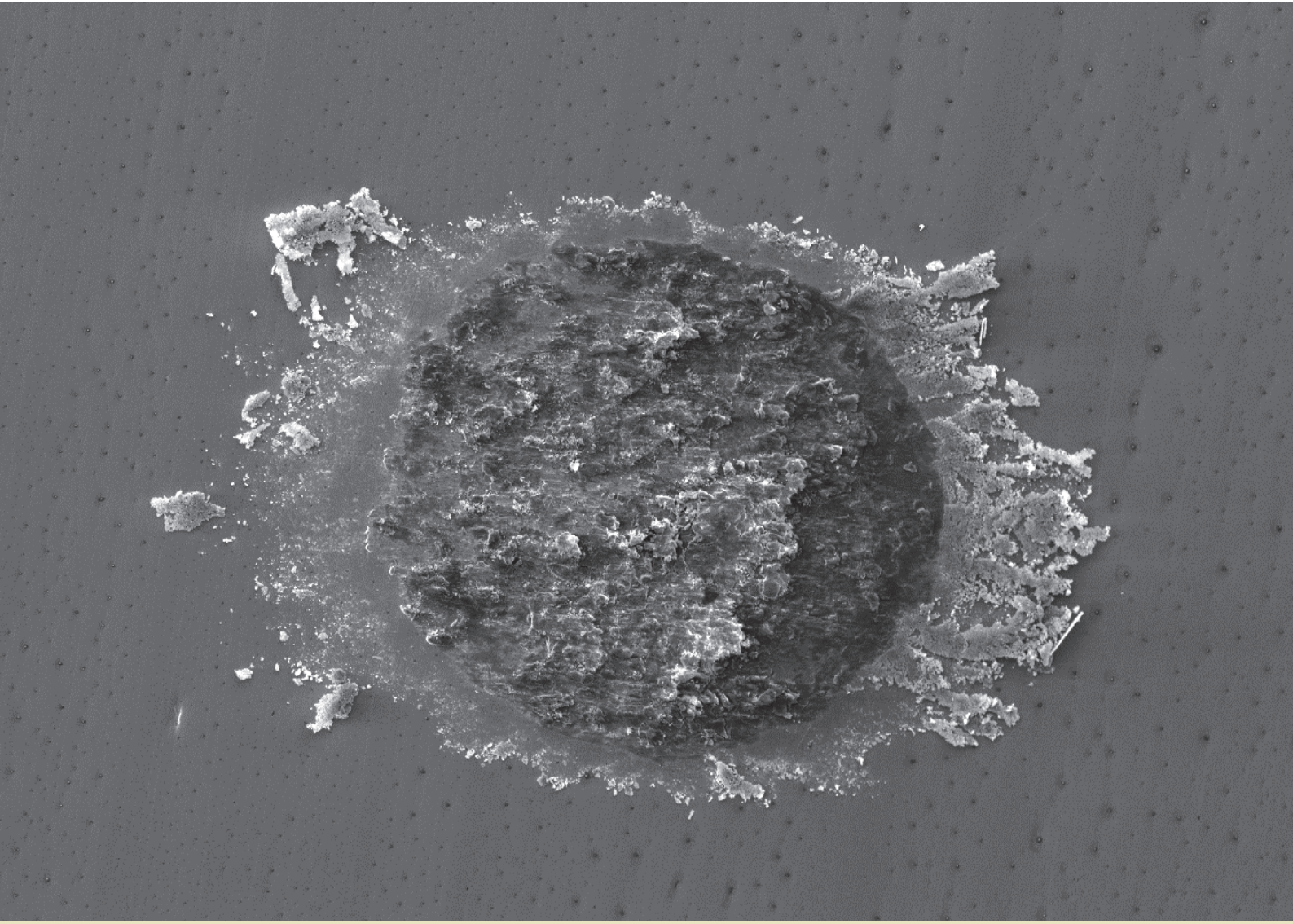

Miguel Alberto Pereira Esteves

STUDY OF FRETTING BEHAVIOUR ON AUTOMOTIVE ELECTRICAL CONTACTS

Doctor of Philosophy Thesis in Mechanical Engineering, Structural Integrity branch, supervised by Professor Amílcar Lopes Ramalho and submitted to the Mechanical Engineering Department of the Faculty of Sciences and Technology of the University of Coimbra

July 2016

· U C ·

Universidade de Coimbra

Miguel Alberto Pereira Esteves

STUDY OF FRETTING BEHAVIOUR ON AUTOMOTIVE ELECTRICAL CONTACTS

Doctor of Philosophy Thesis in Mechanical Engineering, Structural Integrity branch, supervised by Professor Amílcar Lopes Ramalho and submitted to the Mechanical Engineering Department of the Faculty of Sciences and Technology of the University of Coimbra

July 2016

UNIVERSIDADE DE COIMBRA

To my father, Alberto.

This is for you.

ACKNOWLEDGMENTS

This space will serve to provide a small thank you to all the people who made possible this work but also the journey until this point. So firstly:

To my adviser, Professor Amílcar Lopes Ramalho for the constant support, vast knowledge and enormous amount of time I here present my sincere thank you. To my coordinator Engineer Fernando Ramos for the approximation to the subject, the continuous follow up and rapid availability, thank you very much.

A huge thanks to Huf – Portuguesa and Huf group for supporting my work, giving me the opportunity to develop my skills in a most interesting area opening the doors of the company.

I also need to thank the Structural Integrity group in which I was working all this time, especially to Pedro Antunes for the companionship, to Professor José António Martins Ferreira, Professor José Domingos Moreira da Costa, Professor Fernando Jorge Ventura Antunes, Luis Vilhena and Joel Jesus. Thanks also to the group of people who worked with me daily in the Mechanical Department of Engineering.

To my unnamed friends, the ones that make life worth living, they hold important parts of my life.

Uppermost, to the laddies in my life for never saying no or giving me any hard time, my mother and my sister. To my nephew, the next big man. To Brandão, because he brought joy.

To THE woman in my life, Iolanda, whom I don’t see myself without. My family.

This research was co-sponsored by Portuguese Foundation to Science and Technology and Huf - Portuguesa, Grant SFRH / BDE / 52102 / 2013 which is co-funded by the program COMPETE from QREN with co-participation from the European Community and by FEDER funds through the program COMPETE – Programa Operacional Factores de Competitividade, under the project CENTRO -07-0224 -FEDER -002001 (MT4MOBI).

Governo da República Portuguesa

UNIÃO EUROPEIA
Fundo Social Europeu

ABSTRACT

The electric and electronic connectors market represents an area of business widely present on every industry, direct or indirectly. Roughly, the annual production in this sector is one trillion connectors, in which more than 200 billion belong to the automotive industry (estimated in 21%), with increasing perspectives.

Power supply and signal communication in automotive contacts, take great interest in stainless steel, nickel and gold platted. The problem with this coatings is their resistance to the wear process, in the present situation, fretting wear who dictates that the majority of contact life will be performed by bulk materials, though their properties determine the contact's longevity. These specific type of steels, AISI 304, are commonly used when a good elastic behaviour is needed like spring contacts, high elastic modulus, but also battery contacts, particularly coin batteries. As this type of contact is often used in a large number of small connectors, especially on the interface of printed circuit boards, there is a significant interest in studying the problem. Austenitic stainless steels have particular properties, mainly the low oxidation rate, that, allied with relatively low cost and availability, qualify this type of material for this specific task.

This work deals with different effects in the contact surfaces subjected to fretting movements and electric current flow on austenitic stainless steels. The main purpose is to establish a relationship between; wear, the energy dissipation by friction and the energy dissipation by the Joule effect as well as the synergetic effects.

The fretting tests consisted in reciprocating movements on a sphere-on-flat-surface contact geometry. The electric current was kept constant during the entire test at various set values, ranging from 0 mA (no current), corresponding to no energy dissipation by the Joule effect, to 120 mA. The addition of energy in the contact by the Joule effect increases the oxidation of the contacting surfaces, inducing wear acceleration in both specimens by synergetic effect. A synergetic model was introduced in order to quantify individual contributions to total wear volume, which is composed by mechanical wear, a joule effect parcel of wear and an incremental factor of degradation due to the combined effect.

As a parallel task, a wear model suitable for sliding and fretting wear was designed, allowing to estimate the volume loss on contact surfaces based on friction dissipated energy. Hertzian normal contact pressure and a friction stress field are used to determine the resulting contact stresses leading to local analysis of the wear process. An experimental validation study was performed using two pairs of materials commonly used in mechanical applications, regarding an Alumina sphere (Al_2O_3) against an AISI M2 steel flat specimen for the sliding reciprocating tests and an AISI 52100 steel sphere against an AISI M2 steel flat specimen for the fretting tests. For the wear model results present a very good correlation between experimental data and predicted values, in spite of a high dependency on experimental wear rate values used in the model. The resulting wear is compared considering both the local wear depth and the wear volume of experimental tests with the forecasted values.

Preliminary studies suggest the relevance of contact compliance as well as the debris removable and agglomeration affinities. Nevertheless, both parameters influence wear and electric resistance in an inverse way, mainly because wear particles agglomeration in the contact tend to decrease wear (protective layer) but increase largely the impedance. Consequently, analyzing surface texturing influence, evoked as dimples and hollows, on the wear and electric conduction of AISI 304 subjected to reciprocating fretting tests was of most importance. Doing so, the ability to accommodate said debris outside the contact on textured surfaces will be considered as a possibility to improve the performance of electric contacts. Tests were conducted for different sphere radius, texture densities and orientation. There is an obvious influence of contact radii on the electric performance of these type of contacts and basically almost any texture surface is better than a flat surface, counting that the surface is not easily saturated and the contact is multiple.

RESUMO

O mercado dos conectores ou componentes eletrónicos e elétricos está presente, direta ou indiretamente, em diversas áreas da indústria. A produção anual deste tipo de componentes é de aproximadamente mais de um bilhão, dos quais cerca de 21% são usados na industria automóvel, com elevadas tendências de crescimento.

Na indústria automóvel, os aços inox com revestimentos de níquel ou ouro são muito usados em contactos com passagem de corrente, alimentação ou comunicação de dados. O problema com estes revestimentos é a sua resistência ao desgaste, especialmente quanto ao desgaste por fretting, o qual dita em grande parte da vida das conexões, neste caso são os materiais de base, através das suas propriedades, que determinam a longevidade dos contactos. Este tipo de aços inox, nomeadamente o AISI 304, são comummente aplicados como molas de contacto em situações que requerem bom comportamento elástico, elevado módulo de elasticidade mas também em terminais de baterias, especificamente baterias tipo moeda. Como este contacto é muito usado em pequenos componentes, com especial atenção para os contactos de alimentação de placas de circuito impresso, existe um elevado interesse em analisar o problema. Os aços inoxidáveis austeníticos possuem diversas propriedades que os tornam interessantes, nomeadamente a sua resistência à oxidação que aliada ao baixo custo e elevada disponibilidade qualificam este material para esta tarefa específica.

O presente trabalho lida com os diferentes efeitos nas superfícies de contacto sujeitas a fretting e passagem de corrente elétrica em aços inoxidáveis austeníticos. O principal objetivo é estabelecer a relação entre o desgaste, a energia dissipada por atrito e a energia dissipada por efeito de joule e os respetivos efeitos sinergéticos.

Os ensaios de fretting consistiram em testes de movimento reciproco com contacto de esfera sobre plano. A corrente elétrica foi mantida constante durante cada ensaio, com vários valores pré estabelecidos desde 0 mA (sem corrente), que corresponde a uma adição nula de energia dissipada por efeito de joule, até 120 mA. A adição de energia dissipada por efeito de joule no contacto aumenta a oxidação, induzindo por efeito sinergético uma aceleração no desgaste em ambos os elementos do par de contacto. Foi apresentado um modelo sinergético por forma a quantificar as contribuições individuais para o desgaste total,

que será composto por desgaste mecânico, uma parcela de desgaste por efeito de joule e um fator incremental de degradação devido ao efeito combinado das duas fontes de desgaste.

Foi também desenvolvido um modelo de desgaste adequado a desgaste alternativo e fretting, que permite estimar o volume e a forma de desgaste em superfícies sujeitas a energia dissipada por atrito. A pressão normal de contacto hertziana e o campo de tensões de atrito foram usados para determinar as tensões resultantes no contacto facilitando uma análise local. A validação experimental foi elaborada com recurso a dois pares de materiais usados comummente em aplicações mecânicas, esfera Alumina (Al_2O_3) contra um aço AISI M2 em ensaios de desgaste alternativo, e uma esfera de aço AISI 52100 contra uma amostra plana de aço AISI M2 nos ensaios de fretting. Os resultados experimentais apresentam uma boa correlação com os previstos pelo modelo, apesar da elevada dependência do modelo do valor da taxa de desgaste determinada experimentalmente. Os resultados foram comparados considerando as variações de volume local e globais, nas principais secções das marcas de desgaste.

Algumas análises preliminares mostraram a importância das partículas geradas por desgaste quer pela sua acomodação sob o contacto quer quanto à capacidade de serem expulsas da zona de interface. De facto ambos os parâmetros são de extrema importância no desgaste e na resistência elétrica, embora contribuam de forma inversa, visto que a aglomeração de detritos no contacto aumenta a impedância mas tende a amenizar o desgaste (formando uma camada protetora). Pelo exposto, a análise da influência de textura pré-formadas, entenda-se por concavidades e convexidades, no desgaste e na condução elétrica de aço AISI 304 sujeito a fretting é de extrema importância. O objetivo deste tipo de estudos é determinar a aptidão de cada geometria de texturização para acomodar as partículas de desgaste fora da zona de contato. Foram conduzidos ensaios para diferentes raios da superfície esférica, densidade e orientação da textura. Existe uma tendência óbvia na influência do raio de contacto no desempenho elétrico neste tipo de contatos e basicamente qualquer textura melhora o desempenho face a uma superfície plana, contando que a superfície não seja saturada no imediato e se estabeleça contato em múltiplos pontos.

LIST OF CONTENTS

LIST OF FIGURES

LIST OF TABLES

NOMENCLATURE

μ	Friction coefficient
a	Contact radius (m)
A	Section area (m^2)
E_T	Total dissipated energy (J)
f	Fretting frequency (Hz)
F_e	Friction dissipated energy (J)
F_F	Friction force (N)
G_F	Flat surface shear modulus
G_S	Spherical surface shear modulus
h	Height of the wear scar (m)
I	Electric current (A)
J_e	Joule effect dissipated energy (J)
K_E	Wear rate (mm^3/J)
P	Normal load (N)
Q	Tangential force (N)
R	Spherical surface radius (m)
R_a	Roughness average (µm)
R_k	Core roughness depth (µm)
R_{pk}	Reduced peak height (µm)
R_q	Root mean square roughness (µm)
R_{Sk}	Skewness
R_{vk}	Reduced valley depth (µm)
R_z	Mean roughness depth (µm)
S_c	Compliance stiffness (N/m)
S_e	Elastic contact stiffness (N/m)
V	Wear volume (mm^3)
υ	Poisson's ratio
V_C	Spherical cap wear volume (mm^3)
V_F	Friction wear volume parcel (mm^3)

υ_F	Flat poisson's ratio
Vi	Voltage (V)
V_J	Joule effect wear volume parcel (mm^3)
υ_S	Sphere poisson's ratio
V_T	Total wear volume (mm^3)
δ	Imposed displacement (µm)
δ_c	Displacement of the compliance (µm)
δ_e	Elastic displacement (µm)
δ_s	Slip displacement (µm)
ΔV_E	Incremental factor of degradation due to the combined effect (mm^3)
τ	Shear stress (Pa)

1. INTRODUCTION

Electric and electronic connectors market represents an area of business widely present on every industry, direct or indirectly. The annual production in this sector is nearly one trillion connectors, in which more than 200 billion belong to the automotive industry (estimated in 21%) [van Dijk *et al.*, 2008], with increasing perspectives. The rise of this type of component in vehicles represents about 25% of the connector production growth, therefore the most influent in the sector [Bishop & Associates Inc., 2012].

In the automotive industry, navigation and instrumentation are the fastest growing vehicle electrical systems, specifically PCB (printed circuit board) components, in divergence with the decrease of the distribution margins caused by the uprising use of logistics and purchasing programs and software [Bishop & Associates Inc., 2012].

According to some automotive diagnostic tool manufacturers [CarMD Corp., 2012], taking into account the wear parts (tyres, oil, etc.), the most typical breakdown are on electrical or electronic components. Although a mechanical type breakdown is usually more expensive to repair, especially if its engine related, the disregard of a simple electric connection malfunction can lead to severe failure of a dependent essential component. In an increasingly use of embedded electronic systems, essential in vehicles with common application like hybrids or electric in which these costs are higher than usual, the connection failure can easily mean power loss and malfunction, disabling the car.

Nowadays, automobile manufacturers aim for a longer mean time between failures (MTBF) for each component, therefore increasing the car reliability and allowing a longer warranty period, beyond the two years required by law. This practice is being implemented by a large part of car manufacturers without raising the final product price, only possible when the combined reliability of all the components is increased. Regarding the previous statements, the decrease of automotive connector failure is of the most importance for manufacturers.

To clarify the notion of electric connector/connection, Figure 1 will serve as example of this kind of components. These connectors can be standalone segments, as end-to-end

terminals of electric cables and plugs, or internal connections of assembled devices, as power supply terminals.

Figure 1 – Connector illustration.

The present work deals with issues regarding the internal power supply of the RF (Radio Frequency) keys, with the main focus on internal power connections. Moreover, as it will be presented below, the main concerns fall upon the negative battery contact and PCB board contact where a significant amount of wear and damage is identified, due to surface fretting.

The current study deals with the combined effects of friction and electric current, or in other words the synergetic effects of friction dissipated energy and joule effect dissipated energy. Figure 2 shows the core subject of this dissertation, divided into 5 tasks (A, B, C, D, E), all of which were crucial to the end result of introducing a combined effect or synergetic wear model. These five tasks consisted in:

- (A) – Electric connector problem;
  - Identification of the Failure mechanisms and the parameters involved, mainly fretting, detailed in the case studies;

- (B) –Synergetic effect;
  - Hypothesis statement and involvement requirements of the combined effects of friction dissipated energy and joule effect dissipated energy;

- (C) – Material and specimens;
  -Selection of relevant materials, specimen geometries and availability;

- (D) – Test equipment and methods;
  - Fretting tribometer selection and adaptation. Specific test procedures to incorporate both singular effects;

- (E) – Synergetic model;

  -Experimental testing, first with friction isolated effect followed by the introduction of joule dissipated energy. The analysis of the combined effect produced a synergetic wear model;

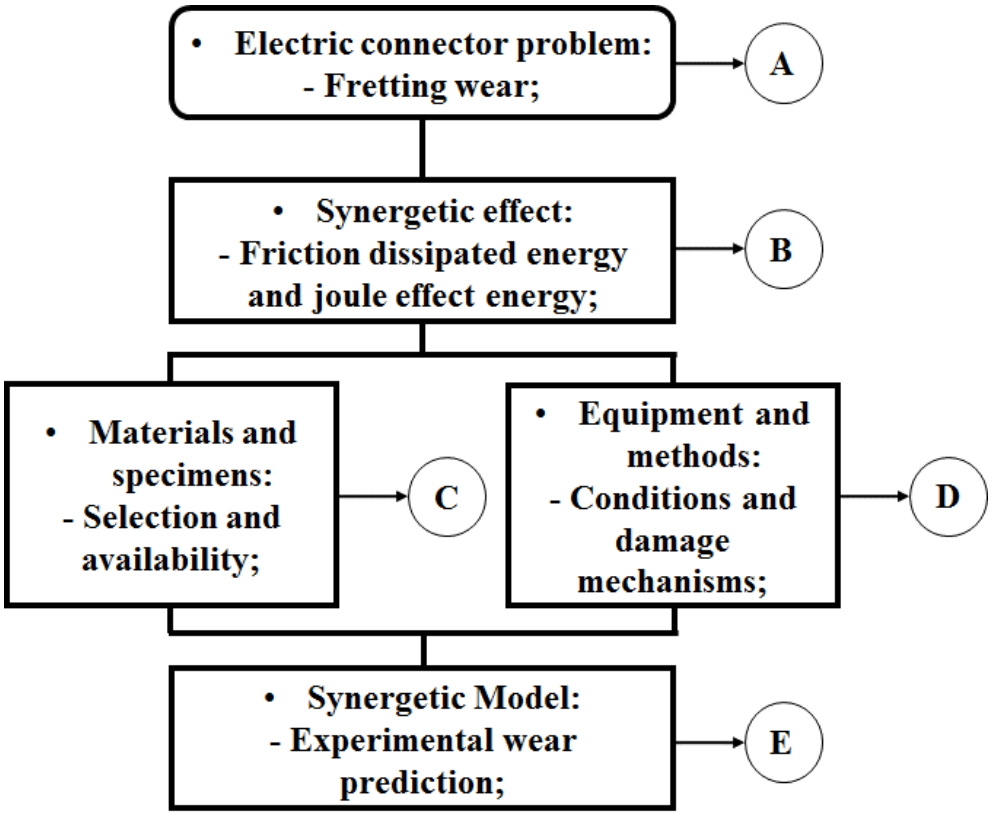

Figure 2 – Core subject interpretation.

1.1. PURPOSE

The main purpose of this research work is to establish a relationship between the energy dissipated by friction and the energy dissipated by Joule effect and to create a synergetic effects model of the behaviour of contact surfaces subjected to fretting movements and electric current flow of austenitic stainless steel against itself. Firstly, only friction governed process were studied, by means of; displacement, relative humidity,

atmosphere nature and the material properties influence. Finally, analysing the influence of both positive and negative textures (dimples and hollows) on a standard sphere-on-flat surface contact subjected to reciprocating fretting, in common spring contact stainless steels, with special attention to the debris entrapment capabilities and multi-contact connections.

A parallel assessment was introduced and a wear prediction model, for reciprocating ball-on-flat contact geometry, based on an analytical discrete method. Hertzian normal contact pressure and a friction stress field are used to determine the resulting contact stresses field enabling the quantification and matching wear amount using a model based on the energy dissipated by friction or alternatively a model based on the normal pressure (Hamilton et al., 1966; Hamilton et al., 1983). Theory of elasticity of contacting bodies is applied to determine regime transition on fretting performance (Mindlin, 1949).

1.2. MOTIVATION

1.2.1. Case studies

This section deals with the core issue motivations, answering the question:
"What industrial problem encouraged the fretting study of electric connections?"

A total of five case studies are exposed in the following pages, giving singular attention to the negative pole contact of the battery, for it is the major concern in the addressed components. As these are branded industrial components, their differentiation will be stated as case nº#.

To understand the subsequent analysis, it is important to differentiate the tree types of predominant RF key mechanisms. Fixed blade RF keys, Figure 3, basically with the assembled electronic components in one case and a fixed ignition blade. Rotating blade RF keys, Figure 4, with the same disposition as the fixed blade however the ignition blade is assembled in a rotating mechanism, which allows the blade storing. Plus, the Bladeless RF keys, Figure 5, none other than a sole electronic casing with no ignition blade.

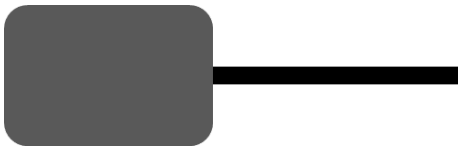

Figure 3 - Fixed blade RF key.

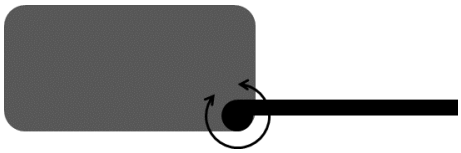

Figure 4 – Rotating blade RF key.

Figure 5 – Bladeless RF key.

The complications and produced damage are isolated in each individual case, stating the probable cause and mechanism involved. In the end of the section, the common denominators are acknowledged providing the grounds to the study.

1.2.1.1. Case study 1

The first case study is a fixed blade RF key, with two common damaging zones in the assembly represented on Figure 6, negative pole battery contacts (nickel plated stainless steel terminals) and the PCB pad contacts (gold coating over a nickel plating with copper substrate PCB pad and nickel plated stainless steel spring terminal). Both with sphere on flat contact configurations indicated typical isolated fretting wear marks on the contact pair and no significant continuous rotation on the battery.

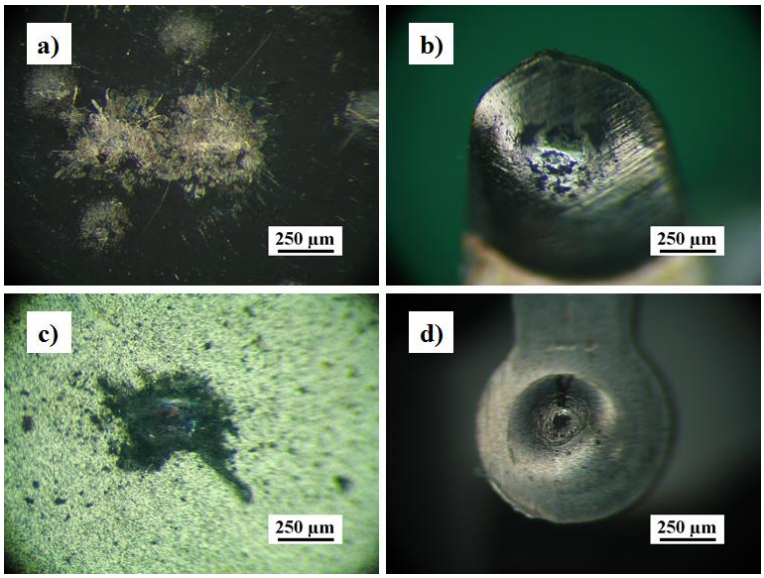

Figure 6 – Negative battery contact terminals a), b) and PCB pad contact terminals c), d) of case study 1.

1.2.1.2. Case study 2

The second case study is a rotating blade RF key, shown in Figure 7, where only a noteworthy amount of damage was identified in the battery negative contacts (nickel plated stainless steel battery and gold plated stainless steel spring terminal). Sphere on flat contact

configuration is also in use, nevertheless battery wear marks showed a major sliding wear track over fretting damage.

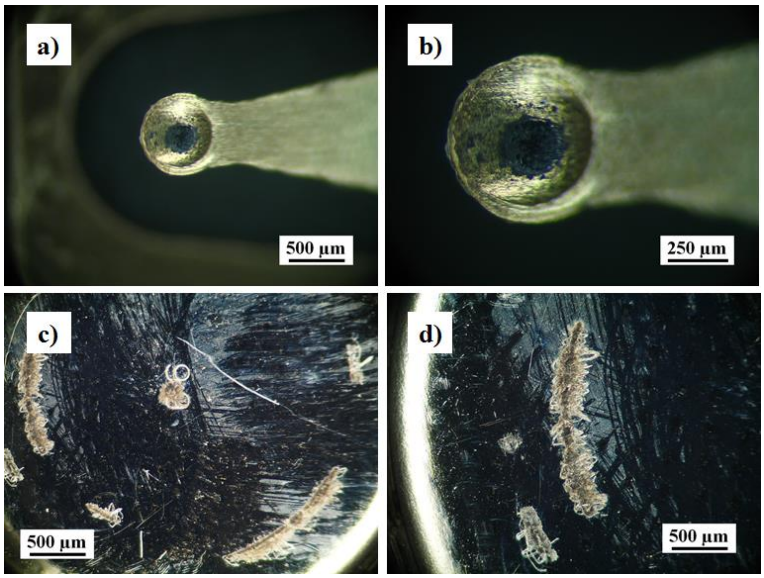

Figure 7 - Negative contact spring a), b) and battery contact c), d) of case study 2.

1.2.1.3. Case study 3

Case study number 3, matches a bladeless RF key. As the previous example, the major wear occurs at the battery negative pole contact, Figure 8. Even without a rotating blade mechanism, which should apply a rotation on the battery owed to the rapid rotation of a significant mass, the two battery examples show an obvious dual circular track as a result of a considerable rotation over fretting wear marks. The contact pair materials are similar to the negative pole on the first case study.

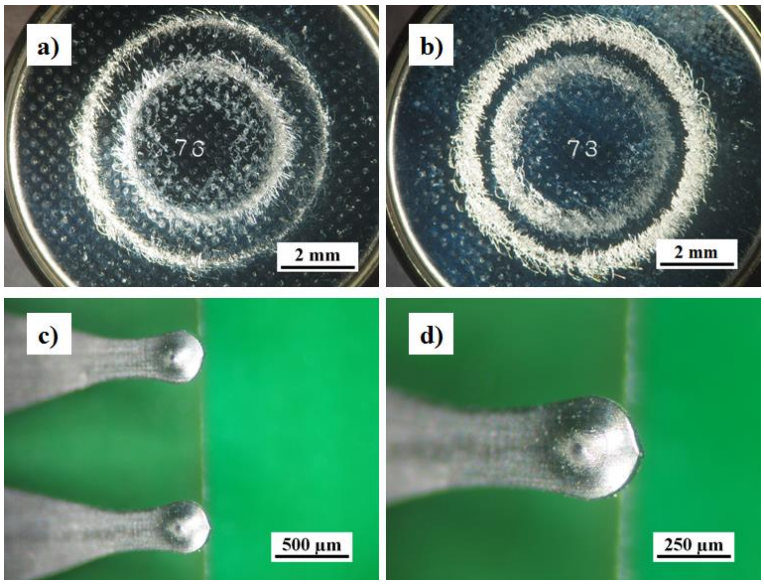

Figure 8 - Negative battery contact a), b) and negative contact terminals c), d) of case study 3.

1.2.1.4. Case study 4

The case study 4 regards to a rotating blade RF key with a singularity in the way the terminals display an inverted specification, or by other words, the negative pole terminal is directly on the PCB pad and the positive pole terminal is a cylindrical shape spring, shown in Figure 9. The battery wear was not noticeable, only PCB pad presented worn surfaces as seen in Figure 9– b) where we can identify fretting on the contact with the battery texture and perceive an non uniform contact area. An important note is the low wear, but admitting a minor time use on this component. The materials used are similar to the first study case; contact spring and PCB pad.

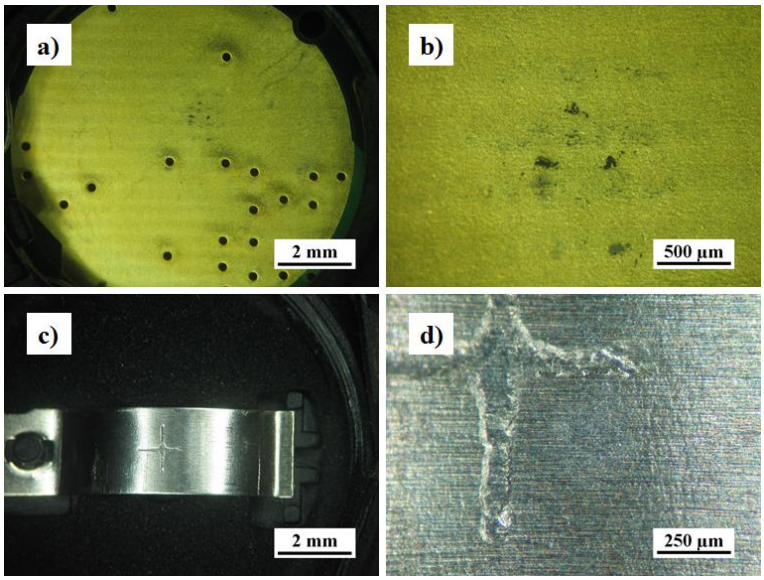

Figure 9 - Negative contact terminal a), b) and positive contact terminals c), d) of case study 4.

In commercial circulation, there are still a large number of variations not present in the case studies displayed. Nonetheless, the major issue is believed to be common to all of these products.

The main damage mechanism identified was friction wear caused by relative slip displacement between terminals, Figure 10, in the form of fretting (major cause) but also larger slip displacements, corresponding to the battery rotations.

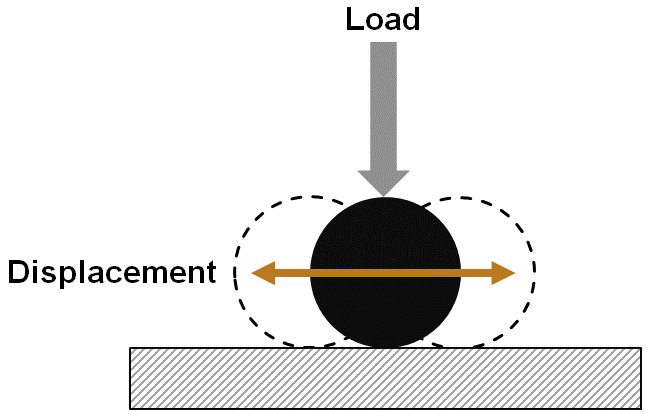

Figure 10 – Tangential slip representation of a ball-on-flat surface.

After the identification of the damage mechanisms, one doubt rose above all the rest and that was the main reason for the battery rotation. We saw through the case studies that

the initial preposition of the rotating ignition blade being the major culprit was not entirely truth as we identify battery rotation movements in bladeless assemblies. The final answer was partially the same, or at least the working principle. Seeing that the battery has a significant concentrated mass, along with all the assembled components of the keys, contrary to the high frequency small displacement vibrations which cause fretting, larger wavelength solicitations with smaller frequency should input analogous results as the rotation of the ignition key blade.

1.3. OUTLINE

A complete outline of the thesis is given in Figure 11 and bellow it the chapters are described with an indicating to which sections of the flowchart make their constitution. This is a more fitted description of the work evolution.

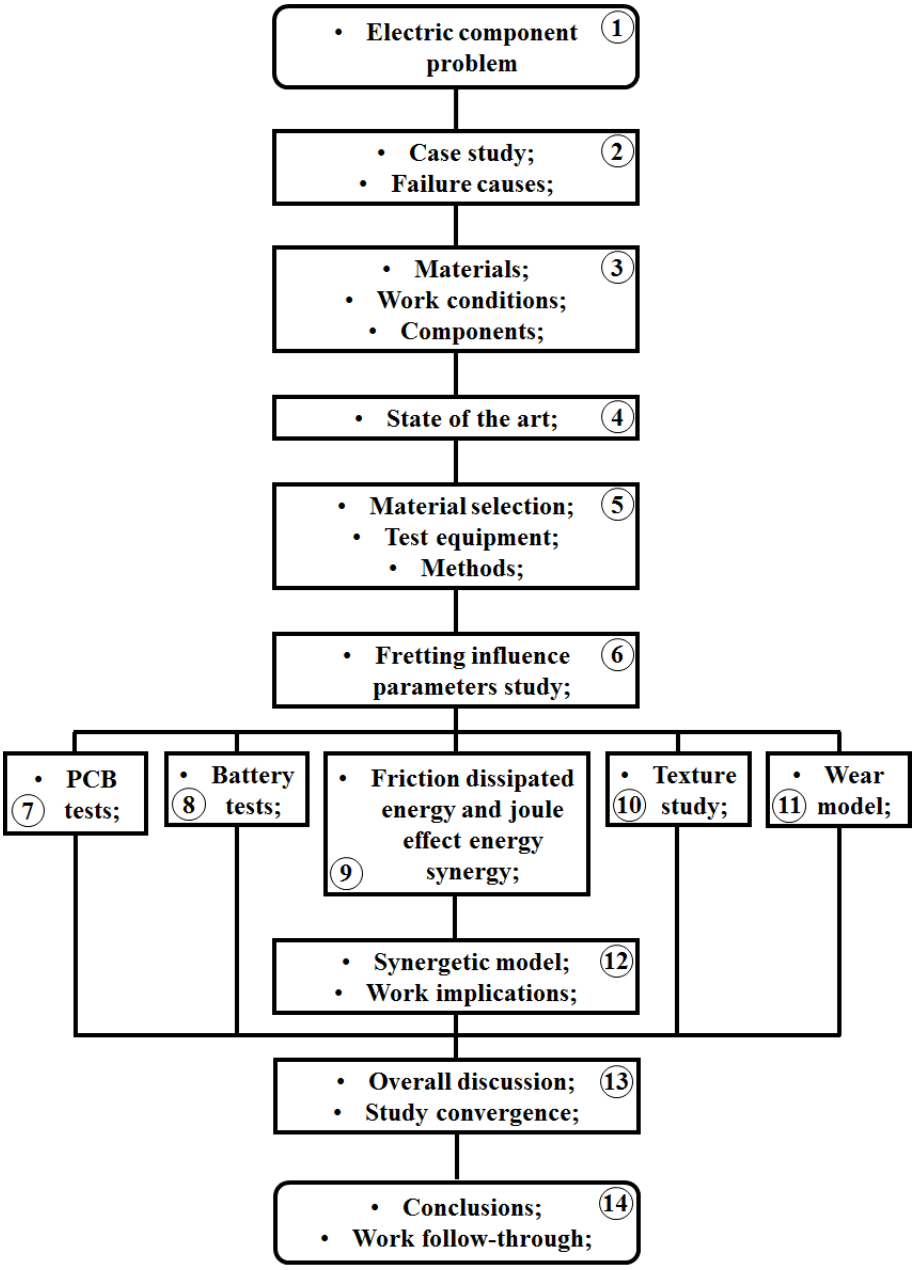

Figure 11 – Work evolution flowchart.

Chapter one corresponds to the first two sections of the flowchart, namely the problem identification and the case study failure mechanisms. The second chapter corresponds to the state of the art and the fourth section of the flow chapter. Chapter three embodies materials, equipment and methods and the equivalent sections on the flowchart are section three, the components and work conditions analysis, and section five, the materials selection, tribometers and methods. Chapter four is the most comprehensive chapter in the dissertation as it covers almost the entire experimental results, which corresponds to the

flowchart sections six to twelve, except section eleven (wear model). Chapter five is dedicated to section eleven, the wear prediction model, a tool developed alongside the core subject to aid in the project and life analysis. Chapter six states the overall discussion and conclusion statements, sections thirteen and fourteen of Figure 11, followed by the sequential references indicated to this study. At the end of the dissertation is the annex A, a section containing the stress field explicit equations applied on the wear prediction model.

1.4. LIST OF PRODUCED KNOWLEDGE

- Fretting behaviour of the AISI 304 stainless steel under different atmosphere environments. Tribology International 08/2015; 88. DOI:10.1016/j.triboint.2015.02.016. (Published).

- A Synergetic Model to Predict the Wear in Electric Contacts. Tribology Letters 09/2016; DOI: 10.1007/s11249-016-0755-y. (Published).

- Wear prediction model for reciprocating contacts. (Submitted).

- Electrical performance of textured stainless steel under fretting. (Submitted).

2. STATE OF THE ART

On the current chapter, the literature review on the addressed topics herein will be indicated and pondered. Primarily, this section is intended to portrait an evolution of general knowledge in the fields of interest but also to make the connection between the support fields. The research starts with a wide-ranging definition of the damage mechanisms, followed by major fretting influencing parameters up to the postulation and discussion of the synergetic effects of friction and electric current passing. Alongside is also the relevance of modelling tools and the interest in texturization techniques.

2.1. LITERATURE REVIEW

Due to a lack of published work regarding the electric connector performance in automotive industry, the majority of the bibliographic review is supported by published studies in the general electric connector. The area of research is nowadays of great importance but the main reason for the lack of public knowledge in the subject are intellectual properties and industrial policies.

The performance of the electric connectors, especially on the automotive industry, is directly influenced by the specific working environment, being some of the most important parameters: temperature, humidity and atmosphere nature (Zhu *et al.*, 2001; Kapsa *et al.*, 2005).

Usually, the electrical connection is achieved by two connector parts, a male and a female. Regardless of the size of the contacts, the real contact area or contact point are very small in comparison with the coupling, therefore when one or both parts of the connector are induced with movement due to mechanical or thermal solicitation the resulting deformations are dissimilar, leading to fretting wear (van Dijk *et al.*, 2008).

In wear processes, loss of material is often associated with the phenomenon causing said material removal, usually; fretting, sliding, rolling and impact. All of these can be sorted as a combination of the wear mechanisms such as; abrasive, adhesive, flow, fatigue, corrosive, melt and diffusive wear (Kato, 2002).

Friction controlled processes are present in almost every working environment and contact situations, hence there is always the need to anticipate their influence. Associated with friction is always energy dissipative mechanisms which can cause significant damage/wear on components (Bhushan, 2001).

Nowadays, when there is the need to study sliding contacts or solutions, the reciprocating test rigs are often the choice as a result of good variable control, output analysis and swift implementation (Esteves *et al.*, 2013; Antunes *et al.*, 2014; Esteves *et al.*, 2015). Essentially, in terms of slip, there is a differentiation from reciprocating sliding to reciprocating fretting, symbolised in Figure 10. Fretting consists of a reciprocating linear relative movement of two mated surfaces, where the contact is maintained on a specific zone under very small displacement, in the range of microns (Kapsa *et al.*, 2005). Reciprocating

sliding consists also on a reciprocating linear relative movement of two mated surfaces but the contact zone is not maintained, i.e. the slip distance is much higher, at least two times the contact size (Esteves *et al.*, 2013; Antunes *et al.*, 2014).

Regarding the same contact specifications, the transition from fretting to reciprocating sliding is achieved when the slip is larger than two times the contact dimension. In terms of the energy, density or distribution *per* area between the two contacts is similar for fretting and very dissimilar for reciprocating sliding cycles with at least a quotient of two (Fouvry *et al.*, 2003).

Friction parameters are usually defined by the type of application in each system working conditions, depending on; applied load, relative displacement and the movement frequency (Chaudhry *et al.*, 2013; Schouterden *et al.*, 1995, Li *et al.*, 2011). Also, the influence of the variation in each of these parameters is also dependent on the system characteristics.

The fretting phenomenon, is mainly governed by vibration sliding and one or more wear mechanisms, and is one of the main failure causes between mated surfaces subjected to vibration. It is characterized by the relative movement between two surfaces, typically in the range of microns, depending on the dimensions of the mated surfaces. The worn surface caused by this type of wear is similar to the contact interface geometry with directionality marks (Bhushan, 2001). Relative movements causing fretting are divided, usually, into four types of displacement, these being tangential fretting, radial fretting, rotational fretting and torsional fretting (Zhu *et al.*, 2011; Zhu *et al.*, 2001; Kapsa *et al.*, 2005). Tangential fretting consists of a unidirectional linear relative movement of two mated surfaces; radial fretting is typically a normal/compressing load variation induced movement that alters the real contact surface between surfaces; rotational fretting consists of rotation with an axis perpendicular to the applied load of one body over another without breaking the contact (accommodation of the contact conditions, ball bearings); and torsional fretting is characterized by a rotation of one body over another but where the rotational axis is coincident with the applied load (spinning). It should be noted that every displacement is on the order of microns (very small compared with the contact surfaces), and contact is always maintained on a specific zone and is always a reciprocating motion (Zhu *et al.*, 2011; Zhu *et al.*, 2001; Kapsa *et al.*, 2005).

Fretting regimes can be divided into partial slip, gross slip and mixed slip regimes. The partial slip regime is viewed as a small sliding area (peripheries) and a large sticking area (centre) on the contact, resulting in closed cycles of friction force versus displacement plots (fretting cycles). For the gross slip regime, sliding occurs in the majority or total contacting area and results in open cycles of friction force versus displacement plots. The mixed slip regime is a combination of the previous two regimes, as a result of the change in the contact conditions during the test (Kapsa *et al.*, 2005).

It is established that fretting, as a friction process, is governed by the combination of contact conditions (tribo-system characteristics) and not only by the material properties (Kato, 2000). These conditions include roughness, tribologically transformed films, environment conditions, friction parameters, contact conditions and mechanical properties.

The fretting failure mechanism, understood as the displacement variation in multiple bodies in contact during time (Kato, 2000; Chen *et al.*, 2002; de Wit *et al.*, 1998; Zhou *et al.*, 2006), can also be enhanced if the stresses on the bodies in contact induced by the movements vary significantly during time, surpassing the material properties (Chaudhry *et al.*, 2013; Ghosh *et al.*, 2013; Zhou *et al.*, 2006; Suh, 1978; Raman *et al.*, 2007).

A very good tool for wear estimation is the wear map, specifically in this project, during the work life maintenance or failing phases. Fretting maps can be divided into two groups: maps under fretting wear conditions and maps under fretting fatigue conditions (Zhou *et al.*, 2006), depending solely on the type of fretting failure mechanism on which it is based. There are typically three regions identified in the fretting process: the initial stage (direct contact with the surfaces or the surface films), initiation of debris formation (beginning of the wear process) and the steady state (accommodation or expelling of debris) (Hurricks, 1970).

The development of fretting behaviour is proposed by two types of model: the Archard and the energetic approach. The Archard's model is suitable for low variation of the friction coefficient and a direct relation between applied load and wear volume (Archard, 1953). The energetic approach is suitable for analysing an energetic parameter which varies along the work duration, friction-dissipated energy for instance (Li *et al.*, 2011; Kim *et al.*, 2010; Fouvry *et al.*, 2001; Fouvry *et al.*, 2003; Korsunsky *et al.*, 2010; Fouvry *et al.*, 1996).

Energy dissipated by friction generates wear damage, in spite of the wear mechanism involved, e.g. in cases of fracturing, plastic deformation or tribochemical reactions. Thus,

the energy dissipation could be directly associated with wear (Ramalho *et al.*, 2006). Energetic approaches are common applied to the field of tribology, with special attention to global influence of different wear mechanisms as seen on (Esteves *et al.*, 2015) or directly focused on the influence of tribochemical reactions on the overall wear process, as reported in (Mischler, 2008). Therefore, there is a common link between energetic input and prediction methods.

The effect of roughness has been investigated in a number of studies (Chaudhry *et al.*, 2013; Li *et al.*, 2011; Kubiak *et al.*, 2010; Fu *et al.*, 2000) and the influence of this parameter on wear and on the coefficient of friction is obvious, suggesting that the work environment should be a factor in the allowed topographic tolerances.

A mechanical property that is known to influence fretting behaviour is hardness, which should be high when it comes to maintaining a single component. This cannot be true when the contact is composed of multiple hard surfaces and the goal is to keep all components in a good working condition (Ghosh *et al.*, 2013; Farrahi *et al.*, 1992). During the fretting process, hardness may vary through work hardening or softening, an identified mechanism in fretting fatigue (Farrahi *et al.*, 1992).

The composition of the atmosphere, relative humidity, ambient pressure and temperature are the environment conditions with the greatest influence on fretting. The atmosphere composition can dictate the chemical reactions in the contact zone and therefore change the fretting response (Cai *et al.*, 2009; Hirsch *et al.*, 2013) as well as the relative humidity (Klaffke, 1995; Klaffke *et al.*, 1988), which can directly influence the coefficient of friction and transformations of the wear debris in the contact (Fu *et al.*, 2000; Chen *et al.*, 2002; Goto *et al.*, 1984; Baets *et al.*, 1998; Mohrbacher *et al.*, 1995; Cai *et al.*, 2009; Huq *et al.*, 1999). The ambient pressure (vacuum, ambient and high pressure) (Chaudhry *et al.*, 2013; Chen *et al.*, 2001; Chaudhry *et al.*, 2013) and the temperature (Hirsch *et al.*, 2013; Rybiak *et al.*, 2010; Pearson *et al.*, 2013) are parameters whose variation have a direct correlation with the oxidation of wear particles and contact films and consequently the wear volume. Some studies regarding the influence of these parameters can be found, specifically on mechanical work alloys and some composites, but with little emphasis on the austenitic stainless steels.

The oxide formation usually dictates the behaviour presented by these types of contacts, depending on the; temperature, atmospheric composition, and amount of available

water as well as the contact parameters (Hirsch *et al.*, 2013; Fu *et al.*, 2000; Mohrbacher *et al.*, 1995; Pearson *et al.*, 2013). In this contact situation the friction of the two surfaces resort on the detachment of particles through asperity contact, also increasing the temperature to the point of rapid oxidation of the particles removed. These oxides are mainly iron compounds because even with a high chromium content on the alloy the amount of iron in the composition is far greater and available for the immediately formed wear particle, a similar process as seen in (Fernandes *et al.*, 2015). The oxides that are expected to be found in a steel contact should be iron oxides (Fe2O3 and Fe3O4) (Hirsch *et al.*, 2013) and as it was found in a previous work (Esteves *et al.*, 2015), although the formation of these compounds is closely related with alloy elements and/or with surface modification techniques (Hirsch *et al.*, 2013; Fu *et al.*, 2000; Mohrbacher *et al.*, 1995).

Also, there is a distinction between oxides that are beneficial (protective films) and those that are harmful (damaging debris) (Fu *et al.*, 2000). Some oxidation models of unlubricated sliding friction suggest a slightly higher temperature on the contact than on the bulk body (Quinn, 1994), and other theories have established that a number of the contact plateaux (with a significantly higher temperature than the remaining surface) oxidize to a critical thickness that is dependent on Archard's wear rate (Quinn, 1994; Quinn, 1992; Quinn, 1998). These models enable the determination of the contact temperature and oxidation parameters through measurement of the oxide thickness and computer modelling. Moreover, the influence of bulk temperature is evident in this phenomenon, typically with a depreciative influence on the consequences because of the forming temperatures of oxidation material, in addition to the thermal dissipation effects to which the contact is subjected (Ren *et al.*, 2015; Slade, 2014).

The performance of electric/electronic connectors is strictly connected to fretting behaviour, namely the variation of electric resistance. Most published studies focus on the influence of coatings and surface treatments on electrical endurance of noble and non-noble metals with very good electrical conductivity (Jedrzejczyk *et al.*, 2009; Hannel *et al.*, 2001; Fouvry *et al.*, 2011; Laporte *et al.*, 2014; Ren *et al.*, 2014; Ren *et al.*, 2015; Woo Park *et al.*, 2009; Antler, 1985). Therefore, since the determination of electric resistance is directly related with interface contact materials, the fretting regime has an extremely important role in electric performance (Jedrzejczyk *et al.*, 2009; Hannel *et al.*, 2001; Fouvry *et al.*, 2011), whether in the preservation of coatings, maintaining a third-body-free interface, or expelling

wear debris. Also, electric resistance can be predicted by the stabilized contact slip (Hannel *et al.*, 2001) and a resulting cycle span amplitude which allows a cross-comparison between different test rigs (Jedrzejczyk *et al.*, 2009).

The influence of current flow on connector performance is usually a key parameter addressed by research on electric and electronic fretting (Ren *et al.*, 2014; Woo Park *et al.*, 2009), in part because there are limited working conditions for these types of components but also due to the direct relation between electric resistance and current load considering the same power source, adding the known synergetic effects of dissipation mechanisms in electrical conductors (Slade, 2014).

In an effort to modify friction, and consequent wear (Wang et al., 2016), surface wettability, (Yilbas et al., 2016), and surface morphology, (Fernández et al., 2016), of selected surfaces, some authors started to apply texturization techniques. These are applied to a variety of applications but, for obvious reasons, fretting is a major field of interest. There are currently three technique groups to apply surface texture, chemical etching, mechanical plastic deformation and focused radiation emission.

Chemical etching, commonly used to reveal alloy microstructures (Vander Voort et al., 2004), consists of a reacting process with partially or the entire surface structure which applies a uneven and random texture to the surface (Fernández et al., 2016). Commonly used prior to deposition process for surface activation, with a wide range of texture wavelengths, micro and macro etching.

Mechanic deformation is the most common procedure to obtain a surface texture, most of the times, as a secondary effect of the fabrication process, as seen in (Yousfi et al., 2016). It can occur directly by material removal, as a milling method, or by mechanical conformation, similar to the one used in coin battery fabrication, with a range from micro to macro textures.

The focused radiation emission consists of a concentrated energy beam, being the most common laser texturization in all its variations (Vilhena et al., 2009; Wang et al., 2016; Yilbas et al., 2016). The major benefits of this technique are the precision and variable control, (Wang et al., 2015), allowing texturization of complex or non-flat surfaces.

Most common applications are in the field of lubrication and surface adhesion. For lubrication purposes, the depressions work as a deposit of lubricant for limit or mixed regime with high localized pressure (Vilhena *et al.*, 2009; Braun *et al.*, 2014; Hua *et al.*, 2016). In

the case of surface adhesion, the attention lies on the ability to alter surface wettability or energy (Prieto-López *et al.*, 2016), allowing an alternation of friction itself on the same contact.

Regarding the influence of texturization in electric performance, there is little work done, excluding some specific application *benchmark*. Some authors, (Trinh *et al.*, 2015), studied the influence of depressions on the electric resistance of coated contacts. The oxide retention and friction coefficient reduction capabilities of these surfaces are addressed but only as a result of a specific type of texture.

There is a notorious relation between the amount of energy input to the contact and the wear behaviour and electric performance (Laporte *et al.*, 2014), but most work undertaken in this field focuses on either the friction-dissipated energy or the direct influence of current flow, disregarding the energetic input and combined contribution.

Nowadays, stainless steels are widely applied in the electric and electronic industries, mainly due to the combination of their low cost and good mechanical, oxidation, and electric properties. Few of the studies focus directly on this specific application, although the analysis is usually not multi-parametric or does not focus on the fretting phenomenon itself, which restricts the application of the results (Li *et al.*, 2011; Kato, 2000; Chaudhry *et al.*, 2013; Hirsch *et al.*, 2013; Chen *et al.*, 2001). Some authors (Chaudhry *et al.*, 2013; Nachez *et al.*, 2006) have studied the behaviour of stainless steels when surface modification treatments are applied.

The usual palliatives/solutions in fretting aim to diminish the extreme condition in every system, so that the lifetime of the coupling is maximised. Some of those techniques are surface modification (surface treatments and coatings), direct friction modifiers (liquid or solid lubricants), geometry modification and material adaptation (Schouterden *et al.*, 1995; Chaudhry *et al.*, 2013; Raman *et al.*, 2007; Kim *et al.*, 2010; Fouvry *et al.*, 1996; Fouvry *et al.*, 2006). Hannel *et al.* (Hannel *et al.*, 2001) studies the behaviour of a coated copper alloy subjected to current flow and suggest a major influence by the fretting regime. The coating endurance on the contact surface, in this case composed by noble metals, has a direct correlation with the state of the electric connection mainly because it regulates the presence and level of oxidation of the wear particles.

Every tribological characterization, regardless if the wear accumulation is classified by; time, number of cycles or energy dissipated, denotes the different regimes and transition

until a steady state is achieved (Blau, 2004). The initial stage, commonly known as running-in, can occur as a more or less severe portion, denoting higher or lower wear than the steady state, as a combination of trends with protective or depreciative results to the overall wear or even disguised as non-existing on the remaining evolution. Also, it is highly dependable on the contact conditions, materials or environment leading to different outcomes as it can amount for the majority of the life cycle (Blau P.J., 2004). On these grounds, it is extremely important to account and predict said phenomenon, as done by some authors (Hanief *et al.*, 2015), and even take the best advantage on the contact influence.

On the subject of predicting wear evolution, numerical or finite element analysis is nowadays the most applicable mainly due to the availability of resources and difficulty in resolving the contact problem. These are applied on a variety of contact situations of different components with special attention to complex stress distribution and elasto-plastic models (McColl *et al.*, 2004; Cruzado *et al.*, 2012; Mattei *et al.*, 2015; Garcin *et al.*, 2015; English *et al.*, 2015).

Some authors even combine analytical and numerical solutions (Zhang *et al.*, 2015) in order to attain a faster prediction, compared to pure numerical ones, retaining the ability to assess complex contact conditions.

Slip regime determination is crucial to evaluate and predict any sliding system performance considering, in the case of fretting, regime transition during tests or life cycle is most likely to occur (Kasarekar *et al.*, 2007; Chaudhry *et al.*, 2014).

3. MATERIALS, EQUIPMENT AND METHODS

This chapter will serve the purpose of presenting all the tools and materials used in the current study. All the materials, as well as the industrial components, were characterized in detail, to the necessary extension. The specimen preparation technics were described with special attention to particular electric current test requirements and texture manufacturing procedures. The equipment section serves the purpose of introducing the tribometer used in fretting tests and the accessory equipment, composed of observation and analysis apparatuses. Only the fretting test methods are described in detail, as it is the main focus of the work. Any secondary tests are referred to their original overview.

3.1. MATERIALS

3.1.1. Fretting – Atmosphere study and Joule effect energy synergy

To note that the material selection process was due to a similarity of steel alloys, application of designated materials and availability.

The specimens used in the study were all made from AISI 304 stainless steel 0.8 mm sheet, whose standard chemical composition and hardness (measured by micro hardness tester) are shown in Table 1. The material selection was due to the similarity with electric and electronic applications. In the interest of a clear distinction between all the materials used in the study, this will be known as AISI 304 (I).

Table 1 – AISI 304 chemical composition and hardness.

Chemical composition (%)*								Hardness
C	**Si**	**Mn**	**Ni**	**P**	**S**	**Cr**	**N**	**MPa**
0.07	1	2	8-10.5	0.045	0.015	17.5-19.5	0.11	1810

* Based on available standards.

Figure 12 displays the microstructure of the stainless steel etched with Methanolic Aqua Regia, typically the austenitic grain boundaries (dark lines) and some agglomeration of $M_{23}C_6$ carbides (dark spots), composed fundamentally of precipitates of alloying elements. The austenite's medium grain size is around 44.2±7.4 μm.

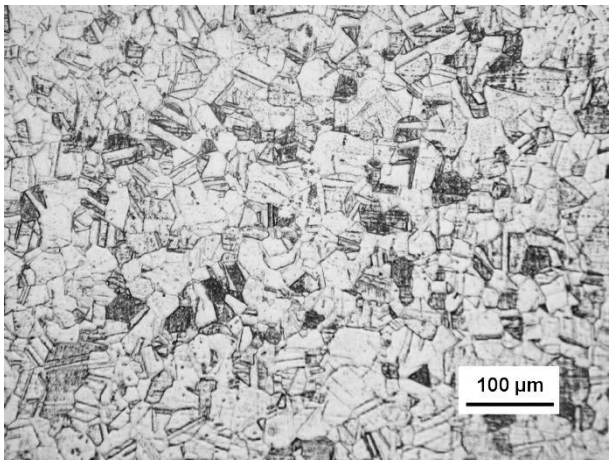

Figure 12 – AISI 304 (I) microstructure.

3.1.2. Fretting – Texture effect

The spherical specimens used in the study were all made from AISI 304 stainless steel, whose standard chemical composition and hardness are shown in Table 1, however instead of the previous 0.8 mm metal sheet a 0.5 mm one was used due to inability on the plastic conformation to the desired geometry of high radius spherical specimens. For differentiation purposes, this will be named as AISI 304 (II).

Figure 13 displays the microstructure of the textured sample, a AISI 301 stainless steel sheet with 0.1 mm. The austenitic grain boundaries (dark lines) and some agglomeration of $M_{23}C_6$ carbides (dark spots), etched with Methanolic Aqua Regia. The austenite's medium grain size is around 40.4±4.9 µm, but in these case the grains present a more elongated geometry due to lamination ratio.

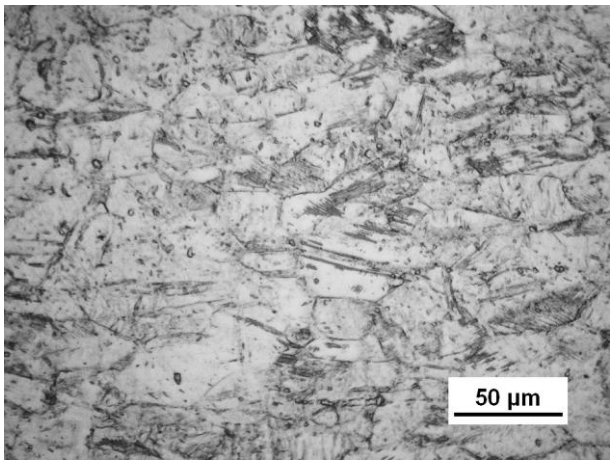

Figure 13 – AISI 301 microstructure (textured).

The standard chemical composition and hardness are presented in Table 2 and the significant difference in hardness (measured by micro hardness tester), from the standard values, is due to the cold rolling process of this 0.1 mm thickness sheet.

Table 2 – AISI 301 chemical composition and hardness.

Chemical composition (%)								Hardness
C	**Si**	**Mn**	**Ni**	**P**	**S**	**Cr**	**N**	**MPa**
0.15	1	2	6-8	0.045	0.03	16-18	0.1	4550

3.1.3. Industrial Components

3.1.3.1. Printed Circuit Board – PCB

Printed circuit boards embody a substantial part of the case study problematic. This is due especially to the spring contacts nature and contact pad fragility. As for the differences in geometry, materials, types and number of contacts present in these components, it was decided that an independent study was more fitted for a wider evaluation and subsequent application of the tools developed. Therefore, none of these components will be represented in full detail. Figure 14 is a schematic representation of a PCB board with contact Pad and springs.

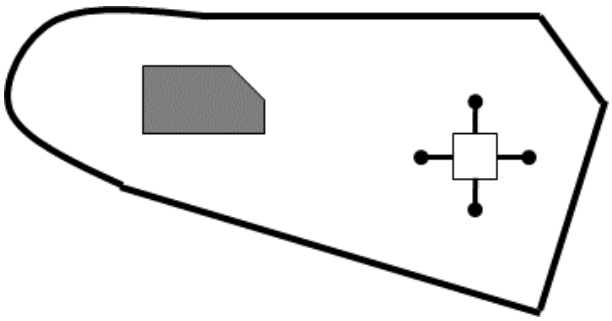

Figure 14 – PCB schematic representation.

In specific detail are represented a pad on Figure 15 of a specific PCB board used in the characterization process.

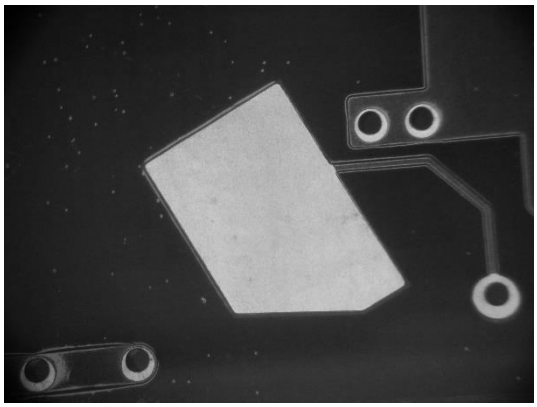

Figure 15 - PCB contact Pad detail.

By datasheet specification analysis, the studied PCB pad is a composed surface of three layers. The basis or substrate is a copper pad, internally connected on the PCB by copper lines, covered by a nickel platting commonly used in electric connections, Figure 16 a), and a gold coating to ensure a low contact impedance, also visible in Figure 16 b) inside the yellow border.

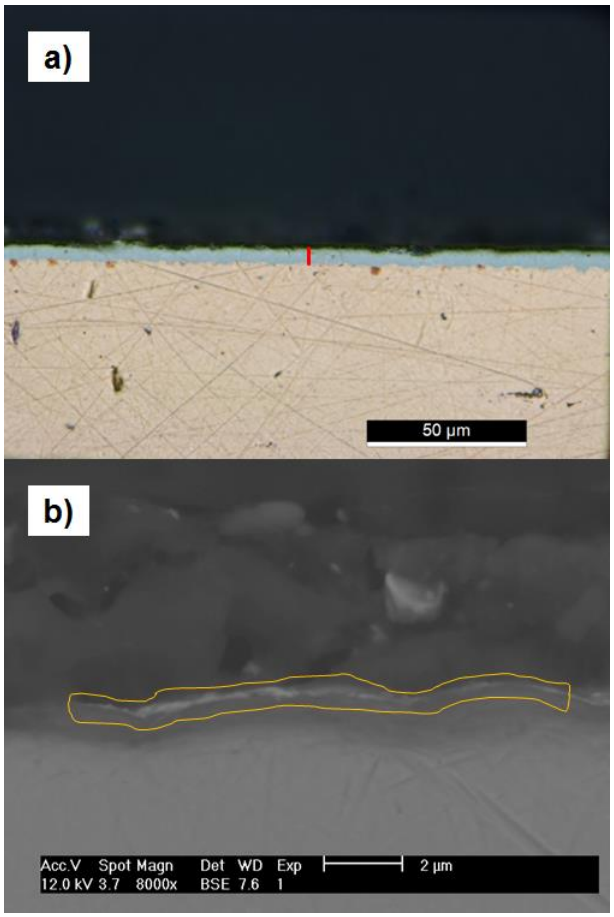

Figure 16 – PCB nickel platting and gold coating cross sections: a) – optical cross section PCB image; b) – cross section PCB (SEM).

By measuring the cross sections of the nickel and gold coatings it was possible to estimate their thickness, shown in Table 3. It is easy to conclude that a minor solicitation on the gold coating will remove said material almost immediately.

Table 3 – PCB coating thickness.

PCB	Coating Thickness (µm)
Gold Coating	0.1-0.2
Nickel Platting	7-8

To establish the electric connection on the pad a stainless steel terminal is used, Figure 17, which corresponds to the positive terminal of the battery. The conditions resulting from contact are provided below.

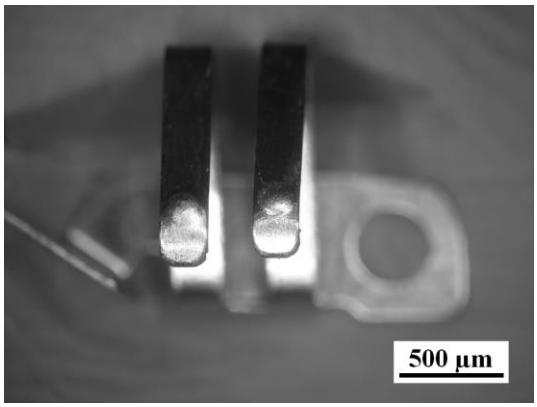

Figure 17 – Stainless steel pad terminal.

Laboratory tests were performed under the same contact conditions, specifically the hertz maximum normal pressure. Therefore, the terminal tip radius and spring stiffness response were measured, shown in Table 4 and Figure 18 respectively.

Table 4 – PCB pad terminal spring.

Number of contact springs	2
Tip diameter (mm)	2.6

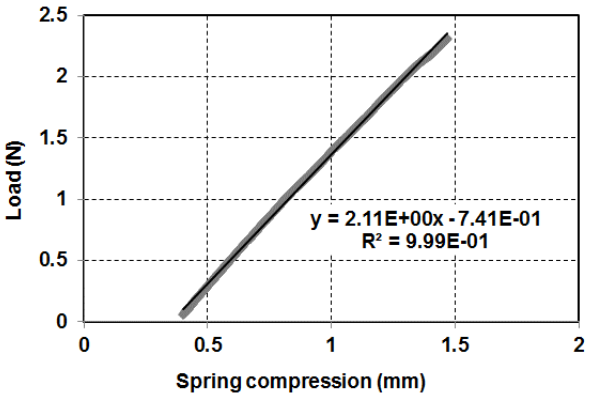

Figure 18 – PCB pad terminal spring compression response.

After taking into consideration these previous results, the estimation of the normal load and hertz maximum stress for the PCB pad were possible, Table 5. The considered load interval was determined based on in situ spring compression distance.

Table 5 – PCB pad contact strains and stresses.

Estimated load range (N)	0.7-1.20
Estimated hertz maximum normal stress (GPa)	1.23-1.49

The spring contact, which matches the negative pole of the battery in Figure 19, is a common electric contact spring, an AISI 301, nickel platted with a contact diameter of approximately 1.2 mm. The positive pole contact with the battery is also composed by an AISI 301 stainless steel with nickel platting coating.

Figure 19 – PCB Spring contacts detail.

For the contact springs, on both positive and negative terminals, there were no coating thickness evaluation due to geometrical restrictions. Only the contact parameters were determined, similarly to the PCB contact terminals. The tip mean diameter is shown in Table 6, and is obviously smaller than the one from the pad.

Table 6 – Negative pole terminal spring.

Number of contact springs	4
Tip diameter (mm)	0.52

Taking into consideration the spring stiffness response, shown in Figure 20, a normal load as well as the hertz maximum pressure were estimated, Table 7, also taking into account an *in situ* spring compression distance of the assembled components.

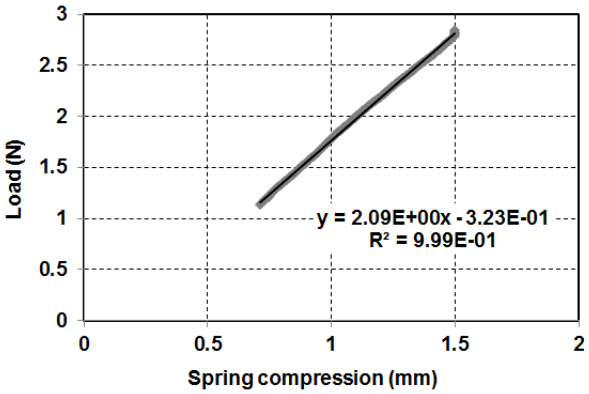

Figure 20 – Negative pole terminal spring compression response.

Table 7 – Negative pole terminal contact strains and stresses.

Estimated load range (N)	0.25 – 0.5
Estimated hertz maximum normal stress (GPa)	2.11 – 2.66

3.1.3.2. Batteries

The battery specimens commonly used in this case study are introduced bellow, deprived of their commercial designation. The majority of our work focused on the operating conditions and contact parameters of the negative pole.

Both specimens are listed below, Figure 21 and Figure 22, with similar geometric shapes differing mainly on dimensions.

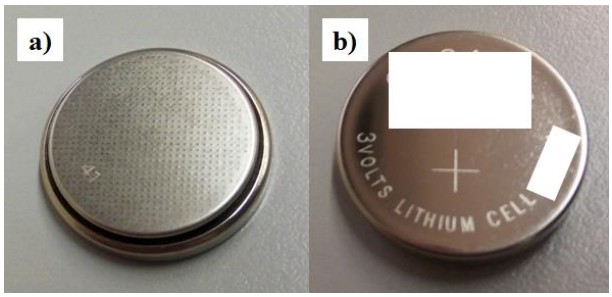

Figure 21 – Battery specimen 1, a) negative pole contact; b) positive pole contact.

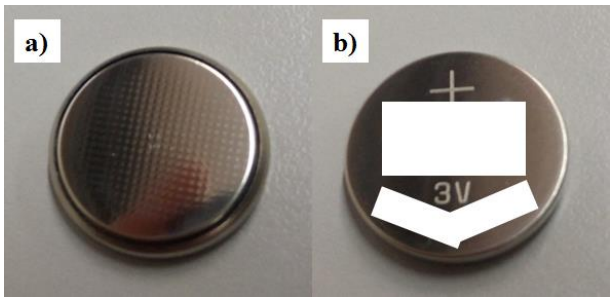

Figure 22 – Battery specimen 2, a) negative pole contact; b) positive pole contact.

Overall, in this scope the relevance and where we will focus stands on the materials and surface parameters, considering that by standard both of them have by an AISI 430 nickel plated alloy for the casing and display very singular surface topography.

3.1.3.2.1. *Surface Characterization*

Surface characterization covered four aspects; roughness, texture, hardness and coating thickness. Roughness measurements, shown in Table 8, are clear when it comes to the comparison between specimens. Both have very analogous mean, root mean square and peak roughness parameters, with singular skewness behaviour, very close on specimen 1 and opposite in specimen 2. The roughness parameters were selected as a way to characterize not only the height of the roughness profile but also to a better understanding of the surface morphology as distribution of peaks and valleys.

Table 8 – Surface roughness parameters for the battery specimens.

Battery		Ra (µm)	Rq (µm)	Rz (µm)	Sk
Specimen 1	**(-) pole**	0.583±0.119	0.735±0.144	2.971±0.681	0.600±0.324
	(+) pole	0.056±0.001	0.071±0.002	0.462±0.029	0.516±0.132
Specimen 2	**(-) pole**	0.591±0.097	0.687±0.093	2.202±0.130	0.544±0.087
	(+) pole	0.078±0.009	0.100±0.011	0.582±0.042	-0.866±0.432

The negative pole contact texturization, detailed in 3D profilometry (Figure 23), is a clear attempt to alter the contact dynamics. On the same line of thought, texture parameters

were identified and displayed in Table 9. Note that, due to the nickel platting process on the batteries, the tip of the dimples are flattened (increase of tip radius).

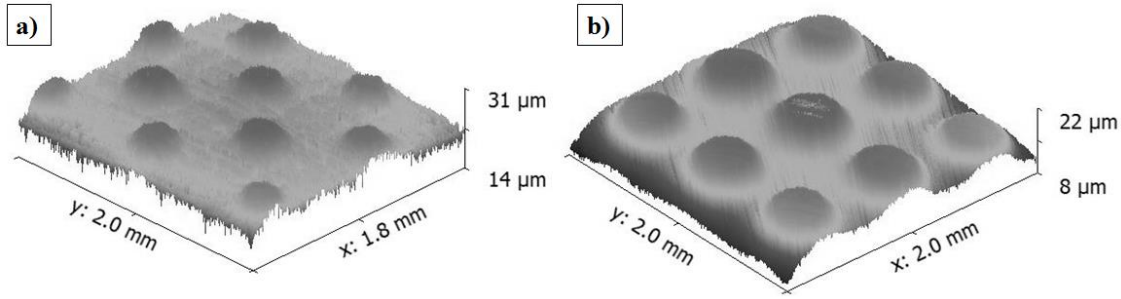

Figure 23 – Textured negative pole contact surface of battery specimen 1 (a) and specimen 2 (b) (3D profilometry).

The texture is not very differentiable between specimens, at least in the scope of the contact in which it is applied, seen in the case study presentation. An important conclusion amidst these combined analysis is the fact that the contact dimension is not sufficient to activate or take advantage of the texture.

Table 9 – Texture parameters for battery specimens, negative pole.

Battery	Dimple Tip Diameter (mm)	Mean Height (µm)	Density (unit/mm^2)
Specimen 1	12.5	5	9.47
Specimen 2	37	5	8.16

Coating thickness was determined by ball cratering, fully described in (Antunes *et al.*, 2003), and the results are shown in Table 10. Specimen 1 presented a denser coating, nevertheless both are very similar and very near 10 µm.

Table 10 – Battery specimens nickel plating thickness.

Battery	Coating Thickness (µm)
Specimen 1	13
Specimen 2	8

Besides the electric performance improvement, the nickel plating should also improve the wear resistance of the batteries by means of a higher hardness. Both sides, as well as the isolated substrate material, were tested and the results are displayed in Table 11.

Table 11 – Hardness for the battery specimens.

Battery (MPa)	(-) pole	(+) pole	Base material
Specimen 1	2,420	2,890	2,300
Specimen 2	2,580	2,490	2,060

After analysis, the hardness results indicated a similitude of both contacts and specimens, not very apart from the substrate results even considering that the plating hardness is a composed value from both steel and nickel, characteristic of thin coatings.

3.1.4. Specimen Preparation

A different set of methods were applied for specimen production to match the requirements of the selected studies. As some of the tests share the same type of specimens, the methods will be announced as the studies in which they are inserted.

3.1.4.1. Atmosphere study and Joule effect synergy

The stationary specimen presents a flat geometry (parallelepiped) and the moving sample a spherical surface with a radius of 4 mm shown in Figure 24, obtained by mechanical conformation from a 0.8 mm thick sheet, AISI 304 (I).

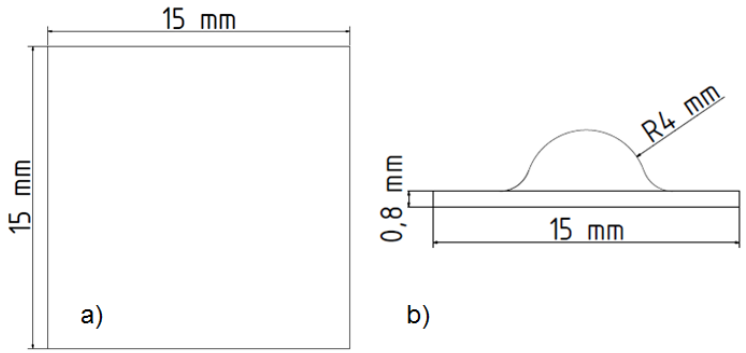

Figure 24 - a) Flat specimen; b) Spherical specimen.

Every test specimen was polished in a routine beginning with sandpapering and completed with the use of a 3 µm diamond finishing suspension in order to ensure a uniform and even contact surface through all the samples. The characteristic roughness parameters are shown in Table 12.

Table 12 – Roughness parameters.

	R_a (µm)	R_q (µm)	Sk	R_z (µm)	R_k (µm)	R_{pk} (µm)	R_{vk} (µm)
Mean	0.049	0.058	-0.050	0.296	0.147	0.033	0.036
STD	0.001	0.001	0.021	0.011	0.006	0.003	0.001

The roughness parameters were selected as a way to characterize not only the height of the roughness profile but also to better understand the surface morphology as distribution of peaks and valleys, with special attention to the Abbot Firestone curve. Ultimately, these group of parameters allowed us to establish a reliable polishing procedure for the entire set of specimens.

There was an additional requirement of electric current flow on the joule effect synergy study however it didn't force any adaptation of the specimens since the connection was maintained directly through the tribometer specimen support.

3.1.4.2. Texture effect

For the texture effect study, two kinds of steel were used being all spherical samples made from AISI 304 (II) and every texturized one from AISI 301, both specified on the materials sections.

Starting with spherical specimens, there were three diameters prepared to evaluate texture effects; 11.2 mm, 17.3 mm and 26.7 mm. These high values were selected deliberately to activate all texture effects applied, also obtained by mechanical conformation from a 0.5 mm thick sheet, AISI 304 (II) with a square base shape of 30 mm by 30 mm.

The texturization process was introduced in the study as a way to benchmark battery surface textures and how to better take benefit of their effects. As a first approach, a comparable texture was created to serve as a starting point resorting to indentation techniques.

This being an evaluation of a process applied in batteries is only natural that the texturization process follow the same principle, negative mechanical conformation of a thin steel sheet. Since we couldn't execute the entire texture in one operation, instead we used a sequential process of a single puncture. The indenter used in the process, shown in Table 13, was selected to implement a wide range of textures.

Table 13 – Texturization indenters.

Indenter Type	Conical
Diameter (mm)	0.078
Tip angle	74°

The process uses a CNC machining equipment, as a sequential operator of the indenter with load control. The sheet samples, 50 mm by 10 mm, were tightened on the extremities over a deformable basis to allow plastic deformation of the sheet specimen.

To take full advantage of the texture it is important to maintain a multipoint contact (more than one dimple) and a void volume to accumulate debris. Especially for the last condition and the ease in creating negative textures, hollows to accumulate debris, a negative

texture with the same densities were also prepared and tested. Table 14 establish the texturization parameters of the test specimens, apart from the flat standard samples.

Table 14 – Texture characteristics.

Texture	Density (unit/mm^2)	Mean Height (µm)	Diameter (mm)
Dimples (positive)	6.25	5.7	1.30 (tip)
	11.11		
Hollows (negative)	6.25	5.5	0.13 (hole)
	11.11		

Figure 25 and Figure 26 are 3D laser profilometry representations of the specimen texturization, positive and negative with different density. Here, we can get a sense of the available void space between single texture elements.

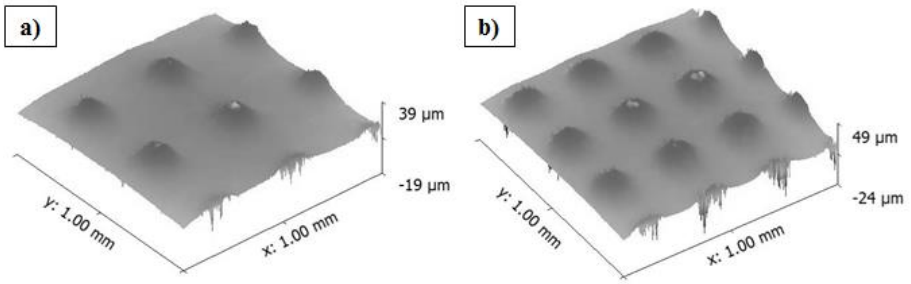

Figure 25 – Positive texture with 6.25 unit/mm^2 (a) and Positive texture with 11.11 unit/mm^2 (b) (3D profilometry).

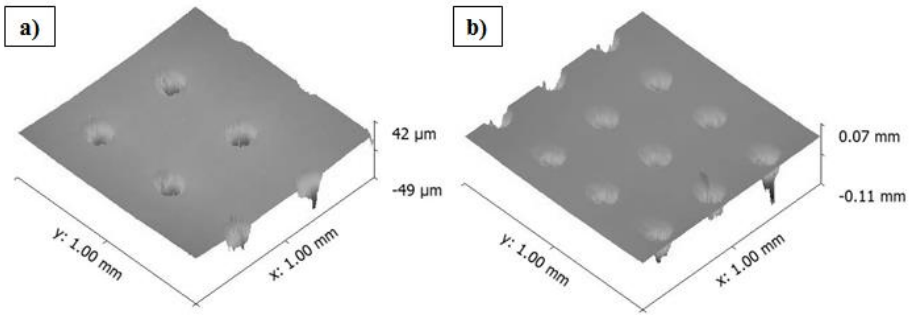

Figure 26 – Negative texture with 6.25 unit/mm^2 (a) and negative texture with 11.11 unit/mm^2 (b) (3D profilometry).

None of the textured specimens were polished since the texture effects would overlap roughness, consequently surface morphology is as laminated.

To assure a stable electric connection between specimens and the resistance measurement circuit, impossible to form through the tribometer specimen support, a soldering process was established. The objective was to use tin solder to easy and reliably make connections, however to do so we needed to coat a border of stainless steel spherical and textured specimens with copper, Figure 27, with a bath shown in Table 15. Prior to the copper deposition the surface was activated with hydrochloric acid.

Table 15 - Copper plating bath parameters.

Surface activation (time)	hydrochloric acid (10s)
Solution (concentration)	Copper sulphate and H_2O (100 g/dm^3)
Tension	3.3 V
Current density	14 – 42 A/dm^2
Cathode	copper
Temperature	25 ºC
Deposition time	30 s

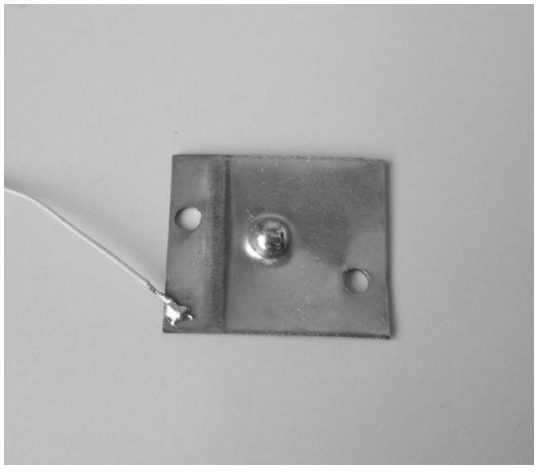

Figure 27 – Tin soldered over copper coating in spherical specimens.

3.2. EQUIPMENT

On the current subchapter, only the tribometers related to this fundamental subject will be described in detail and every supplementary characterization device would be referred to an original description. All measuring and analysis equipment will be mentioned in the final section of this subchapter.

3.2.1. Fretting tribometer

The tribometer used (Figure 28), which was developed in the University of Coimbra, imposes a unidirectional reciprocating movement (tangential fretting) induced by a piezoelectric actuator PI P-845.40 actuated by the driver E-665. XR.

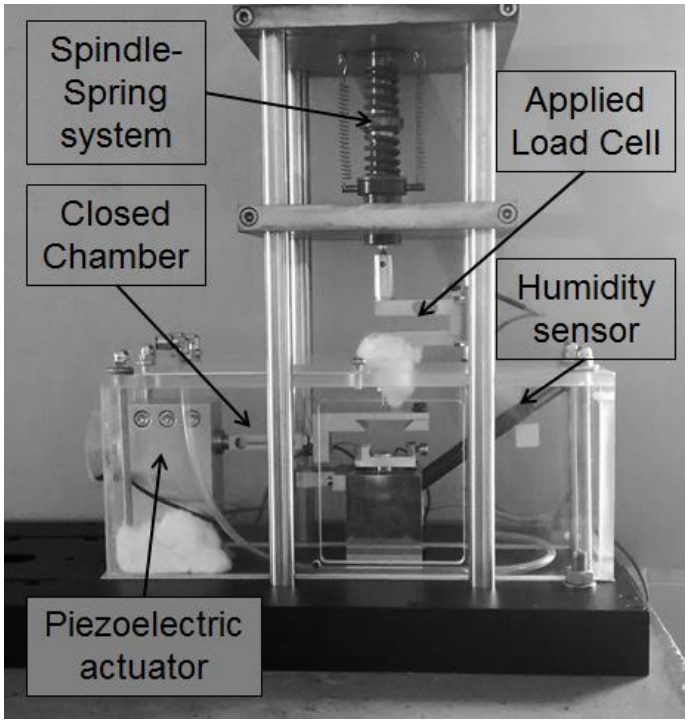

Figure 28 – Fretting tribometer.

The normal force is applied directly on the upper specimen holder by a spindle-spring system and is measured by a load cell (Figure 29). The piezoelectric actuator has a built-in displacement meter but due to the system deformation it is necessary to measure the relative displacement as near to the contact as possible, so it is quantified by a resistive sensor on the lower specimen (fixed flat specimen). The lower specimen holder is supported by a piezoelectric tangential load cell *Kistler* 9143B21, forming a bridge between the sample holder and the reference base of the equipment, allowing assessment of the friction force.

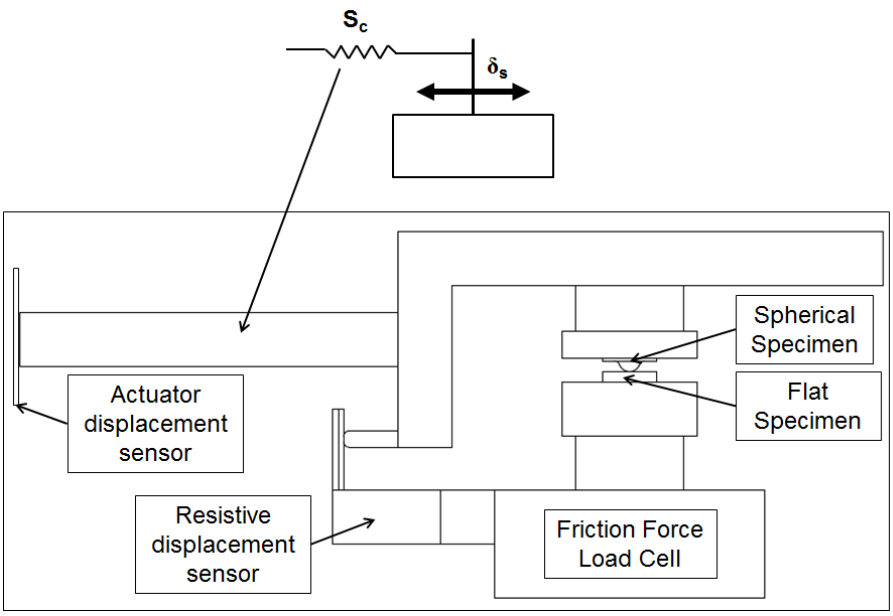

Figure 29 – Contact zone schematics and equivalent rigidity diagram.

Also, part of the test apparatus is the atmospheric conditions control system, which allows the variation and control of relative humidity in a closed chamber by means of an assembly comprising a pump and humidifier/desiccator circuits and humidity/temperature sensor in the test chamber, along with the introduction of an oxidizing (100% oxygen) or reducing (100% nitrogen) atmosphere, which was supplied by gas cylinders. This variation aims to assess the complete lack of relative humidity and maximise the oxidizing atmosphere to evaluate its influence.

The use of a displacement sensor near the contact is in order to reduce the effect of the deformation (elastic effect) of the actuator transmission, which is not perfectly rigid to allow the load application (Figure 29). Although the values measured by the resistive displacement sensor are influenced by the system deformation effect, the compliance of the

system (Ramalho *et al.*, 2003; Fouvry *et al.*, 1995) and its influence can alter the true values of displacement, leading to incorrect interpretations.

Also, part of the test apparatus is the electric current supply circuit and measurement, Figure 30, allowing the supply of a constant electric current and monitoring of the electric resistance and a Wheatstone bridge circuit, Figure 31, to measure electric resistance up until catastrophic values (limit conditions). In that figure, *Rc* is the contact resistance which we want to monitor, while the resistance R_0 was selected to control the current over the contact. The entire process is controlled and monitored by computer, specifically with a *LabView* interface.

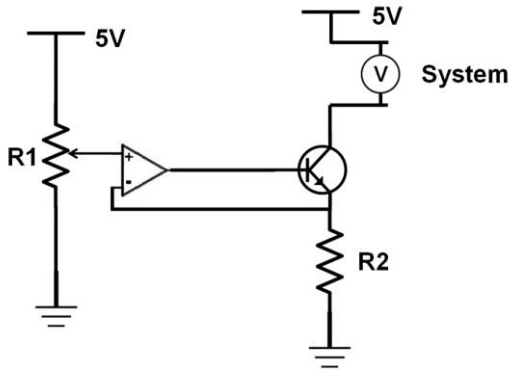

Figure 30 - Electric current supple circuit.

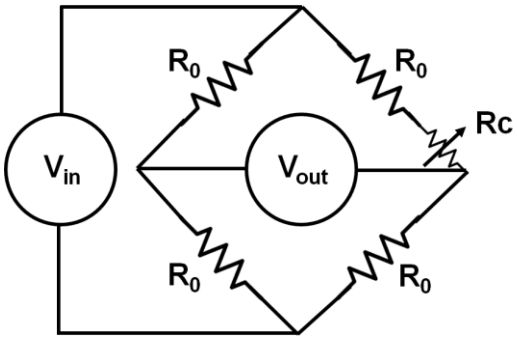

Figure 31 – Wheatstone bridge circuit.

The imposed displacement is characterized by three components, as presented in equation (1) and Figure 32.

The system compliance, is due to deformation of the system and can be used to correct the values of displacement.

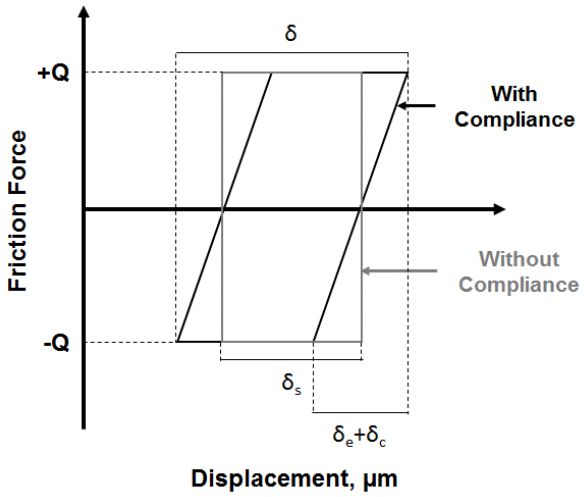

Figure 32 – Theoretical representation of compliance influence, dark with compliance and grey without compliance.

In Figure 32, the slope of the dark fretting cycle, which is equal to the stiffness, is due to deformation of the system and can be used to correct the values of displacement.

$$\delta = \delta_e + \delta_c + \delta_s \tag{1}$$

where δ_e is the elastic component of the displacement considering a Hertzian contact, δ_c represents the displacement of the compliance and δ_s is the slip displacement. The elastic and compliance components are calculated by equations (2) and (3) (Ramalho *et al.*, 2003; Fouvry *et al.*, 1995).

$$\delta_e = Q \times S_e = \frac{F_t}{8a_1} \times \left(\frac{2-\upsilon_s}{G_s} + \frac{2-\upsilon_F}{G_F}\right) \tag{2}$$

$$\delta_c = Q \times S_c \tag{3}$$

Given the previously presented assumption which states that the system compliance can be corrected by the fretting cycle slope, the system stiffness comprised between the displacement measuring points can only be assumed because the elastic stiffness of the contact is much higher (Johnson, 1985). Consequently, the resulting displacement can be calculated by equation (4).

$$\delta_s = \delta - \delta_c \quad (4)$$

And so, to eliminate confusion in the representation of displacement amplitude results, said results will be designated by their imposed displacement values.

3.2.2. Accessory equipment

This section serves the purpose of listing all measurement and analysis equipment with corresponding applications, summarized on Table 16, being that these are commercial devices.

Table 16 - Measurement and analysis equipment.

Function	Name
Optical microscopy	*Leica DM4000 M LED*
SEM	*Philips® XL30 TMP*
EDS	*EDAX – Genesis XM2*
3D laser profilometry	*Mahr-Rodenstock RM600-3D* *Gwyddion post processing software*
Contact profilometry	*Mitutoyo Surftest- SJ-500/P Series 178*
Hardness tester	*Struers Duramin*

3.3. METHODS

3.3.1. Atmosphere study

The tests are only initiated when every sample has been cleaned in an ultrasonic bath, prior to assembly on the tribometer. Both flat and spherical specimens are assembled and the contact is established, the desired normal load is applied, then the chamber is closed. The desired atmosphere restrictions are established and these homogenise while the test parameters are defined according to the specific trial requirements (displacement, frequency and number of cycles).

The experimental conditions of the tests without electric current are: for displacement variation (20 µm; 40 µm; 50 µm; 60 µm) maintaining 50% of relative humidity; for humidity variation (10%; 50%; 85%) maintaining 40 µm of displacement. The reference condition is the 40 µm displacement and 50% relative humidity in normal atmosphere. The different atmospheres introduced into the testing chamber were a reducing atmosphere (nitrogen), an oxidizing atmosphere (oxygen) and a normal composition atmosphere (room atmosphere) maintaining the displacement at 40 µm.

The remaining parameters were the same for each test, with an oscillating frequency of 10 Hz, the number of cycles set as 10,000 and a constant contact pressure of 2 GPa according to the Hertzian contact stress theory.

Subsequently, the specimens are observed in the scanning electron microscope (SEM) and in the elemental analysis for oxidation examination (EDS). Before measuring the wear on each specimen, both are cleaned in an ultrasonic bath to remove the majority of adherent wear debris. Finally, the flat specimens are scanned by 3D laser profilometry and the data are measured in *Gwyddion*®. The spherical specimens are photographed with an optical microscope, then the volume of the spherical cap (volume removed from the specimen) is calculated according to expressions (5, 6):

$$h = R - \sqrt{R^2 - a^2} \tag{5}$$

$$V_c = \frac{1}{3} \times \pi \times h^2 \times (3R \times h) \quad (6)$$

The energy dissipated is equal to the work produced by the friction force, so, in order to determine their amount, it is necessary to integrate the fretting cycles along the test, as in equation (7):

$$\sum F_e = \oint_{\delta} F_F \, dx \quad (7)$$

3.3.2. Joule effect synergy

Every step of the test procedure is the same as the previous section, atmosphere variation study, except for the introduction of electric current applied by a specific circuit, previously shown on the equipment section.

Electric current values of 0, 10, 35, 60, 90, to 120 mA were considered, selected based on the application and desired result of joule dissipated energy contribution. The remaining parameters are the same for each test, with an oscillating frequency of 10 Hz, 2 GPa of maximum Hertzian pressure, an imposed displacement of 40 µm, a triangular wave type, 50% relative humidity, and test duration set as 10,000 cycles, selected based on previous experiments, desired application and equipment characteristics.

As the electric supply is monitored, fixed current and oscillating tension and resistance, the post processing take into account the energy dissipated by joule effect.

The energy dissipated by the Joule effect in each cycle is determined by the power divided by the number of cycles *per* second and is equal to (8):

$$J_e = \frac{Vi \times I}{f} \quad (8)$$

3.3.3. Texture effect

Regarding the texture effect study, as occurred with the joule effect work, fretting tests were conducted using the atmosphere study procedure, apart from the tin soldering of the specimen terminals to the Wheatstone bridge circuit. Test parameters were fixed at 40 µm imposed displacement, 7 N of normal load, 10 Hz for working frequency, 10,000 cycles test duration, with a triangular wave, and relative humidity was maintained at 50 %.

Texture effects were separated in 3 different groups, Table 17, and from the first group the performances were benchmark in order to isolate conditions of interest.

Table 17 – Texture effect condition groups.

Group	**Texture (unit/mm^2) / Sphere (mm)**			
1	Flat / 11.2 mm	Flat / 17.3 mm	Flat / 26.7 mm	–
2	Flat / 11.2 mm	Dimples (6.25) / 17.3 mm	Dimples (6.25) / 26.7 mm	Dimples (6.25) / 11.2 mm
3	Dimples (6.25) / 11.2 mm	Dimples (11.11) / 11.2 mm	Hollows (6.25) / 11.2 mm	Hollows (11.11) / 11.2 mm

The impedance circuit works with a fixed voltage and the resistance is monitored by the fretting test Labview interface.

4. EXPERIMENTAL RESULTS

The results will be presented in two different sections. The first will analyse the main parameters which influence fretting without electric current: amplitude of relative displacement; the relative humidity in the atmosphere; reactivity of the atmosphere. The effect of normal load was not considered in the scope of the present study to reduce the number of test variables.

Secondly, the tests with electric current will be discussed, starting with the synergy effect study followed by the texture effect investigation. The main purpose of the synergy effect study was to establish a relationship between wear and the energy dissipation by friction and the energy dissipation by the Joule effect as well as the synergetic effects. Moreover, surface texturization was implemented with the sole purpose of improving the electric connection performance, a low impedance and higher connection life.

4.1. STUDY OF FRETTING WITHOUT ELECTRIC CURRENT

Every specimen used in this section was produced from AISI 304 stainless steel (I) according with the preparation procedure previously presented.

4.1.1. Displacement amplitude

As discussed before, in the present study every displacement amplitude depicted in the results section refers always to the imposed motion of the piezoelectric actuator. This sub section corresponds to displacement variation (20 µm; 40 µm; 50 µm; 60 µm) maintaining 50% of relative humidity.

The wear volume clearly increases for higher displacements (Figure 33), essentially because of the bigger sliding distance, which results in gross slip regimes and wider fretting cycles.

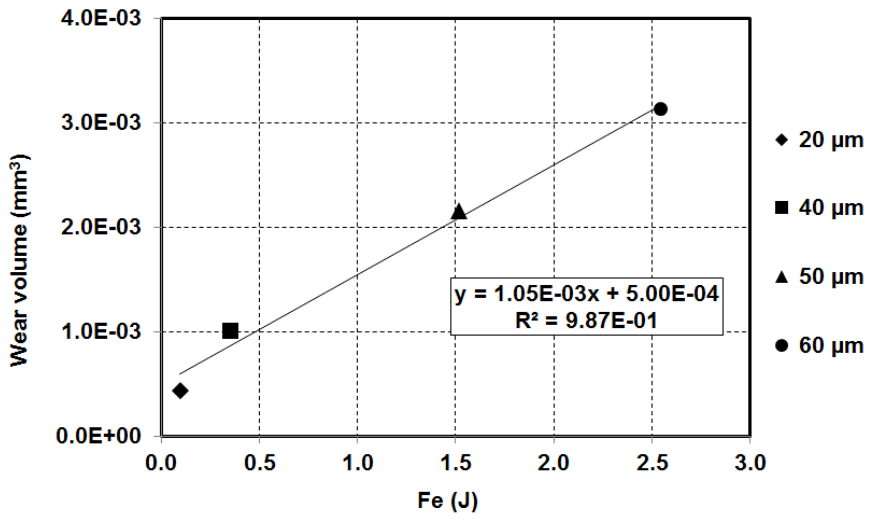

Figure 33 – Wear volume versus energy dissipated by friction for displacement variation.

The coefficients of friction presented in Table 18 from stabilized fretting cycles clearly indicate the variation of the friction condition with material removal and surface alteration, these processes are highly correlated. These results demonstrate that for the two lower displacement values the slip should not occur in the entire contact area, which induced low friction values. In fact, as shown in Figure 34 – b), the shape of the fretting loops changes with the increase of the displacement amplitude. Up to 40 µm, the loops display an elliptical shape which corresponds to a partial slip fretting regime, corroborating the low friction values. When the stroke is higher than 50 µm, the slip extends to the entire contact area, inducing an increase of the friction with a corresponding change of the loop shape to a rectangular appearance.

Referring to the fretting cycles presented, the value of compliance stiffness S_c is approximately 0.49 N/µm and every fretting loop is presented without the influence of the system compliance.

Table 18 – Stabilized friction coefficient values (displacement).

Displacement (µm)	20	40	50	60
μ_F	0.11	0.12	0.35	0.37

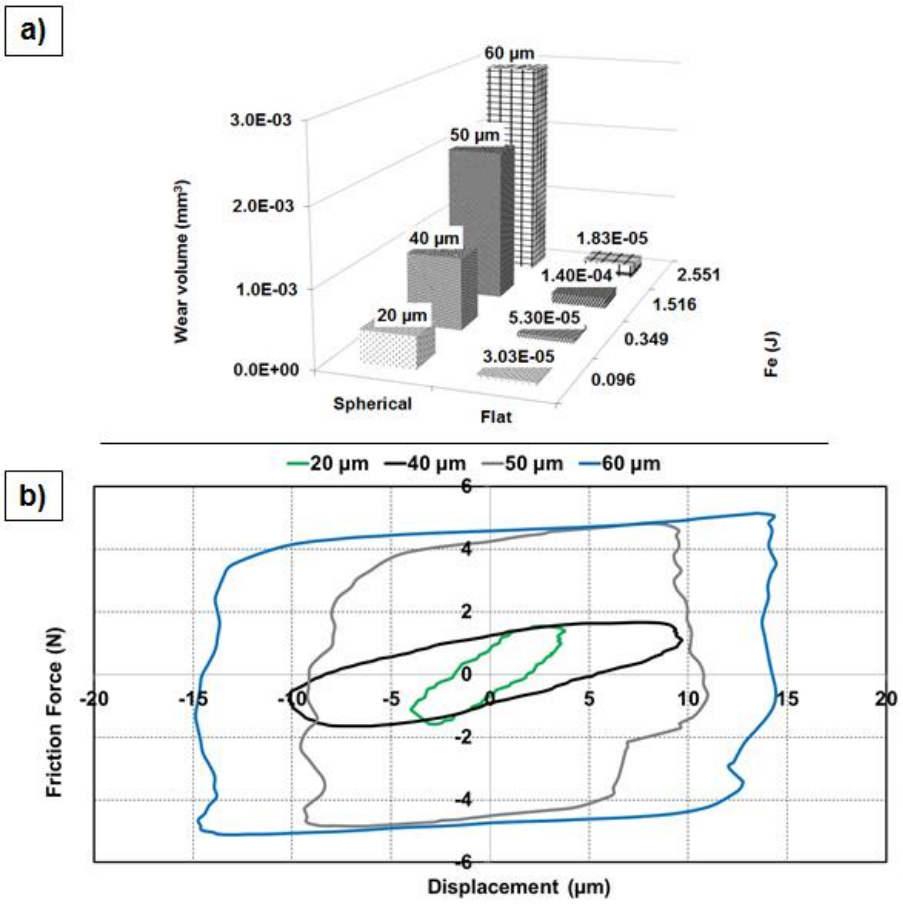

Figure 34 – Representation of: a) – Wear volume versus energy dissipated by friction in different specimens (displacement variation); b) - Stabilized fretting cycle.

The difference between spherical and flat specimens can be seen in Figure 34 – a). Due to geometric conditioning, the wear volume between the flat and spherical specimens differ at least one order of magnitude.

The wear particles from this type of oxide deposit detach from the surface with typically a few microns (Figure 35 – a)), and undergo one of two processes. Some are expelled from the contact zone, gathering in the periphery (Figure 35 – b)) while, other wear debris particles remain between the two surfaces and are compacted into plates (Figure 35 – c)), forming a fragile oxide layer (very brittle) which can perform either as protective or detrimental coats.

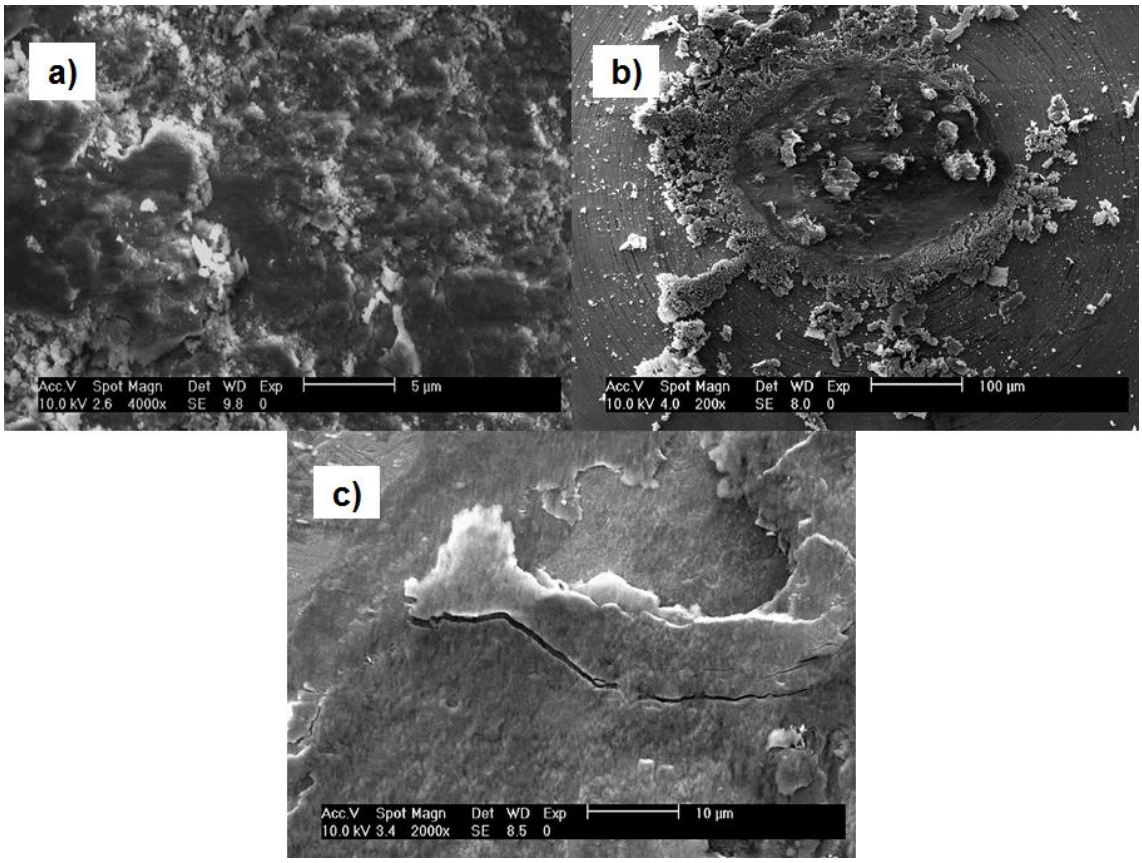

Figure 35 - SEM analysis of surface contact morphologies: a) - Oxide micrometric particles of the 60 µm flat specimen; b) - Oxide micrometric particles of the 50 µm spherical specimen; c) - Oxide plate fracture of the 40 µm spherical specimen.

This compacted layer remains adherent mainly to the flat specimen, which explains the difference of wear amount between the two specimens.

4.1.2. Relative humidity (RH)

The influence of humidity on the friction and wear volume presents some specific trends (Figure 36). There was an reverse trend for friction and wear, Table 19, and so, the energy dissipated by friction decreased when relative humidity was augmented while the totality of material removed by wear rose with the increase of humidity (Fu *et al.*, 2000; Chen *et al.*, 2002; Goto *et al.*, 1984; Baets *et al.*, 1998; Mohrbacher *et al.*, 1995; Cai *et al.*, 2009, Huq *et al.*, 1999).

However, the relation between wear and dissipated energy is not linear. An extreme variation of friction occurred when the relative humidity increased from 10% to 50%, although wear only displayed a significant variation with the increment from 50 % to 85 % of relative humidity (Fu *et al.*, 2000; Goto *et al.*, 1984; Huq *et al.*, 1999).

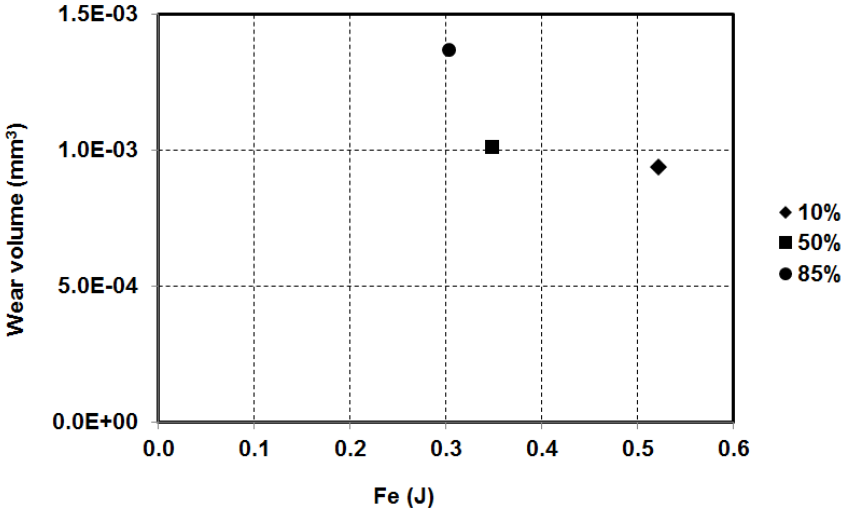

Figure 36 - Wear volume versus energy dissipated by friction for humidity variation.

Coefficient of friction variation (Table 19) corroborates the previously presented evolution but states that the progress of the dissipated energy is not dependent only on the friction coefficient, since the 85% RH test has a higher μ_F than the 50% RH test but a lower dissipated energy. This happens because the slip (sliding) in the 85% RH relative humidity test is lower than in the 50% RH test, mainly due to greater oxidation and oxide deposition on the contact surface.

Table 19 – Stabilized friction coefficient values (relative humidity).

Relative Humidity (%)	10	50	85
μ_F	0.32	0.12	0.18

This is also evident in Figure 37 – a), where the wear of the spherical and flat specimens is presented separately. Since the environment humidity differs, analysis of the debris formed during each test and corresponding oxidation, evidenced by the EDS in Figure 39, shows significant differences, resulting in the formation of various types of iron oxides, typically Fe_2O_3 and Fe_3O_4 (Hirsch *et al.*, 2013).

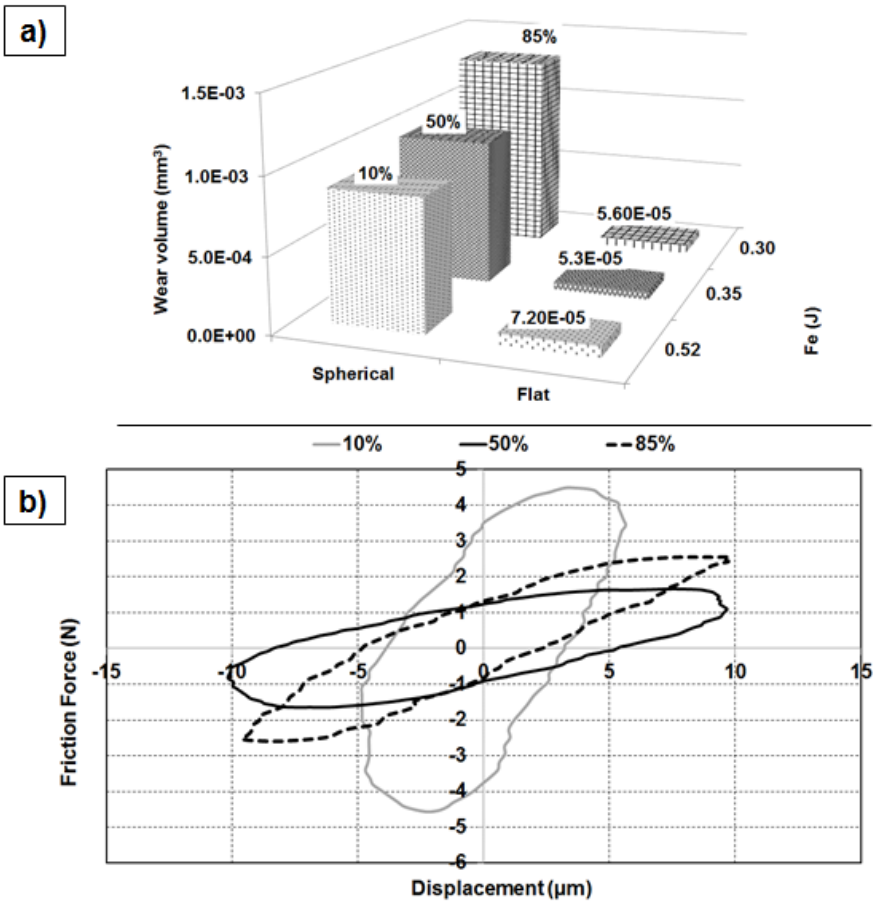

Figure 37 - Representation of: a) - Wear volume versus energy dissipated by friction in different specimens (humidity variation); b) - Stabilized fretting cycle.

Analysis of Figure 38 and Figure 39 of the flat specimens show a high increase of oxygen on the wear zone with a slight decrease of iron and alloying elements, which is a good indication of oxidation but also a reducing tendency on wear volume when a higher humidity is in place. This phenomenon highlighted here was mainly owed to the deposition of debris over the flat specimen surface, result of excessive oxidation with higher relative humidity values.

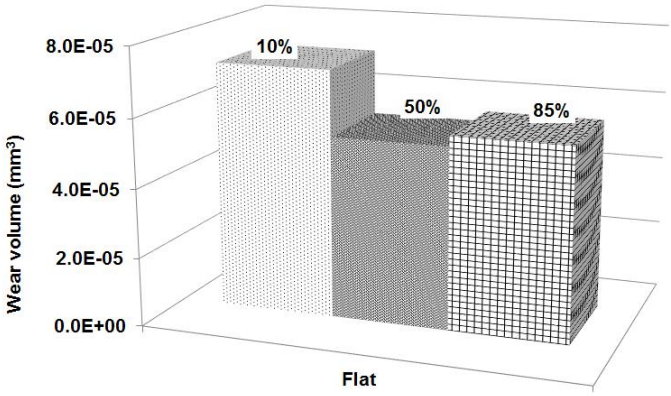

Figure 38 - Wear volume versus energy dissipated by friction in flat specimens (humidity variation).

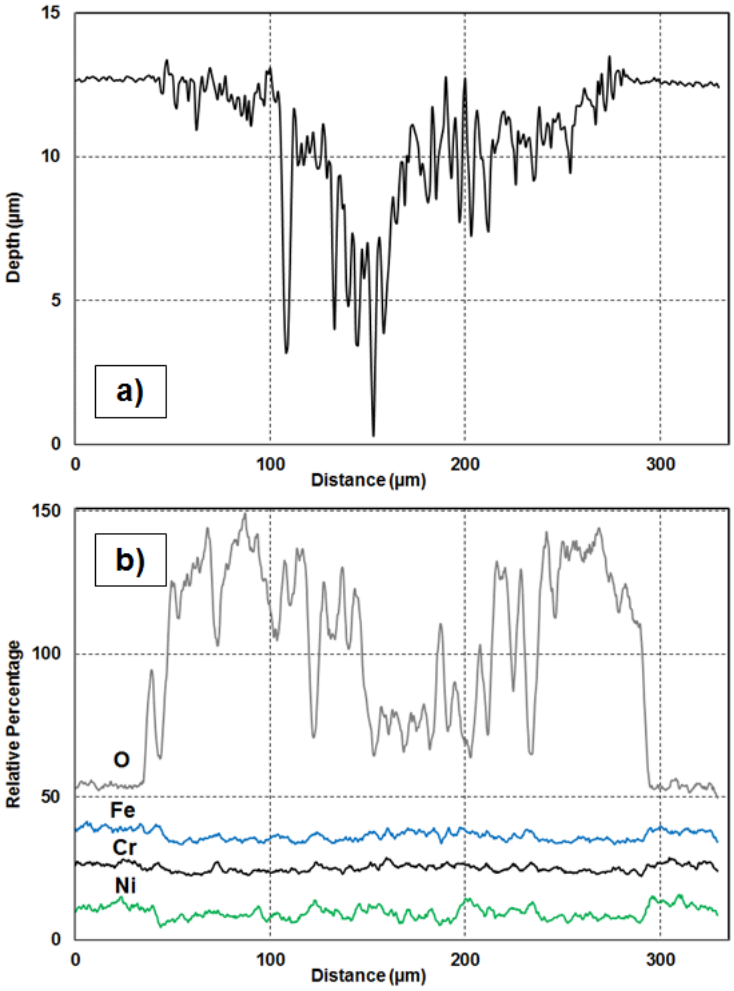

Figure 39 – Cross section profile of the 85% test flat specimen: (a) – depth; (b) - Energy-dispersive X-ray spectroscopy (EDS).

Raman spectroscopy was used in the 50% and 85% RH samples (Figure 40) as a way to understand the oxide layer role. The 50% test specimen contained oxides of Fe_3O_4 (magnetite), and the 85% test specimen revealed the presence of one oxide, Fe_2O_3 (haematite), and one hydroxide, FeO(OH) (goethite). As explained in the introductory chapter, these oxide layers are predominantly formed when the particles detach, rapidly oxidizing, with the most compatible and available elements. Therefore, the higher H_2O available facilitates the oxide formation increasing the wear volume.

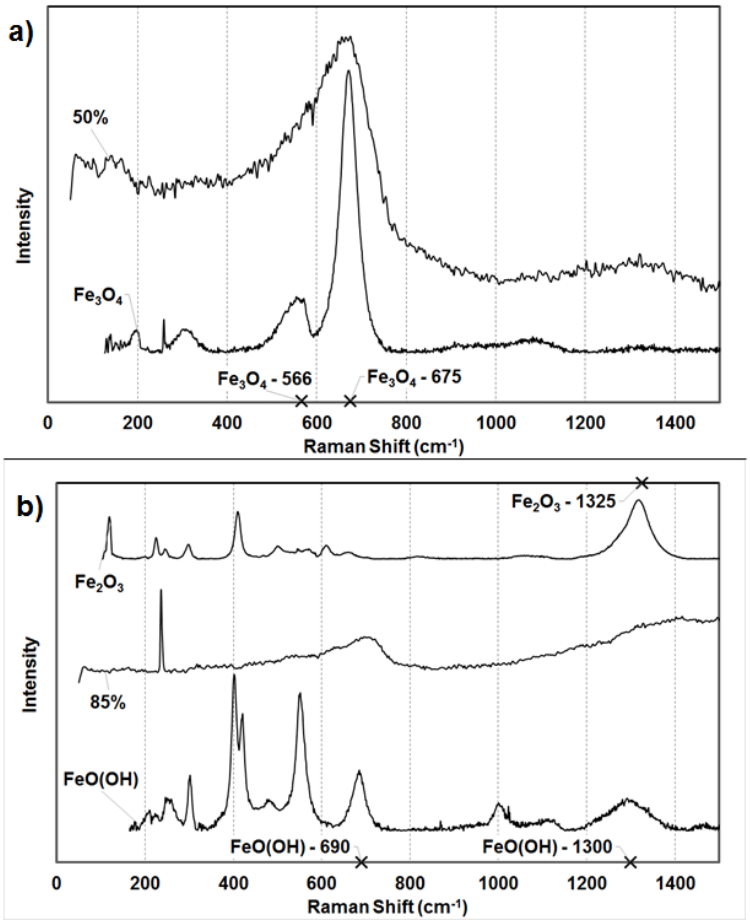

Figure 40 - Raman spectroscopy of a) – 50% specimen and b) – 85% specimen.

The low coefficient of friction and similarity in the 50% and 85% tests was expected since both environments had high humidity, and the very high friction in 10% humidity is also easily explainable. A more pronounced variation is verified on the friction-dissipated energy because of the difference in fretting regime, as detailed in Figure 37 – b). The results obtained revealed that the Fe_3O_4 layer seems be more protective than the layer formed by a mix of Fe_2O_3 and FeO(OH).

4.1.3. Atmosphere variation

Because the oxidation seems to influence the accumulation of material over the contact, the effect of atmosphere was investigated. The reducing and oxidizing atmosphere tests act as limit conditions, since the nitrogen minimises/eliminates oxidation and pure oxygen ensures the very opposite. Figure 41 displays precisely this, where for the reducing atmosphere the wear volume is very low (almost no oxidation, Figure 42 – a) and c)) and also the friction-dissipated energy (high friction coefficient). The oxidizing atmosphere instigated very high wear (due to elevated oxidation, Figure 42 - b) and d) Back-Scattered Electrons (BSE)) and the energy dissipated by friction is also low (dependent on the nature of the oxides) with a high friction coefficient (Table 20). The normal atmosphere (typically 78% nitrogen, 21% oxygen and 1% argon) performed intermediately on wear volume as expected, the only variation being in the friction-dissipated energy field, for the reasons proposed before, all in accordance with the literature.

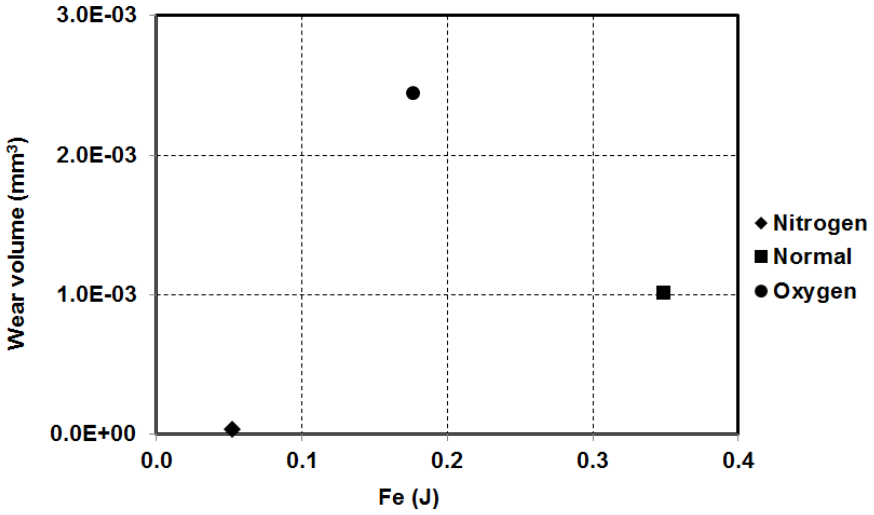

Figure 41 - Wear volume versus energy dissipated by friction for atmosphere variation.

Table 20 – Stabilized friction coefficient values (atmosphere).

Atmosphere	Nitrogen	Normal	Oxygen
μ_F	0.41	0.12	0.43

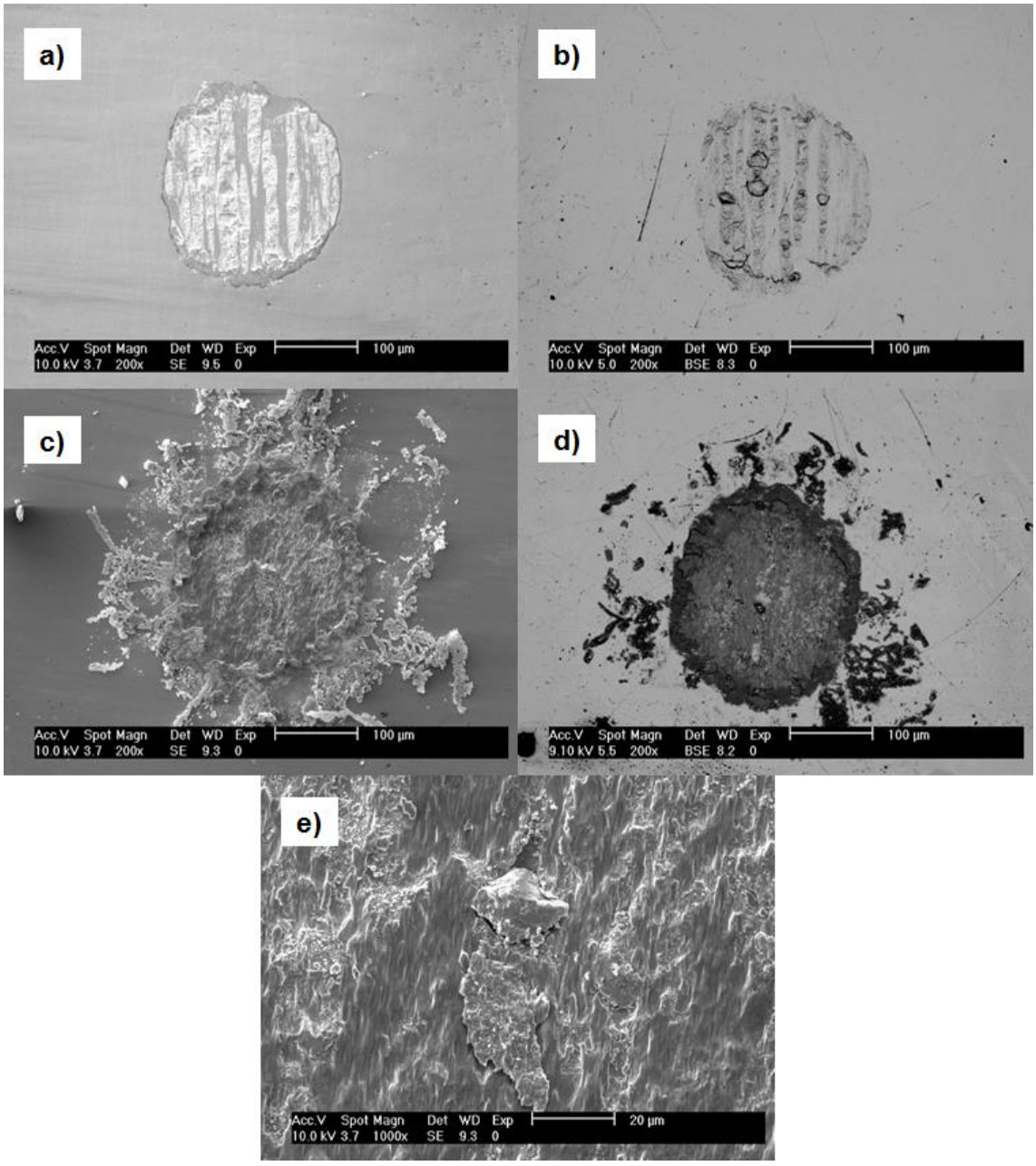

Figure 42 – SEM analysis of surface contact morphologies for: a) - N_2 atmosphere (flat); b) - N_2 atmosphere BSE (spherical); c) - O_2 atmosphere (flat); d) - O_2 atmosphere BSE (spherical); e) - Oxide plate and carbide of the O_2 atmosphere (flat).

The evolution between spherical and flat specimens is presented in Figure 43 – a) and shows the same behaviour in each one. Even so, the spherical specimen in nitrogen atmosphere did not wear at all, suggesting that oxidation is a major factor which reduces friction, increasing the relative displacement and the energy dissipated by friction with further wear growth.

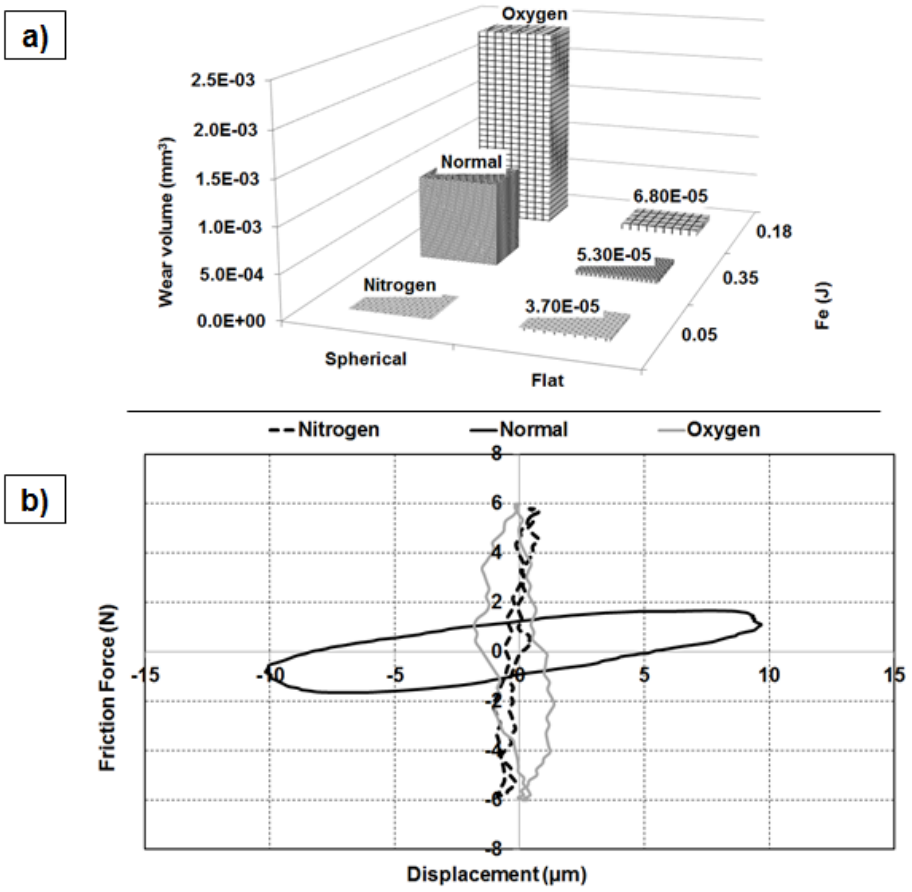

Figure 43 – Representation of: a) - Wear volume versus energy dissipated by friction in different specimens (atmosphere variation); b) - Stabilized fretting cycle.

The fretting cycles shown in Figure 43 – b) justify the evolution of the friction-dissipated energy, with the lowest wear value being the reducing atmosphere and almost no slip.

The very low wear obtained in nitrogen atmosphere should be related to the fact that the loops remain closed with a very low amount of energy dissipated, leaving the contact very close with adhesion. Concerning the oxygen-rich atmosphere, the energy dissipated by friction was also low, but the protective effect of the oxide layers seems to be low because of the looser nature of the oxides increasing the abrasion effect, which was enhanced by the action of the carbides (Figure 42 – e)). This variation of behaviour should be related to the type of oxides formed by the different atmospheres.

The combined analysis of the parameter variation is presented in Figure 44, for wear volume versus energy dissipation.

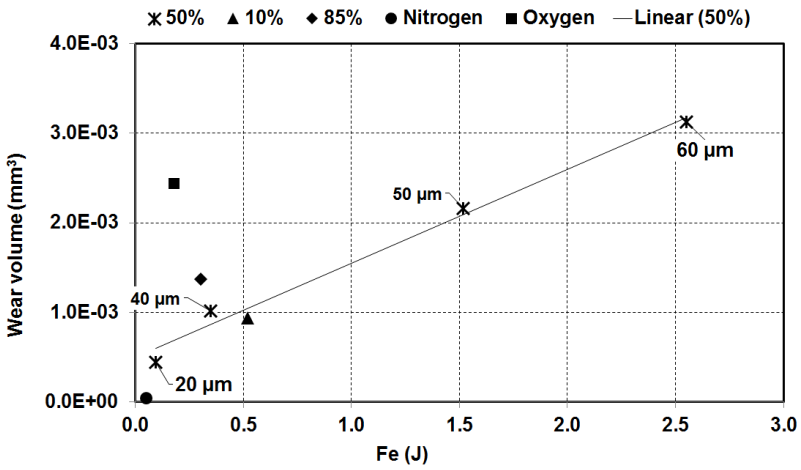

Figure 44 - Wear volume versus energy dissipated by friction for different regimes.

There is a regime separation through the 50% relative humidity line (linear regression of the 50% RH test values). This means that, even with different coefficient of friction variation through the test, the wear volume versus friction-dissipated energy fits a linear evolution very well.

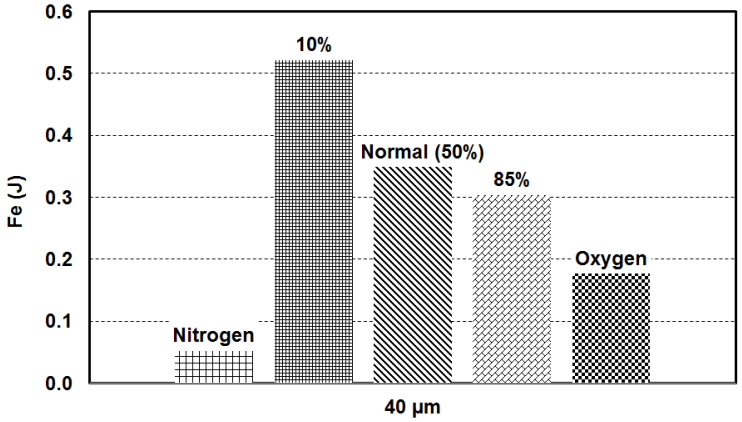

Figure 45 – Friction dissipated energy for the same contact condition tests (40 µm imposed displacement).

The two regimes evidenced are low and high relative humidity. Low RH includes the 10% RH test and reducing atmosphere (nitrogen), in both of which the oxidation is reduced or even eliminated, leading to less wear for the same amount of friction-dissipated energy, as shown in the domain below the linear variation line in Figure 44 and Figure 45. High RH tests are the 85% RH and the oxidizing atmosphere (oxygen) which promote oxidation that

leads to higher values of wear for the same amount of friction-dissipated energy, as shown in the domain above the linear variation line in Figure 44 and Figure 45.

4.2. JOULE EFFECT SYNERGY STUDY

The electric current should increase the immediate contact temperature, as it's well documented and even modelled (Slade, 2014). We could not evaluate experimentally the evolution of the temperature in the contact due to dimension restrictions and because drastic temperature changes are confined to the real contact dimension since the material dissipates reasonably well the heat. Off course, this translates to a very slight increase of temperature regarding the already present friction contribution, concluding in the analysis of partial contribution of energy, but specifically increasing the oxidation of particles.

The current flow in the contact significantly altered the coefficient of friction (Figure 46), increasing it to an average value that was three times higher than that without current flow. However, with a further increase of current from 10 to 120 mA the coefficient of friction remained almost constant.

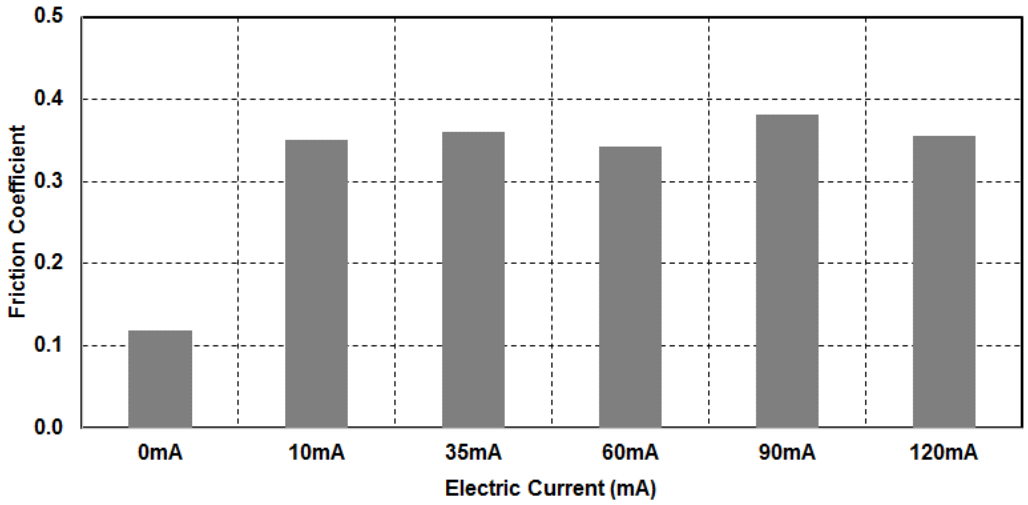

Figure 46 - Friction coefficient evolution with electric current.

Specimens are represented in Figure 47 and Figure 48 for every test condition and both wear-zone images were taken immediately after the tests, therefore containing the majority of wear particles of each trial. There is substantial evidence that the oxidation increases with the addition of electric current.

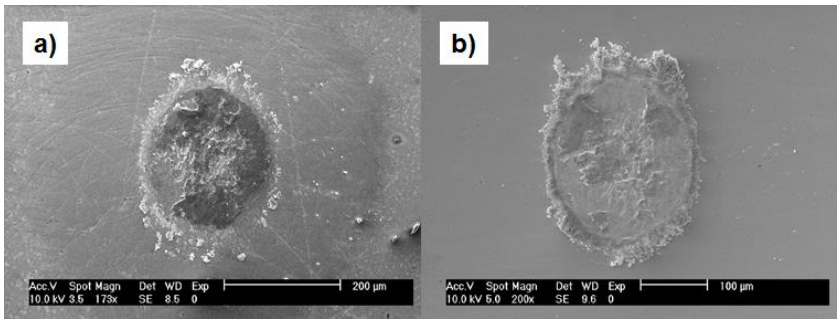

Figure 47 - Wear zones analysed by SEM for 0 mA: a) spherical specimen; b) flat specimen.

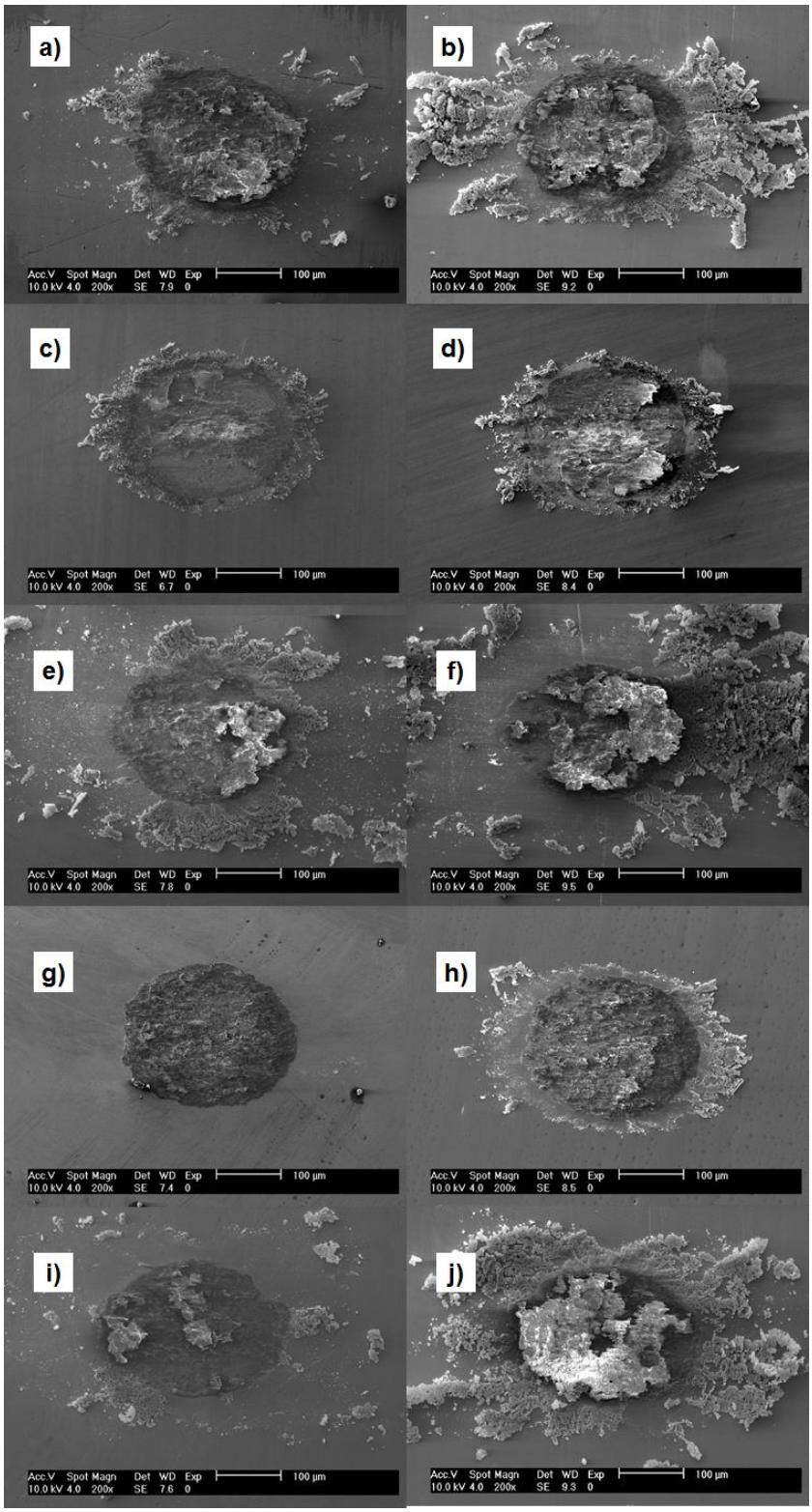

Figure 48 - Wear zones analysed by SEM: on the left spherical specimens and on the right flat specimens. a),b) 10 mA; c),d) 35 mA; e),f) 60 mA; g),h) 90 mA; i),j) 120 mA.

An analysis of the test behaviour and results shows a linear trend of wear with the total dissipation of energy, dissipated by friction added to the Joule effect, (Figure 49), were $k = 4.82 \pm 1.32 \times 10^{-6}$ mm^3/J. The mean value and standard deviation were obtained by a linearization model described in Ramalho, 2010.

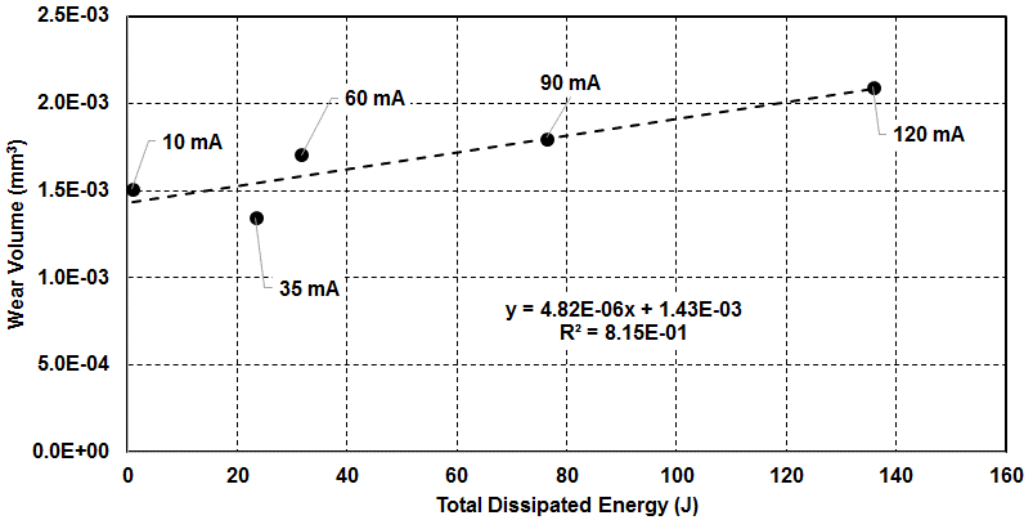

Figure 49 – Total Energy dissipated versus wear volume.

4.2.1. Synergetic model

The addition of energy dissipated by the Joule effect increased the amount of wear in the contact, possibly due to the heat increase on the contact, as might be expected from the current flow. Even so, due to the large increase in the total amount of energy, which increased by the electric current, the wear rate only displays a slight growth, indicating a different contribution from the two energy types. In fact, previous results, Figure 33, show that the effect of the energy dissipated by friction is around three orders of magnitude higher than the energy dissipated by the Joule effect. This can be seen from the difference in the wear rate, where the total amount of energy dissipated in the contact is $k = 4.82 \times 10^{-6}$ mm^3/J and the slope has the tendency presented in Figure 49, while the energy dissipated by friction alone is $k = 1.05 \times 10^{-3}$ mm^3/J, as observed in Figure 33. This means that, considering the same amount of energy, much more wear is produced if the energy was dissipated by friction.

When the complete linear trend of the wear is analysed, slope and the *Y* axis intercept, the law from friction dissipated energy alone, Figure 33, the *Y* axis intercept is ten times lower than the slope (wear rate) allowing the dismissal of the intercept term. That is not the case when energy dissipated by joule effect is included, where the *Y* intercept is three orders of magnitude higher than the slope on Figure 33, meaning it cannot be dismissed and demands a physical clarification.

So, to better understand the synergetic effects, the joule effect contribution to wear was separated from the friction contribution using a synergetic approach common in tribo-corrosion studies as seen in Mischler, 2008. In the present case the total wear volume will be the summation of the mechanical wear (friction), V_F, a joule effect parcel of wear, V_J, and an incremental factor of degradation due to the combined effect, ΔV_E, Equation (9), alas resulting in a synergetic model.

$$V_T = V_F + V_J + \Delta V_E \tag{9}$$

Concerning the equation (9), it should be ideal to forecast the evolution of the wear volume (V_T) on a contact with fretting motion and current passing. Provided that friction can be well defined, friction dissipated energy will be determined resorting to equation (7 methods), the V_F parcel always previously independently determined. The strategy established to calculate the remaining two parcels of the synergetic model was the discrimination of (V_J+ΔV_E) from equation (9) and by means of the experimental dataset correlation, test a good interpolating function.

In Table 21 is presented a decomposition or identification of the model effects contribution based on the different apportions of energy contributions, where friction and joule effect energy are isolated from each other.

The separation of friction contribution to wear, equation 10, and synergetic model joule effect parcel of wear plus incremental factor due to the combined effects, equation 11, are shown in the last columns Table 21.

$$V_F = (1.05 \times 10^{-3}) \times F_e \tag{10}$$

$$V_J + \Delta V_E = V_T - V_F \tag{11}$$

Table 21 – Wear contribution decomposition.

Test Current (mA)	E_T (J)	F_e (J)	J_e (J)	V_T (mm^3)	V_F (mm^3)	$V_J+\Delta V_E= V_T- V_F$ (mm^3)
10	0.79	0.49	0.29	1.51×10^{-3}	5.19×10^{-4}	9.92×10^{-4}
35	23.29	0.26	23.03	1.35×10^{-3}	2.72×10^{-4}	1.07×10^{-3}
60	31.62	0.61	31.01	1.71×10^{-3}	6.44×10^{-4}	1.06×10^{-3}
90	76.33	0.30	76.03	1.80×10^{-3}	3.16×10^{-4}	1.49×10^{-3}
120	135.81	0.72	135.10	2.09×10^{-3}	7.51×10^{-4}	1.34×10^{-3}

Figure 50 represents the joule effect parcel of wear and incremental factor due to the combined effects, respectively the joule effect wear rate k = 3.15 × 10^{-6} mm^3/J and incremental factor of 1.02 × 10^{-3} mm^3/J previously justified. The number of experimental data points is quite reduced, but the use of a linear trend line seems to be reasonably supported.

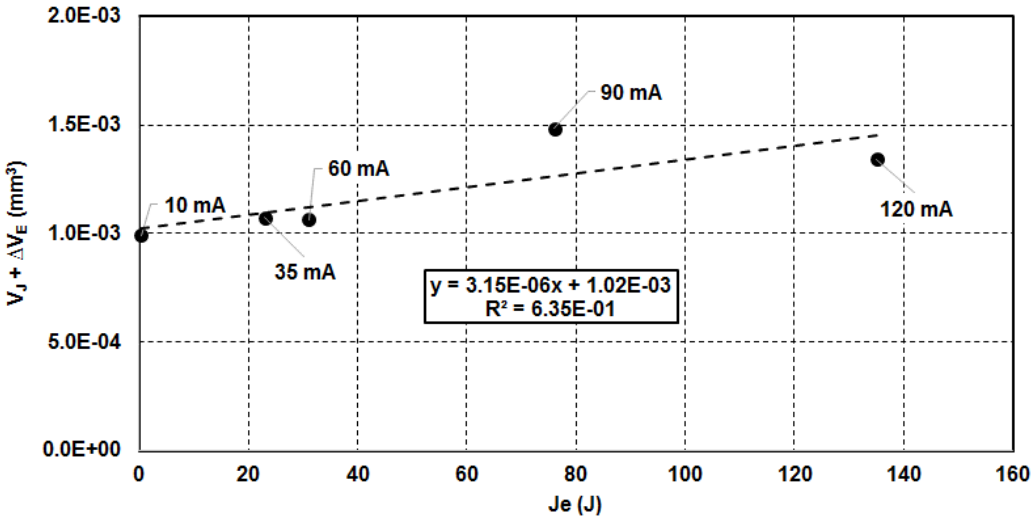

Figure 50 – Wear volume versus energy dissipated by joule effect contribution.

Regarding a similar linearization model, the wear rate mean and standard deviation is k = 3.15 ± 1.38 × 10^{-6} mm^3/J. When the wear coefficients of the two singular contributions to wear are compared, it is obvious that the input of joule effect energy is three orders of

magnitude lower than friction contribution. Even so, the incremental factor is of the same order of magnitude than the friction contribution and this addition to wear is the action of just adding electric current to the contact.

The contribution of energy to the total amount of wear is parcelled in Figure 51 and the very different contributions of the synergetic approach model can be identified. The validation of the synergetic model is tested through the delimitation of each parcel contribution against the experimental wear results.

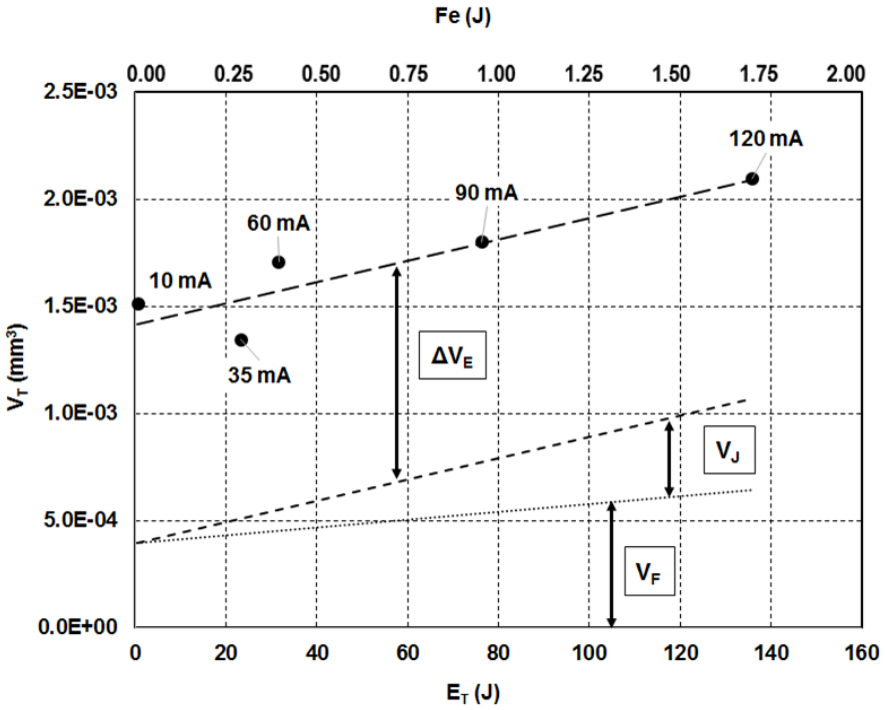

Figure 51 - Synergetic approach parcel contribution to total wear volume.

Therefore, to predict the wear generated in this type of contacts subjected to electrical current the following equation can be used.

$$V_T = (1.05 \times 10^{-3}) \times F_e + (3.15 \times 10^{-6}) \times J_e + 1.02 \times 10^{-3} \qquad (12)$$

Detailed observation of the contact surfaces by SEM revealed that the wear was governed by surface oxidation (Figure 48, Figure 52). However, in some cases, the oxidized particles form more adherent platelets, which are highlighted on the figures for the tests at 35 and 90 mA. The other test conditions displayed more dispersed particles around the

contact. The EDS analysis of the wear debris, Figure 52, showed the same type of ferrous oxides as previous works (Esteves *et al.*, 2015), Fe_2O_3 and Fe_3O_4 and very low content of chromium, deriving from the alloy content because, as previously stated, even with a high chromium content on the alloy the amount of iron in the composition is far greater and available for the immediately formed wear particle. Analysis result was very similar in every test, from EDS to presentation and morphology.

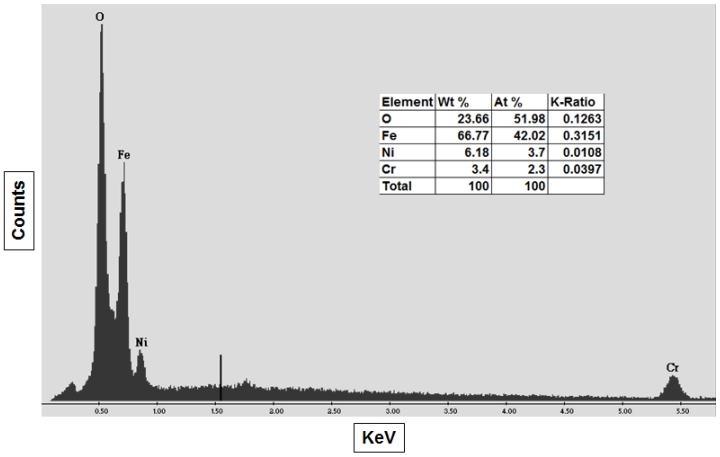

Figure 52 - EDS analysis of the 10 mA test.

Further analysis of the evolution of electric resistance during tests (Figure 53) also shows an increasing tendency, especially two tests at 35 and 90 mA, which present the most atypical behaviour and higher mean values (Table 22).

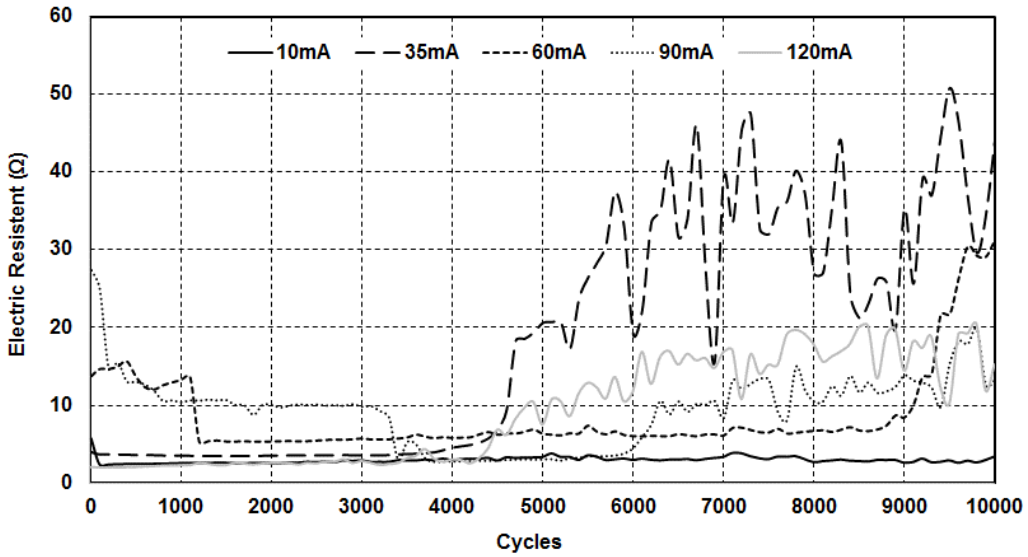

Figure 53 – Evolution of Electric Resistance during the tests.

The higher values of resistance (Table 22) originate from the debris density and presence in the contact for those specific tests.

Table 22 – Mean electrical resistance value.

Test Current (mA)	10	35	60	90	120
Resistance (Ω)	2.97	18.65	8.66	9.56	9.31

It is perceptible that the types of oxides present in the contact dictate the major behaviour aspects of the contact, from wear to electric performance. Looking at the 35 and 90 mA tests, SEM observations show an oxide layer that is much more compact and close to contact, leading to increases in friction and electric resistance (Figure 46 and Figure 53; Table 22). This oxide layer is harder to remove and promotes lower slip with a higher friction coefficient, revealing a smaller contribution of energy dissipated by friction (Table 21) and decreasing wear loss (Figure 49). Even with these constraints, the difference in electric current is too high to alter the evolution of total energy dissipated, leading to a more or less linear tendency.

Finally, the synergetic effects between friction-dissipated energy and energy dissipated by the Joule effect are pinpointed in the previous analysis. From the wear representation it is obvious that the increase of the electric current has a cumulative effect, adding to the friction energy effect (Figure 49) but altering the cumulative energy trend.

When an amount of energy similar to that dissipated by the Joule effect is added to the friction parcel, there is an immediate increase of wear due to the rise of temperature and consequent rapid oxidation of the wear particles (incremental factor of degradation due to the combined effect just by adding a minimum amount of current). Although the addition of a similar amount of energy promotes rapid wear growth, the continual rise in wear values can only be obtained by a very high increase in the electric current and consequent Joule effect energy (low contributing joule effect parcel of wear). The main reasons for this performance are the low and indirect influence of the sliding contact parameters from the electric current flow, which is the main governing mechanism for particle detachment, rearrangement, and removal. In further detail, the contribution of friction dissipated energy is, in the present situation, divided in to plastic deformation, with a major role, and particle oxidation, with a minor role, whereas the joule effect energy can contribute only to the oxidation. Actually, the assumption will be that energy dissipated by joule effect, because of the higher amount, would increase temperature (some oxidation and wear) proportionally but the fact is the energy density should be lower, when compared to friction contribution, because is much more distributed on the entire contact as opposed to the localized situation caused by stress distribution on the contact (not uniform).

This slight increase depends on the increasing oxidation rate, a consequence of the early contact temperature rise, which in turn increases the electrical resistance and coefficient of friction due to the availability and chemical composition (Figure 53). Because the Joule effect energy has little control over the sliding phenomenon, the rise of the electric current and consequent oxidation can induce very rapid impedance growth if a steady state of particle removal is established. This tends to worsen with compaction of wear particles comprised within the contact [(Figure 48 (c), (d), (g), (h)], reaching undesired impedance values, which in turn can cause system breakdown or electric current surge.

4.3. TEXTURE EFFECT STUDY

As mentioned on the previous section, due to the size and the uneven nature of the contact surfaces the wear volume was not considered for evaluation. Be that as it may, wear conditions of the surface were analysed and benchmarked alongside with the more significant parameters like friction coefficient, friction energy dissipation and electric resistance.

The performance evaluation on the contact pairs was divided into three control groups, where, by means of an elimination process, the comparing conditions were selected using the first group as launch scenario.

4.3.1. Contact radius effect

There is an obvious influence of contact radius on the electric performance in these type of contacts. As seen in Figure 54 and Table 23, a higher sphere radius increases the resistance during the test, reaching a catastrophic failure very soon, a resistance of at least 1 kΩ. Setting the first test of the group as standard, the increase of sphere radius rises the average impedance difference from 35% to 250%.

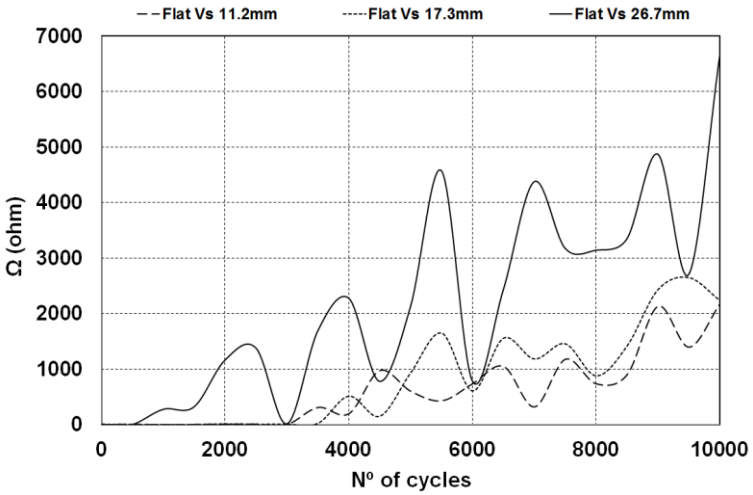

Figure 54 - Electric resistance variation for group 1 comparison.

Friction dissipated energy, present in Table 23, show a decreasing tendency with higher radius caused primarily by the difference in the initial slip conditions of the tests since the fretting cycles and friction coefficient are analogous on all conditions. This is also evident in the resistance evolution chart, Figure 54, as for it controls the tribological transformed layer formation.

Table 23 - Group 1 resistance and friction energy.

	Flat Vs 11.2 mm	**Flat Vs 17.3 mm**	**Flat Vs 26.7 mm**
R_{max} (Ω)	2176.0	2648.7	6641.3
$R_{average}$ (Ω)	658.0	885.9	2304.8
ΔR_{avg} (%)	0%	35%	250%
F_e (J)	6.50×10^{-1}	6.43×10^{-1}	6.12×10^{-1}
μ_F	0.18	0.20	0.17

A thorough analysis on the fretting cycle loops, Figure 55 – c), for the stabilized regime show an almost identical behaviour on every condition leaving the only remaining variable the contact dimension, for controlling the resistance. In other words, with increasing contact size, the available contact area is higher, however, with the same displacement a larger contact area is not as efficient expelling wear debris and renovating the contact surfaces.

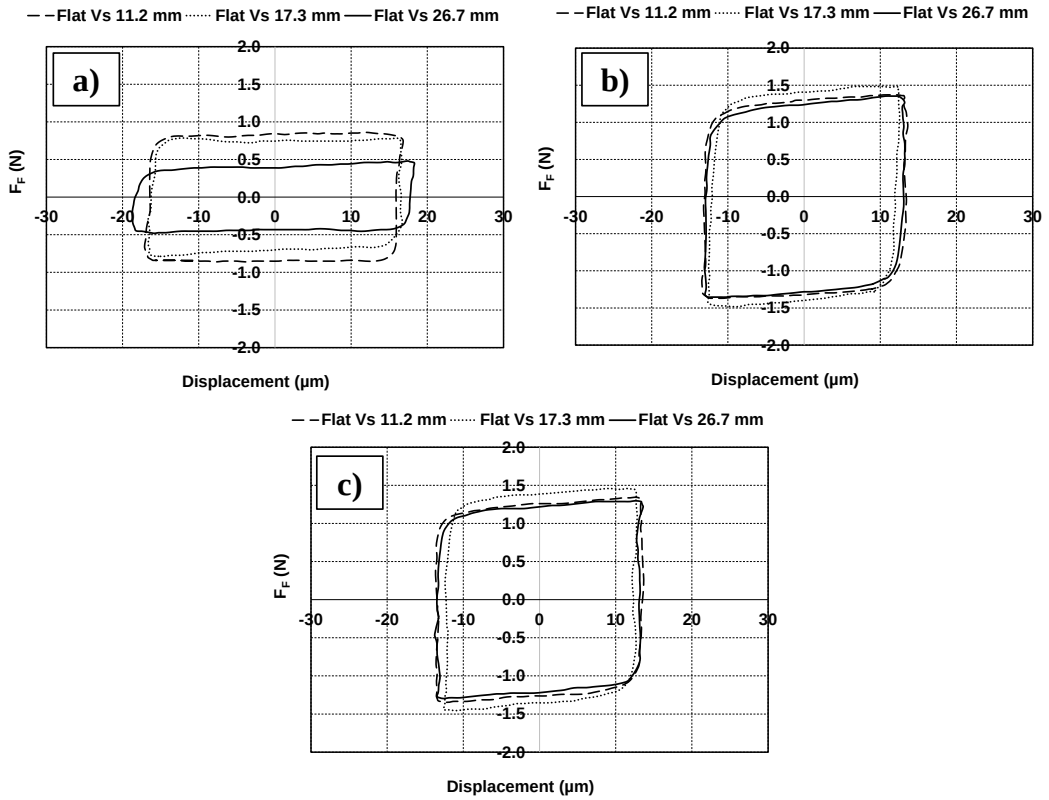

Figure 55 – Group 1 comparison fretting cycles for: a)- Cycle nº 100; b)- Cycle nº 5000; c)- Cycle nº 10000.

Concerning the relation between electric resistance and oxidation, there was an evident behaviour for all the tested conditions on every group, tight to the waviness of the resistance evolution curves and development of oxide layer. A series of elemental analysis were performed in all the groups tested with similar results, as shown in Figure 56, so it is expected to obtain ferrous oxides, also found in a previous work (Esteves *et al.*, 2015).

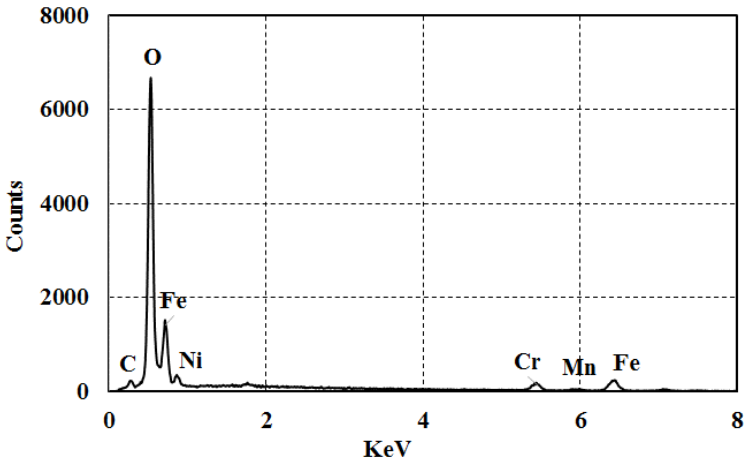

Figure 56 - Energy-dispersive X-ray spectroscopy (EDS) for the flat against 10 mm sphere.

As seen in (Sauger *et al.*, 2000), the evolution of the TTS (tribological transformed structure) is a continuous and complex process based on the dynamics and specifications of the contact. In a simplified manner, Figure 57 transpires the formation and growth of the oxidized layer initiated in, step I; with low wear and resistance, step II; first detachment of debris from the contact and residual resistance, step III; oxidation of the detached debris almost immediately and compacting leading to fragile structures (high resistance) and, step IV; fracture of the oxide layer by friction induced stresses and instantaneous resistance reduction (waviness), continuing always with a cumulative tendency.

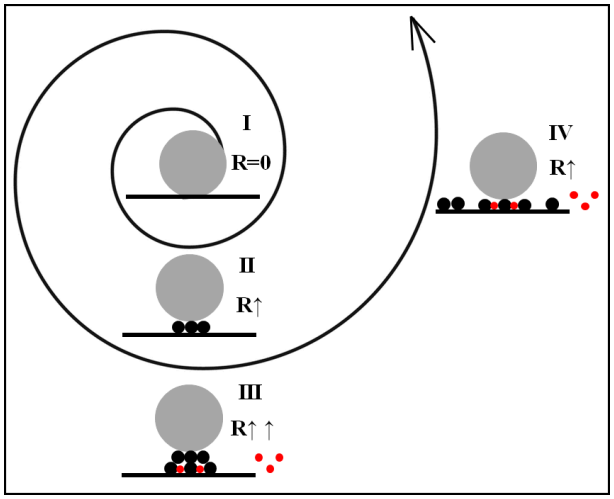

Figure 57 – Simplified tribological transformed structure evolution schematics. I – Clean contact; II – Fist debris formation (particle detachment); III – Debris oxidation (oxygen in red) and layer growth; IV – Fragile layer detachment.

4.3.2. Effect on contact radius

The purpose of introducing the texture into the flat surface geometries was mainly to take advantage of blank spaces or dead volume between the dimple contacts and the counter body while maintaining a large number of independent contacts, at least more than one.

Figure 58 shows the electric resistance evolution for different sphere radius against the less dense texture. It stands out immediately the ability of any textured surface delaying the increase of resistance reaching much lower values during the tests, if compared to untextured case. Maximum and average values, Table 24, also induce the same conclusion being at least half the value of the flat surface. Setting the first test of the group as standard, it is noticeable an evident decrease on average impedance, at least 50% up until 80%.

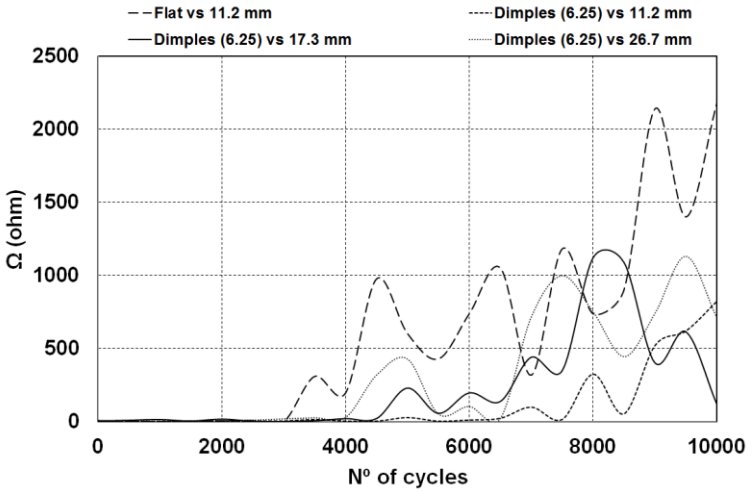

Figure 58 – Electric resistance variation for group 2 comparison.

This behaviour is especially due to free volume available in between the dimples, which maintain a clean metallic contact with the sphere. The free space allows the particles an easier expulsion out of the contact and accommodation of wear debris stopping any interaction of said particles with electric current flow. The same phenomenon can also partially explain why there is also an increase of electric resistance for higher sphere radius since, as seen in Figure 59, the proximity between independent contact points can and will exhaust the near available free space.

Table 24 - Group 2 resistance and friction energy.

	Flat Vs 11.2 mm	**Dimples (6.25) Vs 11.2 mm**	**Dimples (6.25) Vs 17.3 mm**	**Dimples (6.25) Vs 26.7 mm**
R_{max} (Ω)	2176.0	820.3	1119.1	1132.1
$R_{average}$ (Ω)	658.0	126.5	241.5	324.6
ΔR_{avg} (%)	0%	-81%	-63%	-51%
F_e (J)	6.50×10^{-1}	5.78×10^{-1}	6.10×10^{-1}	6.22×10^{-1}
μ_F	0.18	0.19	0.19	0.20

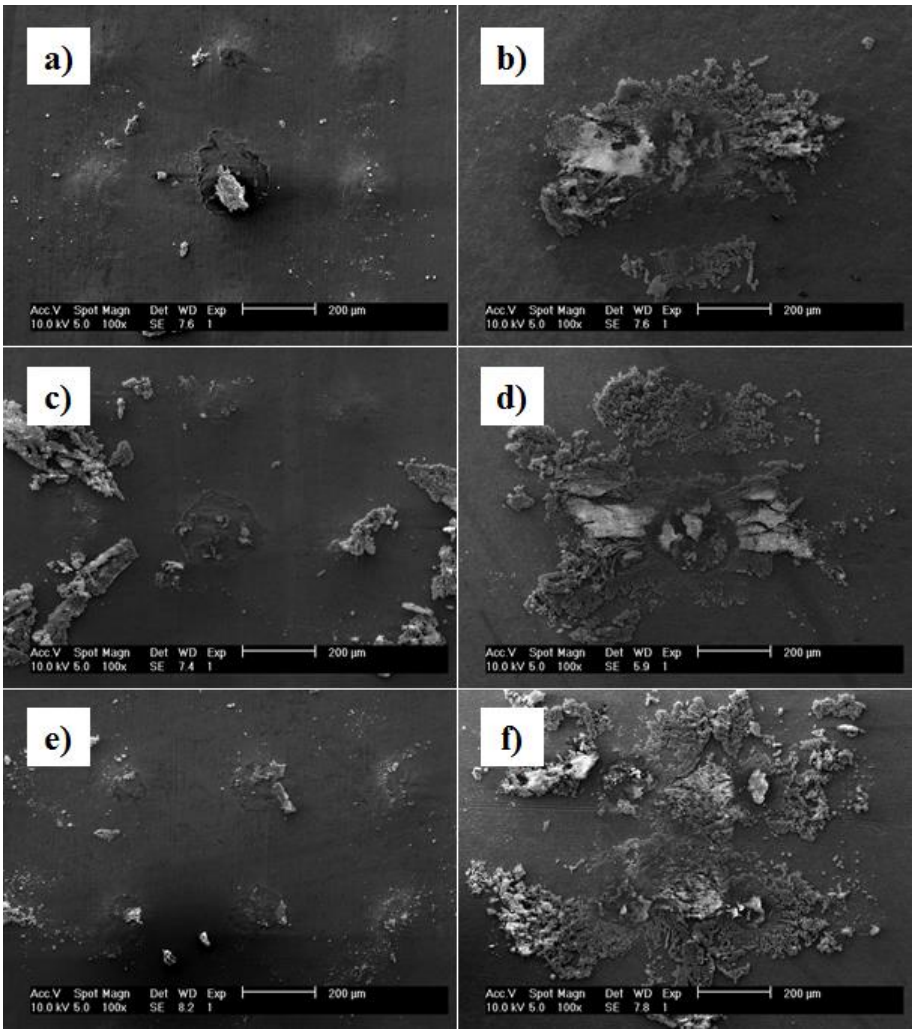

Figure 59 – SEM wear marks: a)-textured (dimples (6.25); 11.2 mm); b)-sphere (dimples (6.25); 11.2 mm); c)- textured (dimples (6.25); 17.3 mm); d)- sphere (dimples (6.25); 17.3 mm); e)- textured (dimples (6.25); 26.7 mm); f)- sphere (dimples (6.25); 26.7 mm);

A doubt remains on why a larger radius would get a worse electrical performance and even a higher friction dissipated energy. A detailed analysis of the instantaneous evolution of the friction dissipated energy, Figure 60, denote a faster rise of the dissipated energy for larger radius and confirmed in the fretting loop comparison, Figure 61. In fact, it would be expectable that with more individual contacts, so higher number of dimples, the contact pressure would be lower, however, since the contact rigidity is higher the same displacement input will cause a larger energy dissipation particularly in the initial cycles, assuming an Hertzian contact is in place, Figure 60 and Figure 61.

From here, the assumption that the number of independent contacts, Figure 59, alters the slip conditions of the contact pair takes shape, which can be demonstrated by the sudden

increase of energy dissipated and consequent electric resistance around 5,000 cycles for the texture and a 11.2 mm diameter sphere test, Figure 58 and Figure 60, corresponding to the addition of one more dimple to the contact, the one almost without wear in Figure 59 – a).

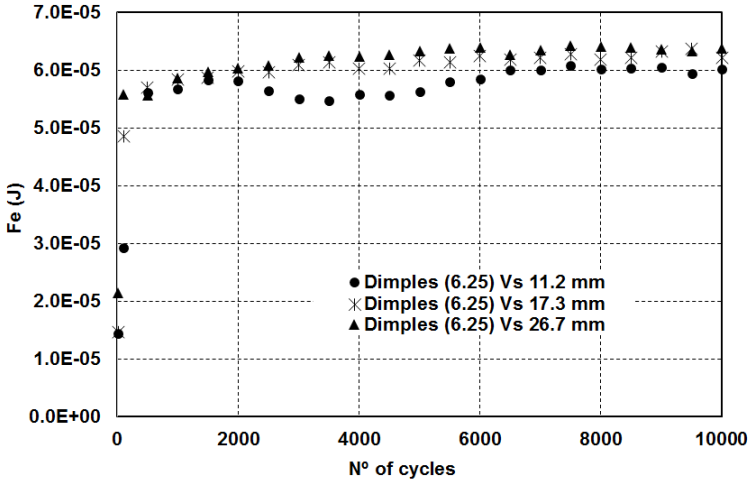

Figure 60 – Friction dissipated energy per cycle for group 2 comparison.

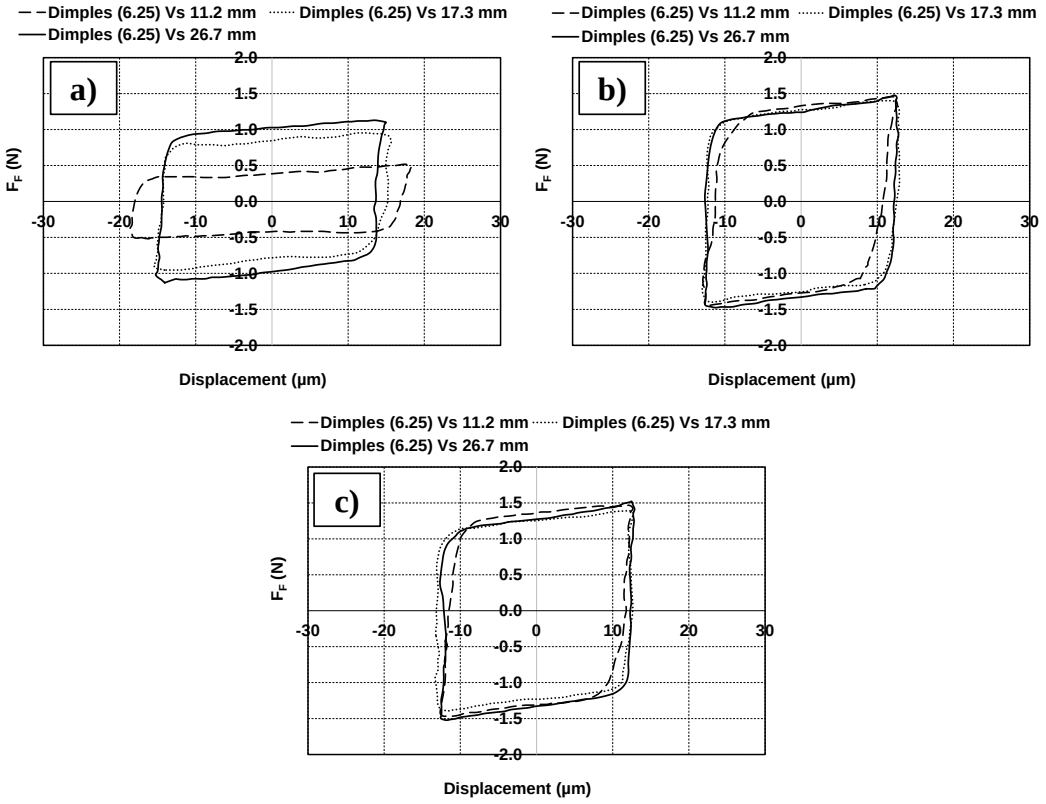

Figure 61 – Group 2 comparison fretting cycles for: a)- Cycle nº 100; b)- Cycle nº 5000; c)- Cycle nº 10000.

4.3.3. Effect of density and negative texture

Since the initial conviction was that a greater number of individual contacts would benefit the connection performance, the need of adjusting the density of dimples without increasing the sphere radius arises. Likewise, is the need to counterpoise these influences with a negative texturing, inversed or hollowed, which in theory can also act as particle accumulation pockets.

After a careful analysis of the group 3 performance, Figure 62 and Table 25, it is clear that beneficial effects can be achieved with both solutions. Setting the first test of the group as standard, that in this case refers to the less dense positive texture, the improvement is not present in all the other textures as a dense texture and inverted off the standard can improve the impedance resistance from 35% to 45% but is not the case inverted dense texture with an increase of average impedance of 242%.

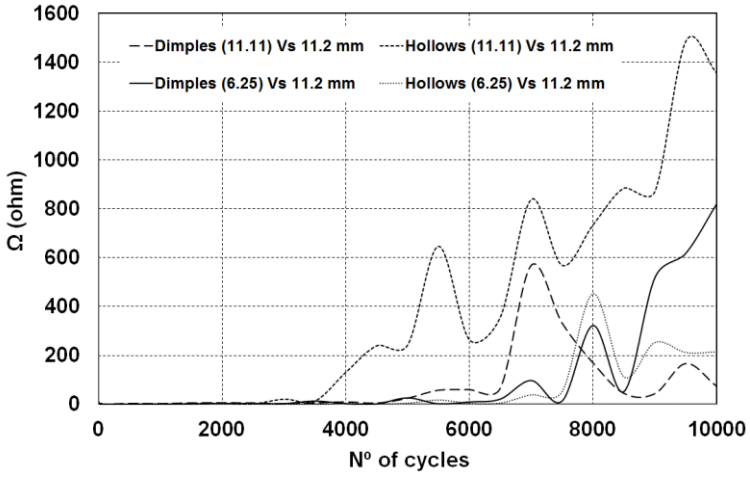

Figure 62 - Electric resistance variation for group 3 comparison.

Table 25 - Group 3 resistance and friction energy.

	Dimples (6.25) Vs 11.2 mm	**Hollows (6.25) Vs 11.2 mm**	**Dimples (11.11) Vs 11.2 mm**	**Hollows (11.11) Vs 11.2 mm**
R_{max} (Ω)	820.3	451.7	568.2	1485.7
$R_{average}$ (Ω)	126.5	69.6	82.1	433.1
ΔR_{avg} (%)	0%	-45%	-35%	242%
F_e (J)	5.78×10^{-1}	5.13×10^{-1}	4.42×10^{-1}	6.13×10^{-1}
μ_F	0.19	0.16	0.17	0.17

Thoroughly analysing the denser test behaviour, it is acknowledged the ability to extend the life of the electric connection although with low values of friction dissipated energy. As it stands out, the effect of multi-contact is intensified by an increased number of contacts, Figure 63 – e) and f), very close to each other, with a uniform wear distribution on the worn dimples and almost clean new contacts which decreased the resistance to the end of the test, Figure 62.

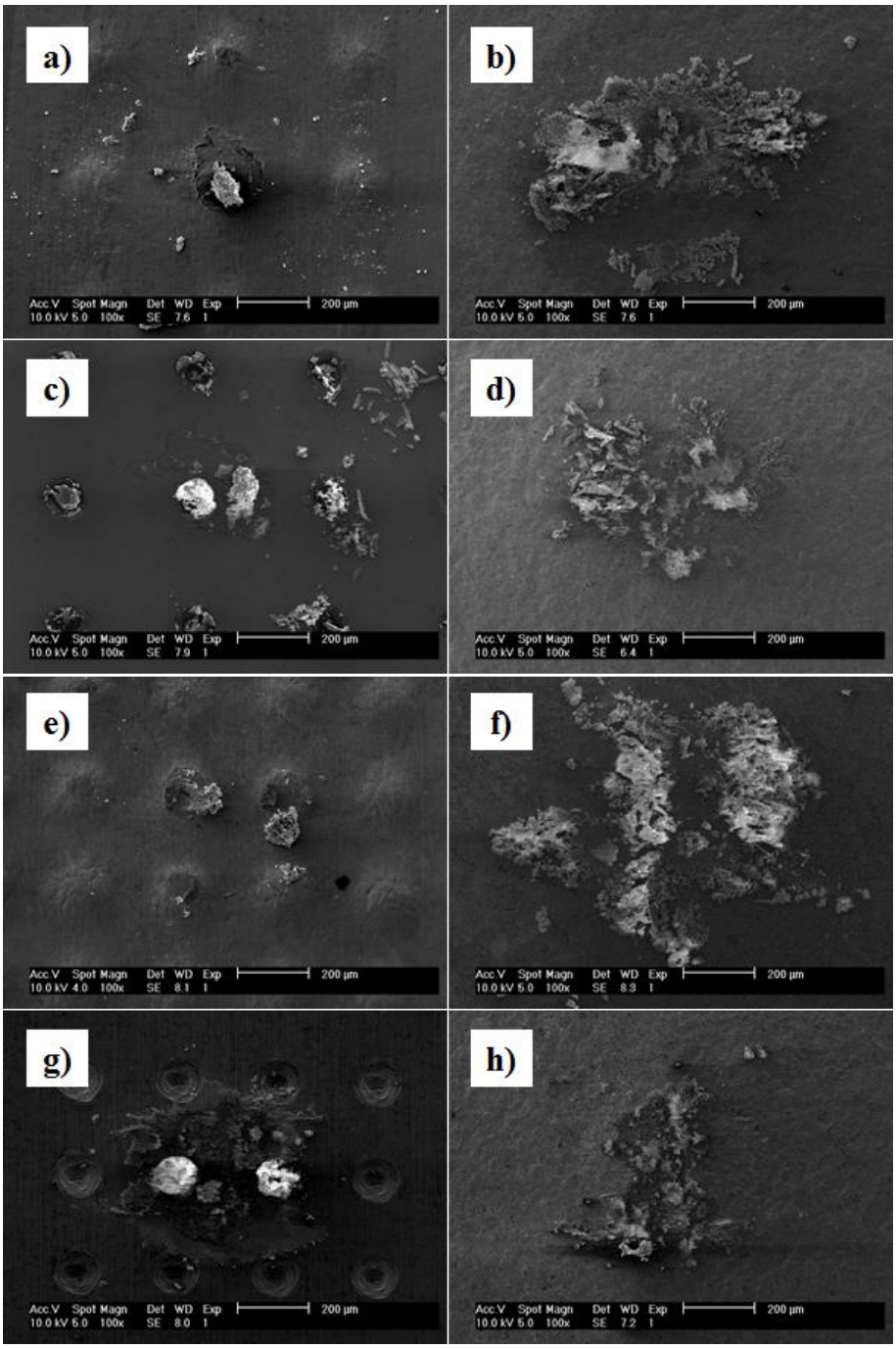

Figure 63 – SEM wear marks: a)-textured (dimples (6.25); 11.2 mm); b)-sphere (dimples (6.25); 11.2 mm); c)- textured (hollows (6.25); 11.2 mm); d)- sphere (hollows (6.25); 11.2 mm); e)- textured (dimples (11.11); 11.2 mm); f)- sphere (dimples (11.11); 11.2 mm); g)- textured (hollows (11.11); 11.2 mm); h)- sphere (hollows (11.11); 11.2 mm);

Consequently, this cluster of events decreased the dissipated energy by means of higher friction by interlocking effect, noticeable on the evolution of dissipated energy *per*

cycle of Figure 64 and the fretting loops of Figure 65 that show sloping cycles, lack of friction saturation, for the denser test.

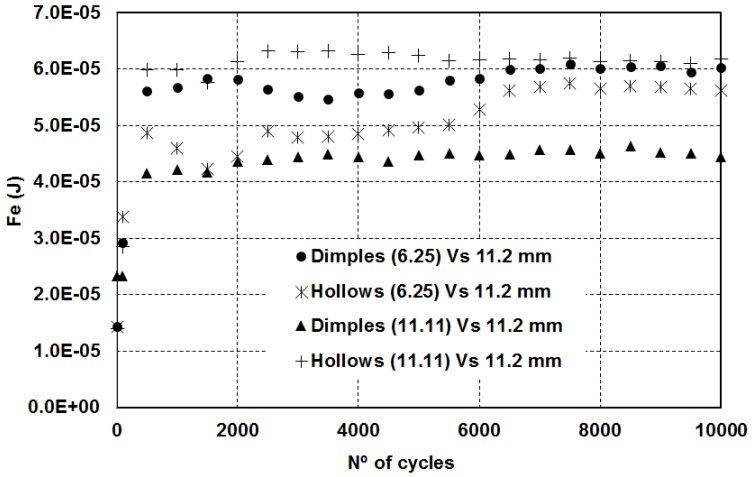

Figure 64 – Friction dissipated energy per cycle for group 3 comparison.

Finally, the reason behind the discrepancy of the inverted textures was identified as the contact surfaces and dissipated energy evolution were observed. Just by observing Figure 63 one can see that the less dense inverted texture test contact surfaces are not as well delimited as the denser ones, scattered versus agglomerated debris, respectively. The contact area present clean zones in the first case but not in the second. Knowing that they possess a similar contact area, same size sphere, the proximity of the depressions of a denser texture caused the rapid depletion of empty space saturating the contact adding the limiting effect of the nearer depressions as no contact zones, marked as red circles in Figure 66. The excess oxides promoted high slip and consequent accumulated dissipated energy.

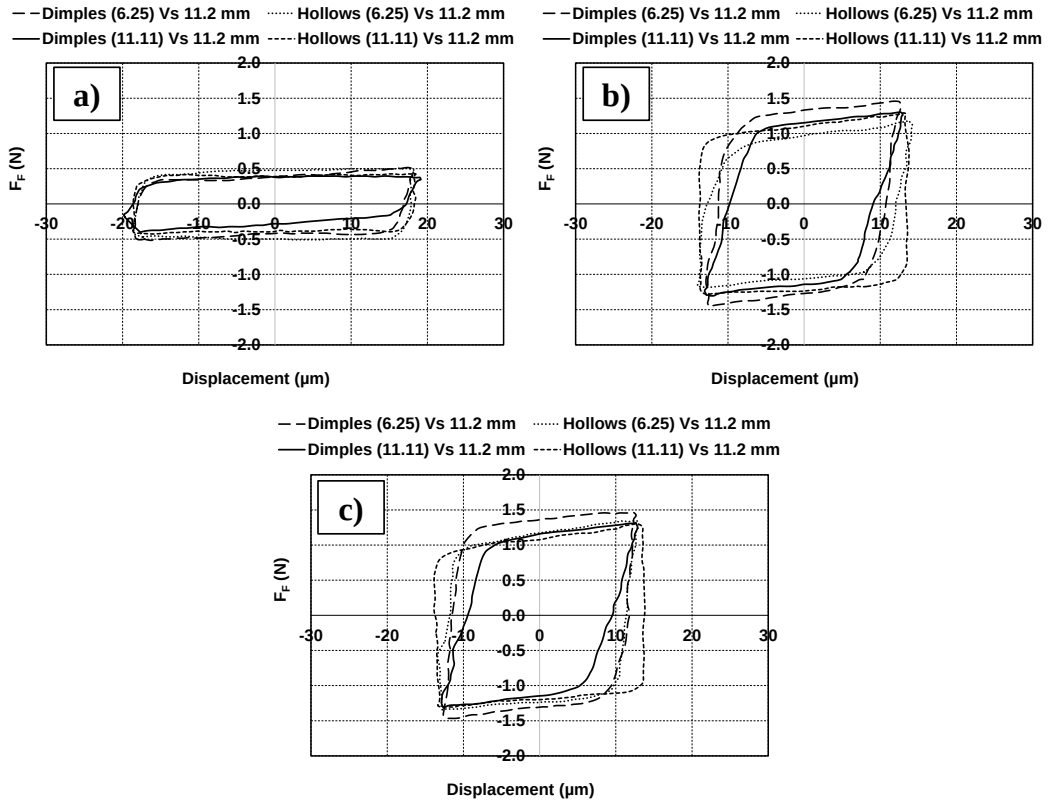

Figure 65 – Group 3 comparison fretting cycles for: a)- Cycle nº 100; b)- Cycle nº 5000; c)- Cycle nº 10000.

The best performance test is a little difficult to identify since both the denser texture test and less dense inverted texture test showed good behaviours. The decisive circumstance would then be the final cycle's performance which can indicate a longer test would benefit the denser texture solution.

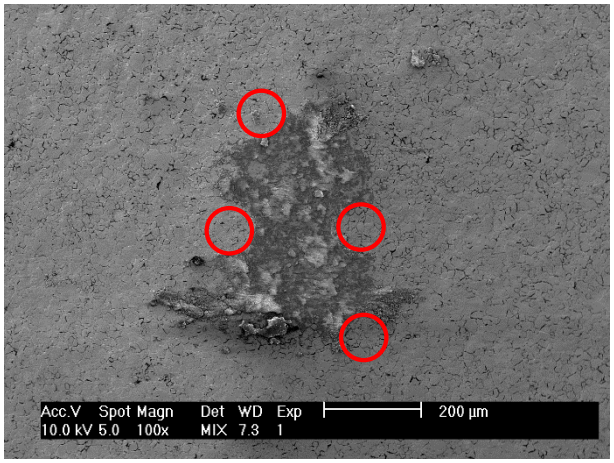

Figure 66 – Sphere counterpart of the denser inverted test (depressions open contacts).

4.4. BATTERIES CHARACTERIZATION

The supplied battery specimens, although being different models of two distinct manufacturers, do not differ too much as far as materials and friction behaviour goes, as it is shown in the following section and in the component presentation.

4.4.1. Friction characterization

Coefficient of friction is often a very good indicator of friction controlled processes and in the situation of intermittent operation of wear processes a classic approach is necessary to determine both static and dynamic coefficient responses. The following values were determined resorting to reciprocating tests for dynamic friction (Esteves *et al.*, 2013) and an inclined plane test for static friction.

Table 26, which comprises the interaction of both positive and negative poles, is proof of a typical similarity and subsequent response between this types of components. Even between positive and negative pole surfaces of the same specimen the results are very close to each other regarding static coefficient of friction. For dynamic friction, after the removal of the texture or running-in, the coefficient is dominated by the steel response.

Table 26 – Friction coefficient for the battery specimens.

Battery		Static	Dynamic		
		μF	μF_{min} (total)	μF (average)	μF_{max} (running-in)
Specimen 1	**(-) pole**	0.39±0.03	0.47	0.55	0.99
	(+) pole	0.22±0.03	0.12	0.80	1.04
Specimen 2	**(-) pole**	0.22±0.04	0.64	0.77	0.86
	(+) pole	0.23±0.03	0.11	0.78	1.01

The wear results of the reciprocating tests on the battery specimens, shown in Figure 67, denote a clear tendency or disparity in the wear volumes of both specimens. This should be linked to the native difference of material hardness and nickel platting thickness, analysed on the chapter 3.

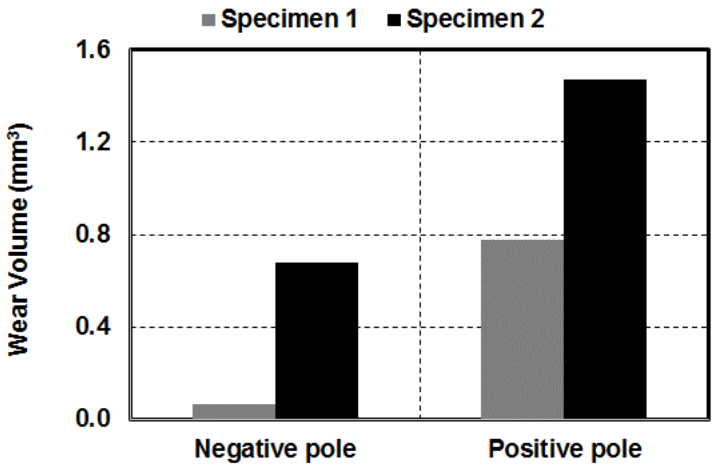

Figure 67 – Wear volume of reciprocating tests on battery specimens.

4.4.2. Specimen 2 fretting characterization

The fretting tests on the battery contacts were performed after the fretting study without electric current, making the discussion lighter and reducing the amount of unknown effects.

Displacement variation, Figure 68, is clear in demonstrating an almost linear relationship on both specimens, similar to the 304 stainless steel behaviour represented by the dashed lines in each graph.

Very important to point out is that these tests were performed on the negative pole contact (textured) as is the most solicited side. The wear volume is clearly higher when compared with the results of the uncoated 304 stainless steel, indicating a lower wear resistance from the nickel platting as coefficient of friction is very similar, with a cumulative wear effect from the sphere, and the inability to activate or take advantage of the textured surface.

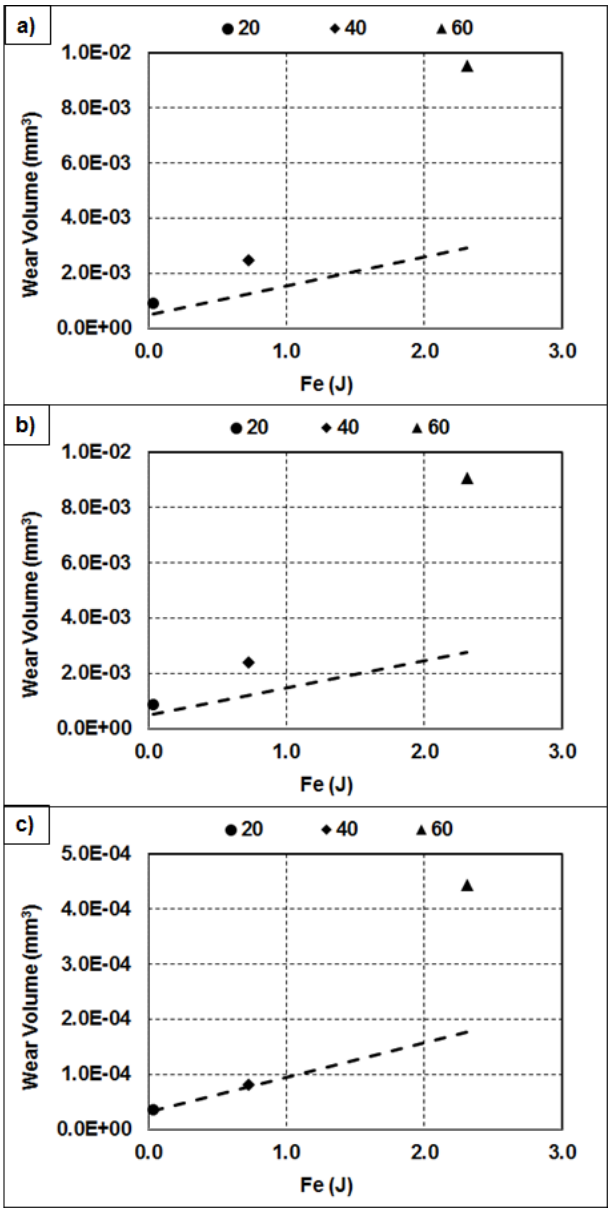

Figure 68 - Energy dissipated by friction versus wear volume for displacement variation on specimen 2 (dashed line represents the wear rate for the 304 stainless steel results), a) - total wear volume; b) – sphere wear volume; c) – battery wear volume.

Nickel platting effect on the relative humidity variation is clear on Figure 69. As the relative humidity is highly responsible for governing oxidation on steel, due to an inert nature of the coating and proximity of the wear volume values the result is two different wear tendencies.

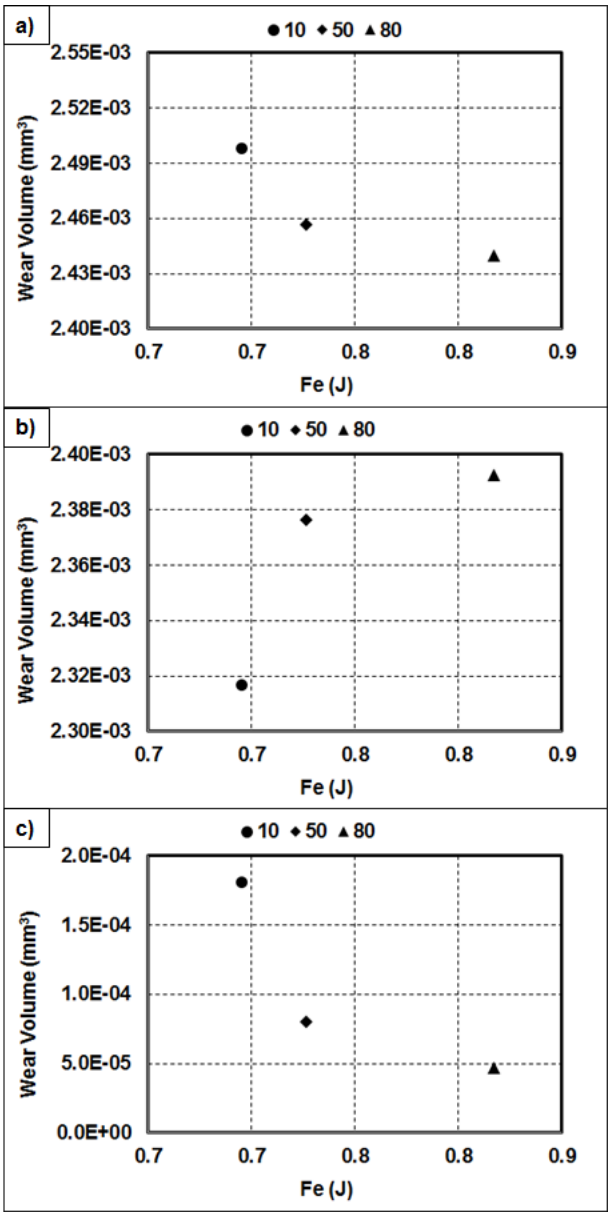

Figure 69 - Energy dissipated by friction versus wear volume for humidity variation on specimen 2, a) - total wear volume; b) – sphere wear volume; c) – battery wear volume.

An inert atmosphere, when introduced on the contact pair, reduces significantly wear and oxidation, Figure 70, evident on the stainless steel sphere, contrary to an oxygen rich environment. On the battery specimen the effect of nitrogen environment is not significant but the oxygen one had the opposite influence, believed to be an abrasive action performed by the oxidised wear debris.

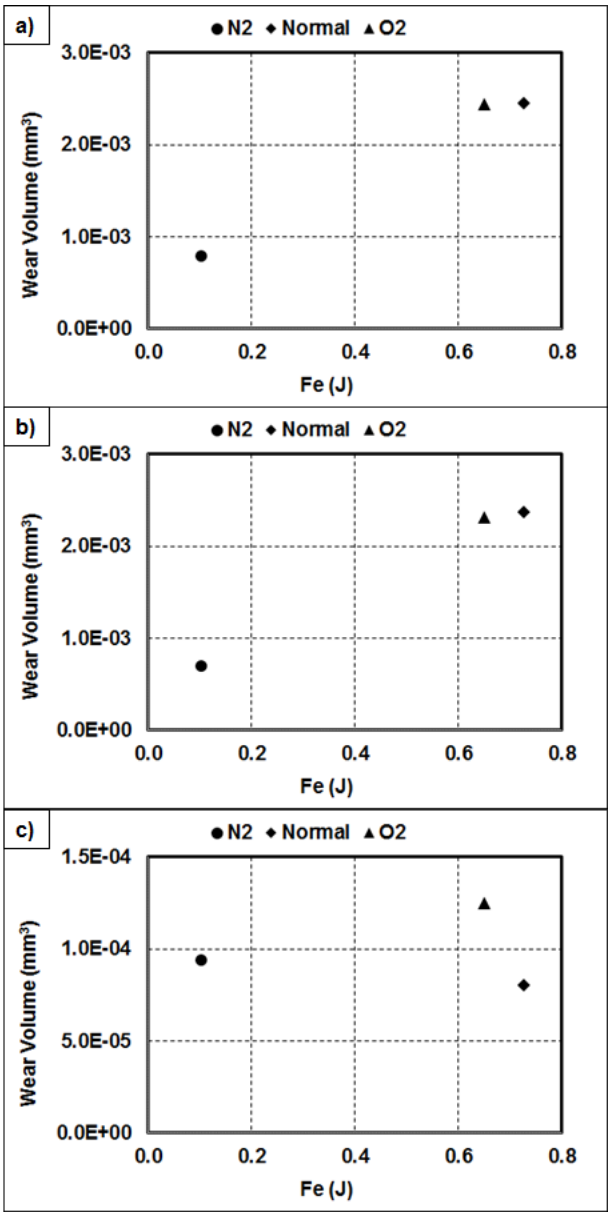

Figure 70 - Energy dissipated by friction versus wear volume for atmosphere variation on specimen 2, a) - total wear volume; b) – sphere wear volume; c) – battery wear volume.

The friction response to environment variation is expected since it is reduced for higher relative humidity values and higher for the inert atmosphere, Table 27, both on the account of oxidation phenomenon.

Table 27 – Friction coefficient for fretting tests of specimen 2.

Displacement variation (µm)	**20**	**40**	**60**
	0.14	0.24	0.30
Humidity variation (% RH)	**10**	**50**	**80**
	0.30	0.24	0.22
Atmosphere variation	**Nitrogen**	**Normal**	**Oxygen**
	0.36	0.24	0.25

What we concluded by this characterization is the role of nickel platting on the environmental wear response. From this point on, two main concerns arose in the subsequent of this work. One was the influence of nickel platting on the fretting process itself and the difficulty to pinpoint it's effect and the other was the battery texture effect , in fact much more interesting to develop than the coating response due to availability of information and scientific work in the field.

Therefore, the evolution of the present work took form considering similar independent materials allowing a clarified vision on fretting effects.

4.5. PCB CHARACTERIZATION

4.5.1. Scratch tests

Figure 71 shows an illustration of; normal load, friction force and friction coefficient evolution of a scratch test. The flat surface acts as a very ductile material, with low coefficient of friction until the nickel plating is removed. After the nickel plating is reached the peak friction coefficient stabilizes at 0.63.

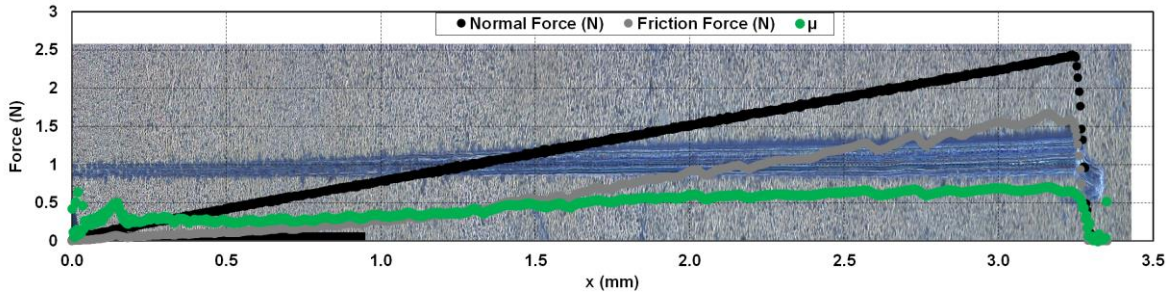

Figure 71 – PCB scratch test with friction representation.

The surface/contact material presented very high ductility, Figure 72, and it deformed plastically with no spalling.

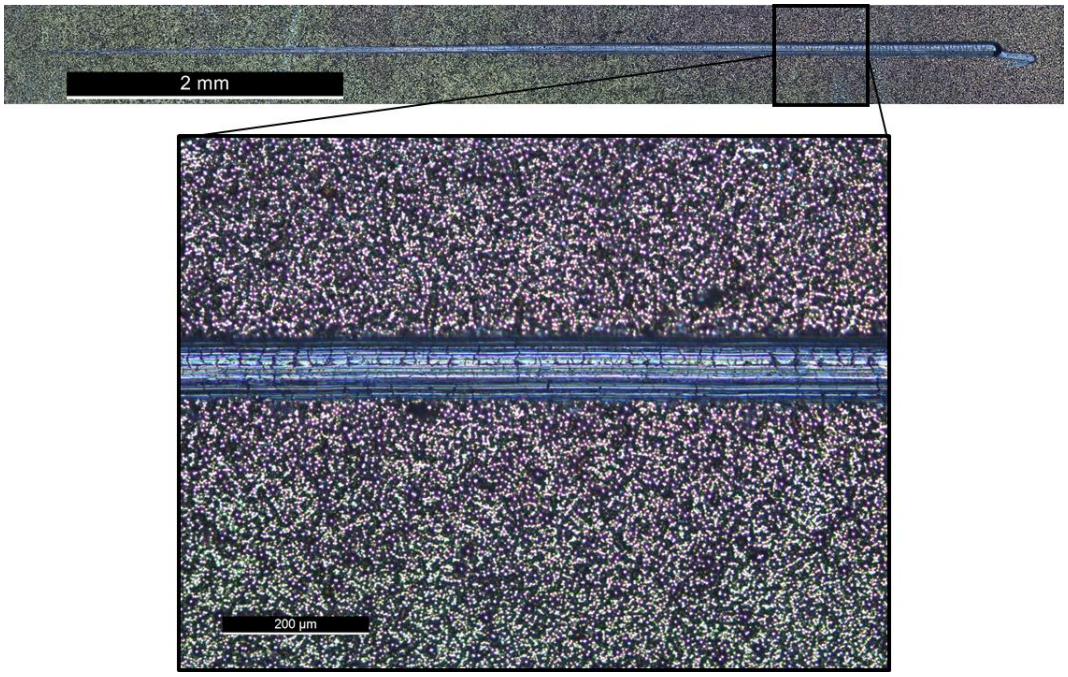

Figure 72 - PCB scratch morphology detail.

4.5.2. PCB fretting characterization

As stated in the procedure section, the characterization of the industrial components started early on this work however the applicability of the methods and material analysis was not satisfactory to a full understanding of the process variables.

Fretting wear tests clearly demonstrated the gold coating behaviour and the displacement study, Figure 73, is clear on that matter. The 10 µm test didn't applied significant wear since the contact was in partial slip the entire test but the 20 µm test almost completely removed the gold coating.

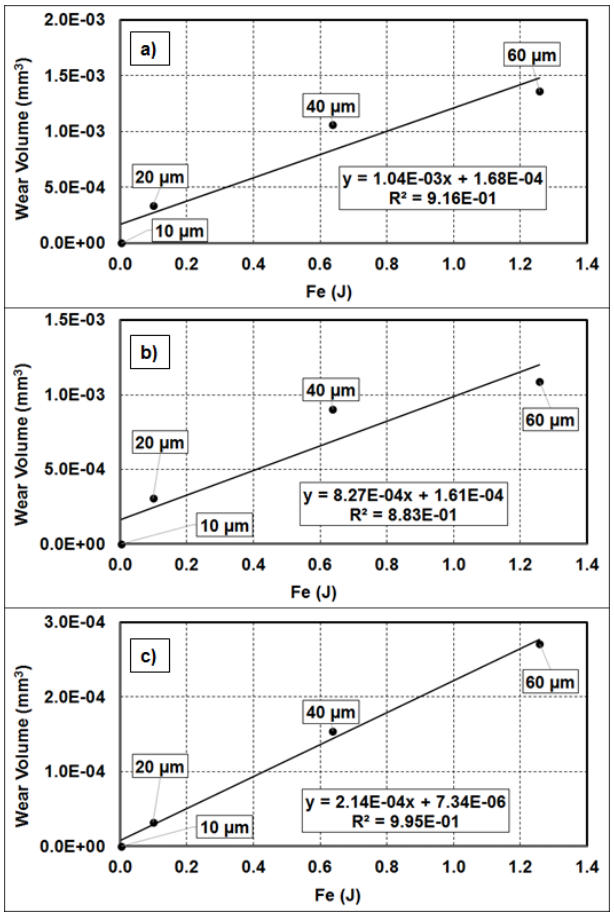

Figure 73 - Energy dissipated by friction versus wear volume for displacement variation, a) - total wear volume; b) – sphere wear volume; c) – PCB wear volume.

For an intermediate displacement condition, 40 µm imposed displacement, the number of cycles to completely remove the gold platting is very low, just 1,000 cycles, and since its effects on wear resistance are insignificant, Figure 74, the wear rates and tendency are almost unchanged for the entire study.

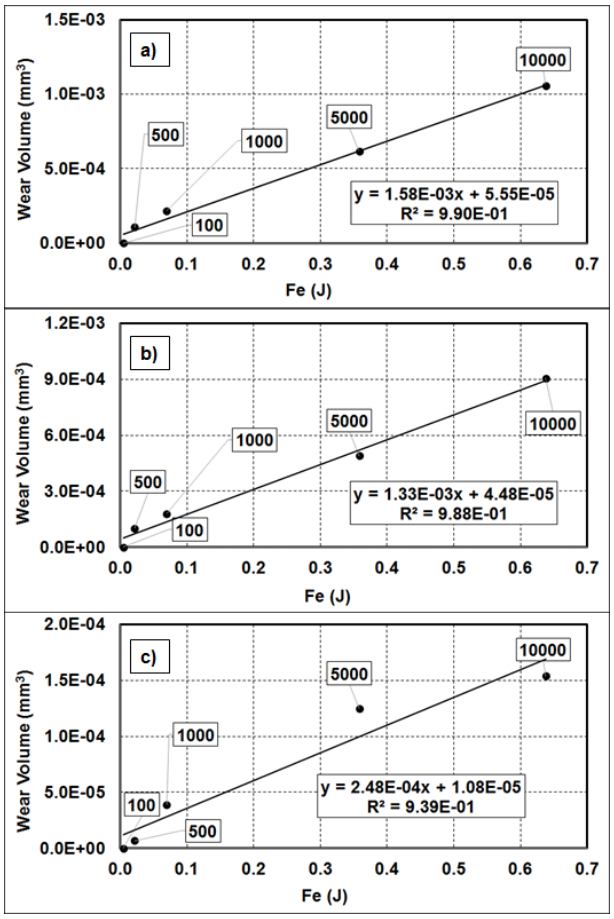

Figure 74 - Energy dissipated by friction versus wear volume for number of cycles variation, a) - total wear volume; b) – sphere wear volume; c) – PCB wear volume.

Sphere diameter variation present in Figure 75, which derived from a necessity to evaluate the contact behaviour on different wear regimes due to low wear resistance and the inability to alter the load applied by contact springs, didn't establish a clear performance. In every test, the gold coating was removed and for the smallest diameter, 3.1 mm, the copper substrate was reached, mainly because the contact pressure was too high. With larger spherical contacts, the gold coating should stand the wear process longer however the entire volume removed would still be great by means of a bigger contact area.

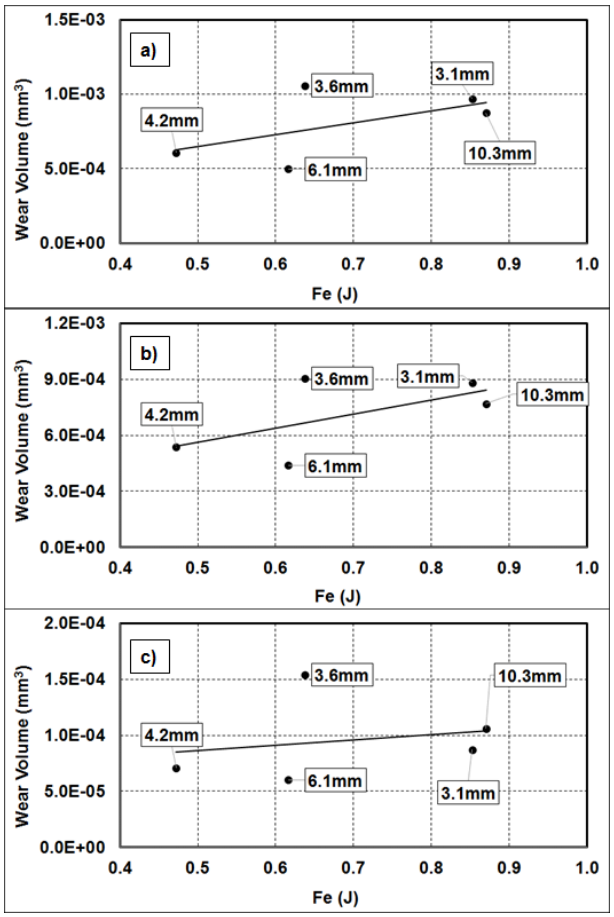

Figure 75 - Energy dissipated by friction versus wear volume for sphere diameter variation, a) - total wear volume; b) – sphere wear volume; c) – PCB wear volume.

Further development of this analysis was held up primarily for two reasons. The first was due to the inadequacy of the contact to a fretting wear environment, gold coating essentially. The second was the indication of the company intention to change the type of contact.

5. WEAR PREDICTION MODEL

After the initial approach taken in this study, specifically referring to the case studies, a wear model started to take shape with a sole purpose to quantify or predict wear on these specific contacts. This model was created specifically to ball on flat contact applications.

A Hertzian normal contact pressure and a friction stress field are used to determine the resulting contact stresses leading to local analysis of the wear process. The quantification and matching wear amount can be established using a model based on the energy dissipated by friction or alternatively a model based on the normal pressure.

An experimental validation study was done, based on two pairs of materials commonly used in mechanical applications, which will subsequently be presented. The resulting wear is compared considering both the local wear depth and the wear volume of experimental tests with the forecasted values.

5.1. WEAR MODEL INTRODUCTION

The model is built in a low-level programming language, MATLAB, for very specific reasons. The most important is the ease of programming in this platform, but also the set of tools available is in good accordance with the aim of the work.

Fundamentally, there is an iterative process running for each fretting cycle that determines the stress field of a specific contact pair, consequent local energy dissipated and the increment of material removal. A general flowchart of the model process is presented in Figure 76, where two wear conditions are differentiated, reciprocating sliding and fretting, these being the contact dynamics and discretization of the main differences between the two.

The two-body contact plane is transposed to a 2D matrix, in the *x* and *y* axes, with a specific discretization, displayed respectively in each model section.

The stress field is determined in the matrix nodes, subsequent dissipated energy and removed material, enabling a localized analysis.

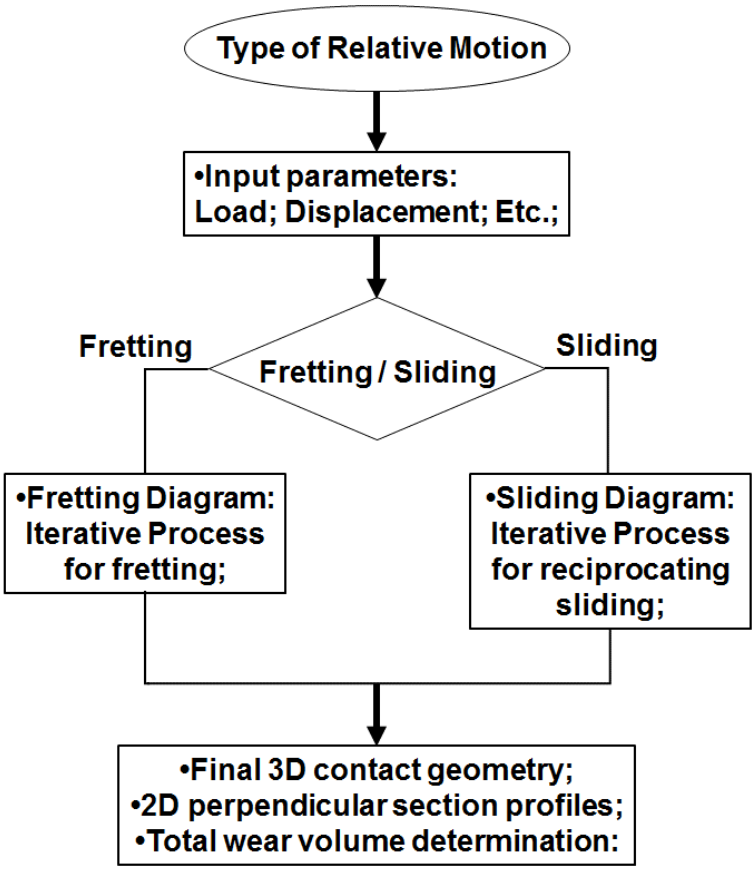

Figure 76 - Model overall flowchart.

The resulting stress field distribution on the contact should be determined taking into account the equivalent Hertzian stress and friction stress field, considering the stress field equation of the theory of elasticity (Hamilton *et al.*, 1966; Hamilton *et al.*, 1983; Mindlin, 1949), present in annex A.

The friction energy dissipated in the contact is the equivalent work *per* unit area produced by surface stresses applied in the same direction as the imposed movement because *X* is the direction of the relative motion, therefore, tangential stresses on the *ZX* defined plane (τ_{zx}). This translates as the friction force, which is the only force component producing work in the contact during the relative motion.

Thus, in every wear condition or model variation the two core difficulties to overcome are determining the stress field, with the consequent dissipated energy and wear, and the contact geometry variation. The way the model treats the interaction as always approximated to a geometric contact allows the application of the elastic theory explicit equations, in (Hamilton *et al.*, 1983), combined with energetic wear models, advocated by

(Fouvry *et al.*, 2003), and applied locally on single elementary sections. The contact dimension demanded an empirical approach for the increased contact size without the need for intricate finite modelling analysis. A detailed description is presented in the next sections, together with specific distinctions.

5.2. RECIPROCATING SLIDING

5.2.1. Model principles

Reciprocating motion is the basis of the main classic mechanisms whish are very currently used in most of engineering creations. Therefore, reciprocating sliding is usually applied in wear performance studies, allowing a great input of wear (material removal) and consequently significant geometry variation. With the addition of previous experimental knowledge, it was defined that the current model would run for two distinct contact geometries, the initial one, sphere/half-space maintained until a limit condition is achieved, and a secondary one, sphere/cylindrical race for the remaining duration of the test. Generally, the initial condition runs only for a few cycles due to immediate geometrical variations, but the threshold is frequently dependent on the contact pair.

Figure 77 represents the evolution of the reciprocating simulation from the contact definition to the final solution. After the initial necessary parameters are inputted in the model, the stress field is calculated on an *XY* matrix for the contact plane. This matrix is bound to the referred plane and only the contacted region are transferred according to the displacement. From that point, a frictional energy is determined as well as consequent localized wear and contact update until a limit condition is reached. This condition can represent a geometrical, volume or cycle number parameter, depending always on the user definitions. Overall, these parameters can control coating limits, minimum/maximum wear depth or of sliding distance. When the specified limit is achieved, the contact geometry is altered to the secondary one, and the calculation process is repeated until the end of the test. Only when each test is completed are the output variables calculated and presented.

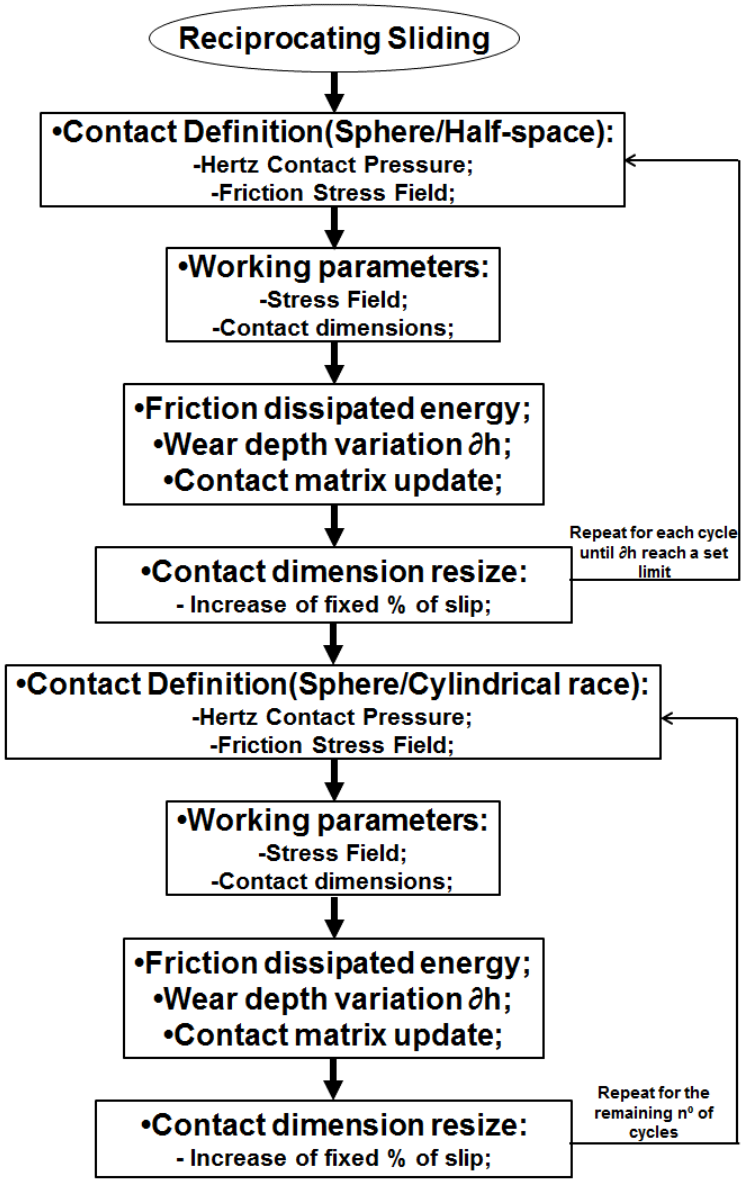

Figure 77 – Reciprocating sliding model section flowchart.

The output parameters are determined and updated for each cycle but only presented at the end of each simulation. The friction-dissipated energy is equivalent to the work executed by the friction force or the equivalent stresses by section area, as in equation (13).

$$F_e = \tau \times dA \times dX \tag{13}$$

A general energetic model is used to determine the wear locally, equation (14), based on a wear rate and the work done by friction.

$$V = K_E \times F \times X \tag{14}$$

The depth variation is determined for a specific section (elemental area on the contact plane), given in equation (15), where, by means of the shear stress present on that plane, the friction dictates the majority of the energy dissipated in the contact, as shown in equation (16).

$$dh \times dA = K_E \times dF \times dX \tag{15}$$

$$dh = K_E \times \left(\frac{dF}{dA}\right) \times dX = K_E \times \tau \times dX \tag{16}$$

The depth is a variation only in the *Z* axis forming the wear scar, but it is also a limit condition for contact geometry iteration. This process isolates local depth variations of the elementary sections considered, thus gradually building a 3D volume matrix.

Throughout the simulation, the contact should vary continually, but in order to quantify the shear stresses involved without the need of a FEM analysis, which is the only way possible to analyse a complex geometry stress distribution, it was established that said contact geometries can be considered as the most similar simplified cases.

5.2.2. Simulation variables

The discretization for the reciprocating sliding model, used on the scope of the present study, is shown in Table 28. A squared element with 10 µm length proved to be enough to maintain a performance/correlation quotient. A smaller element will not improve the model accuracy, but greatly increases the processing time.

Table 28 – Reciprocating sliding contact matrix.

Matrix Elements (XY)	400×400
Matrix area (mm^2)	4×4
Element size (μm^2)	10×10

The remaining input tests parameters are specified in Table 29, for the validation tests. In this current state, the model can work with generic average friction coefficient and wear rates. Only for validation purposes is it necessary to use the experimentally obtained values.

Table 29 – Reciprocating sliding input variables.

	Sphere	**Flat Specimen**
E (GPa)	393	210
υ	0.27	0.3
Initial radius (mm)	5	∞
Normal Load (N)	7;10;15	
Duration (cycles)	5000; 10000; 20000	
Stroke (mm)	2	
COF	0.771	
K (mm^3/J)	2.04×10^{-5}	

5.3. FRETTING

5.3.1. Model principles

Fretting wear is normally associated with very small relative displacements between mated surfaces, in the order of micrometres, usually subjected to high frequency solicitations. In fact, the contact is never fully renovated since the slip should never surpass the real contact dimension. The contact geometry is the same as that used initially in the reciprocating sliding, i.e. sphere/half-space, due to the nature of the close contact and low wear. The general evolution is shown in Figure 78 and it follows the reciprocating procedure until the second step when, after the assembly of the contact plane *XY* matrix, the fretting regime dictates the wear process evolution, for each cycle.

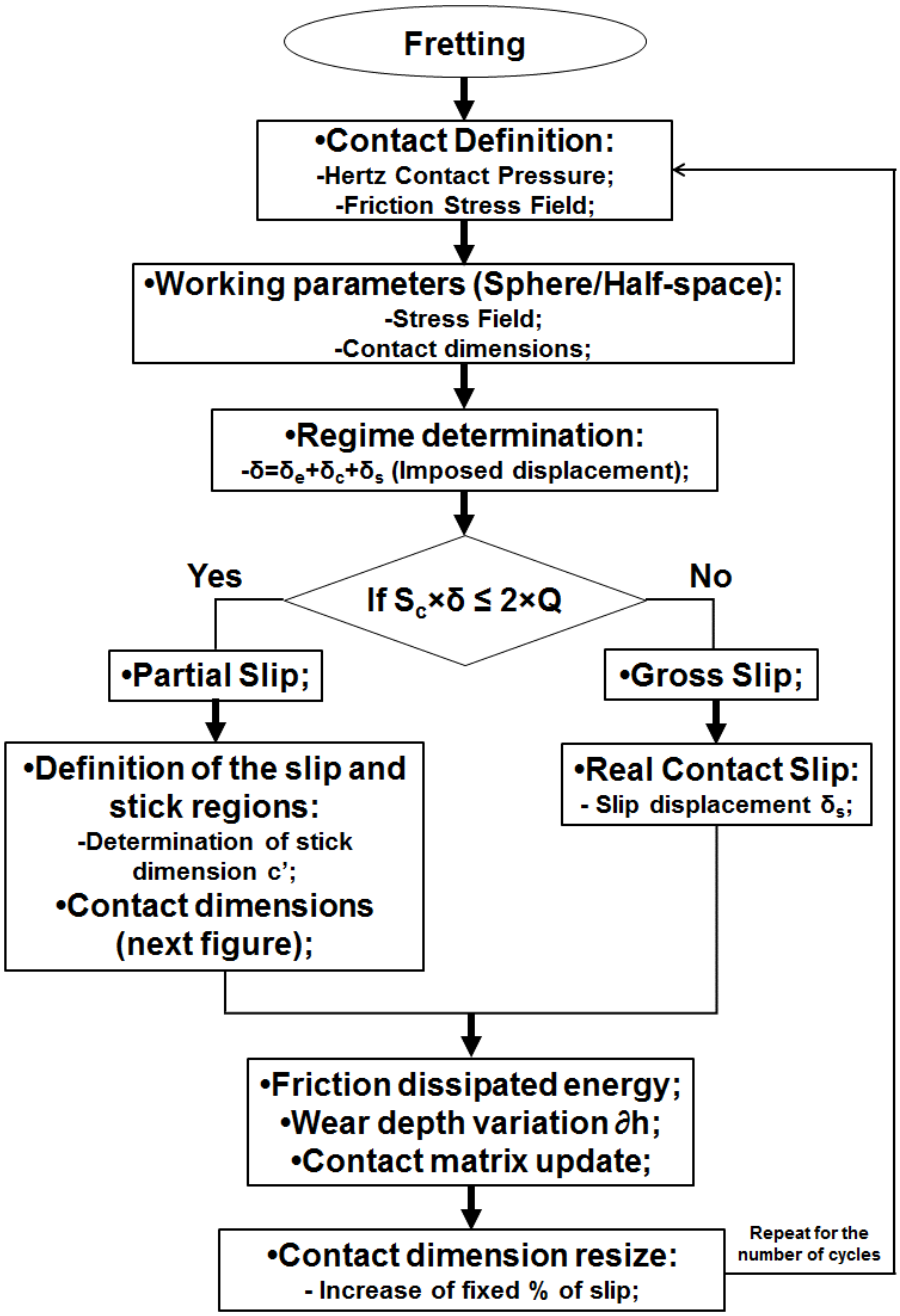

Figure 78 – Fretting model section flowchart.

Currently, the model considers the two main fretting regimes, partial slip and gross slip, and due to system rigidity the imposed displacement can input null slip. The regime variation is controlled by displacement where, for the imposed displacement, δ, and a system rigidity, S_c, if the total tangential load, $2\times Q$, is higher than the product of system rigidity and imposed displacement, the contact is in partial slip; otherwise, the regime is gross slip.

In the case of partial slip, it is necessary to determine the adhesion zone of the contact variation in every instant. Therefore, the value of the stick zone for maximum tangential load, point *A* of Figure 79 and Figure 80, represented as c_0, resorting to equation (17).

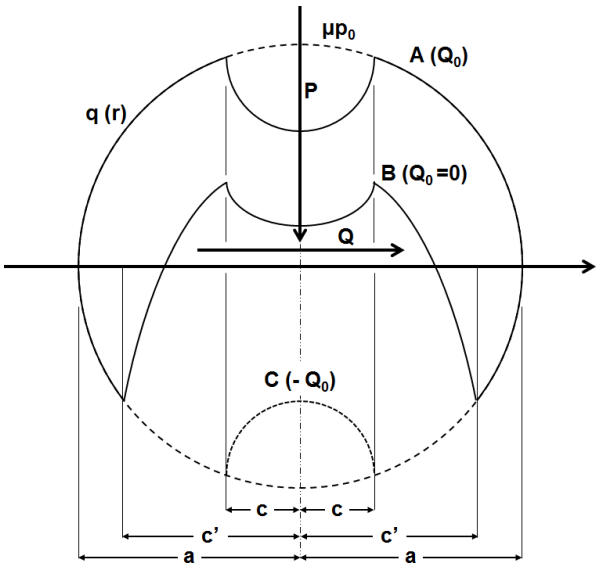

Figure 79 – Circular contact subjected to a steady normal load P and an oscillating tangential load of amplitude Q.

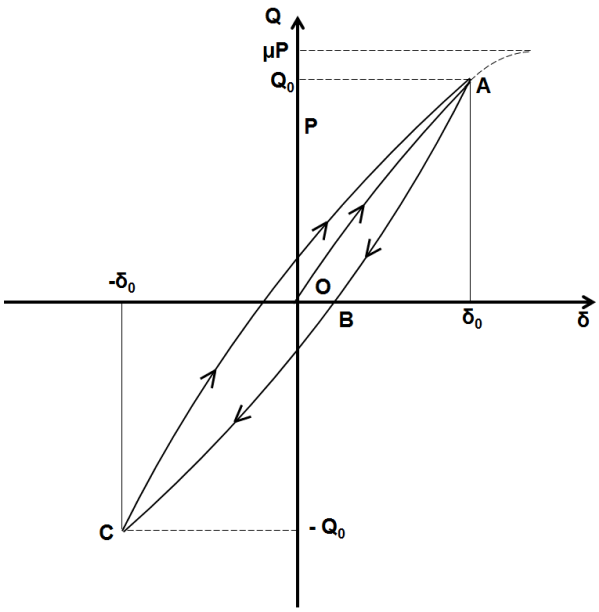

Figure 80 – Partial slip load displacement cycle.

$$Q_0/\mu P_0 = 1 - (c_0{}^3/a^3) \qquad (17)$$

The instantaneous value of the stick contact, *c'*, is determined in an iterative process with the slip displacement until *c'* reaches the limit of the contact, equal to, equation (18).

$$\delta = \delta^* - \Delta\delta = \left(\frac{3\mu P_0}{16a^3}\right) \times \left(\left(2 - \frac{\upsilon_1}{G_1}\right) + \left(2 - \frac{\upsilon_2}{G_2}\right)\right) \times \left((a^2 - {c_0}^2) - 2\left(a^2 - {c'}^2\right)\right) \quad (18)$$

A gross slip scenario considers a full slip of the entire contact, but even so, the imposed displacement is always affected by the system rigidity, which is nothing more than the elastic accommodation of the system, resulting in a smaller slip displacement. This limit is also governed by the tangential load, friction force, up to the limit of the rigidity, as represented in equation (19).

$$\delta_s = \delta - \left(\frac{2Q}{S_c}\right) \quad (19)$$

As for the reciprocating sliding model, the output parameters are determined and updated for each cycle but only presented at the end of each simulation, according to equations (13) to (16).

5.3.2. Simulation Variables

The discretization applied for the fretting model is shown in Table 30. A squared element with 0.1 µm length proved to be enough to maintain an adequate performance/correlation quotient. A smaller element will not improve the model accuracy but greatly increases the processing time, even though this is a relevant subject since this is a fast prediction model.

Table 30 – Fretting contact matrix.

Matrix Elements (XY)	3000×3000
Matrix area (μm^2)	300×300
Element size (μm^2)	0.1×0.1

The remaining input tests parameters are specified in Table 31, for the validation tests. In this current state, the model can work with generic average coefficient of friction and wear rates. Only for validation purposes is it necessary to use the experimentally obtained values.

Table 31 – Fretting input variables.

	Sphere	**Flat Specimen**
E (GPa)	210	210
υ	0.3	0.3
Initial radius (mm)	5	∞
Normal Load (N)	20	
Duration (cycles)	10000	
Displacement (μm)	20;40;50;60	
COF	0.05;0.23;0.26;0.24;0.22;0.21	
K (mm^3/J)	2.06×10^{-5}	

5.4. MATERIALS AND EXPERIMENTAL PROCEDURES

5.4.1. Materials and specimens

For the purpose of developing and improving the model performance, a set of dedicated tests and materials were used to better understand the limitations and state evolution. After the model reached a mature state, it was applied to some previous universal work in order to fundament a wider application.

5.4.1.1. Reciprocating fretting validation

The materials used in this study were an AISI M2 steel, with E = 210 GPa and υ = 0.3, for the flat specimens and a commercial bearing steel ball, AISI 52100 with E = 210 GPa and υ = 0.3.

Every flat specimen was polished in a routine beginning with sandpapering and completed with the use of a 3 μm diamond finishing suspension in order to ensure a uniform and even contact surface through all the samples. The contact pair was selected regarding a low probability of adhesion occurrence, as well as the elastic behaviour of both specimens under these loading conditions.

5.4.1.2. Reciprocating sliding validation

The selected specimens to the reciprocating sliding study were alumina balls, with E = 393 GPa and υ = 0.3, and an AISI M2 steel, with E = 210 GPa and υ = 0.27, for the flat specimen also polished with the previous mentioned procedure. The selected contact pair was used to minimise adhesion contribution to the wear process but also the introduction of two different materials of dissimilar mechanical properties.

5.4.1.3. Reciprocating fretting retroactive validation

The specimens used were all made from AISI 304 (I) stainless steel, with E = 210 GPa and υ = 0.3. This is a previous published work regarding the influence of different environmental conditions (Esteves *et al.*, 2015), also part of this manuscript described in the atmosphere study.

5.4.1.4. Reciprocating Sliding retroactive validation

The materials were a grey cast iron GJL 200, DIN EN 1561 with E = 101 GPa and υ = 0.26, for the flat specimens and a commercial ball bearing steel AISI 52100, with E = 210 GPa and υ = 0.3, used on a previous study (Miranda *et al.*, 2014).

5.4.2. Experimental procedures

Besides the specific model validation sections, a previous universal work was also compared against model results. Since the experimental procedure is similar between same wear tests, the parameters for the retroactive application are stated on the validation and discussion section.

5.4.2.1. Reciprocating sliding

The experimental procedure of reciprocating sliding ball-on-flat wear tests was performed to determine the wear behaviour of the M2 steel as well as the wear produced on the alumina ball. This technique comprises a sliding contact of a spherical body (10 mm radius) in reciprocating motion against a M2 steel stationary flat specimen, shown in detail in (Antunes *et al.*, 2014). In the scope of the present study, the test conditions are presented in Table 32.

Table 32 - Reciprocating sliding tests conditions.

Normal Load (N)	Cycles	Frequency (Hz)	Stroke (mm)
10	5,000	1	2
7;10;15	10,000		
10	20,000		

After the tests, the produced scars on the flat specimen were scanned with 3D profilometry. The spherical specimens presented wear scars with spherical-cap shape and the diameter of their surface was measured in two orthogonal directions: the direction of motion and the direction perpendicular to it. Wear classification was based on friction dissipated energy and the localized volume variation (contact geometries) were analysed by 2D local profiles.

5.4.2.2. Reciprocating fretting

The tribometer used, described in detail in (Esteves *et al.*, 2015), imposes a unidirectional reciprocating movement (tangential fretting) induced by a piezoelectric actuator.

The experimental conditions are presented in Table 33 and the procedure is identical to the one presented in (Esteves *et al.*, 2015).

Table 33 - Reciprocating fretting tests conditions.

Normal Load (N)	Imposed Displacement (µm)	Frequency (Hz)	Nº Cycles
20	20	10	10,000
	40		
	50		
	60		

Wear classification was based on friction dissipated energy. The localized volume variation (contact geometries) were analysed by 2D local profiles.

5.5. VALIDATION AND DISCUSSION

As initially proposed, both wear models derivations are evaluated by three standards: friction-dissipated energy, local and total wear volume. In an early stage of model

development, the energy correlation was a critical parameter in determining the suitability of the basic principles. Following the acceptance of this approach, both the global and localized wear performances are evaluated, and the two final model versions are a compromise between these two standards.

5.5.1. Reciprocating sliding

This section features reciprocating sliding validation test materials, an alumina sphere and an AISI M2 flat specimen. On both wear model approximations, only the tangential load variation is necessary. The initial shear contact stresses are represented as dimensionless to the contact size in Figure 81. There is significant increase of the τ_{zx} stresses towards the contact centre, intended for the present wear process.

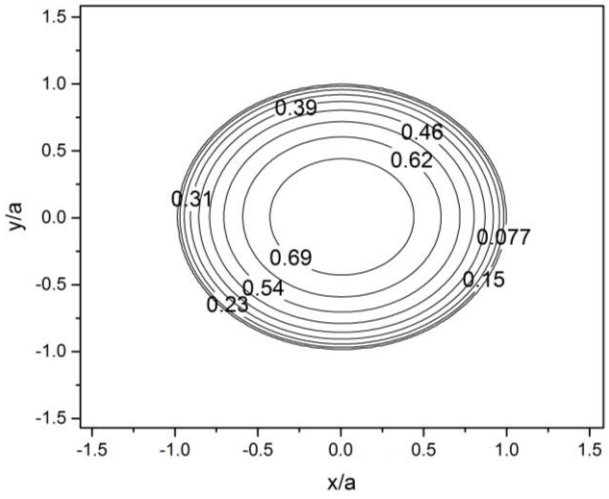

Figure 81 – Isolines for τ_{zx}/p_0 on the surface (Z=0) for the reciprocating sliding (μ=0.771).

In order to determine the suitability of the approach, the basic principles were to be tested first, namely the energy dissipated by friction correlation between the model and experiment. Table 34 shows the energy dissipated by friction during all of the tests, modelled and experimental, and a good approximation was found by the method in use.

Table 34 - Reciprocating sliding friction dissipated energy correlation.

Load (N)/Nº Cycles	Test	Friction dissipated energy (J)				
		7	10			15
		10,000	5,000	10,000	20,000	10,000
Experimental		250.12	168.10	338.61	668.57	454.81
Model		228.93	162.35	323.64	646.14	487.39
Relative error (%)		-8%	-3%	-4%	-3%	7%

There is a noticeable difference in the evolution of relative error due to the use of an average coefficient of friction rather than the specific value for each test. Nonetheless, all the results show less than 10% of error, which should be acceptable for this form of study.

The experimental results, displayed in Figure 82, show linear wear trends on both specimens although with dissimilar wear rates. Due to geometrical restrictions, the localized wear variation of the ball will not be evaluated and therefore only for the flat specimens are the wear scar dimensions modelled.

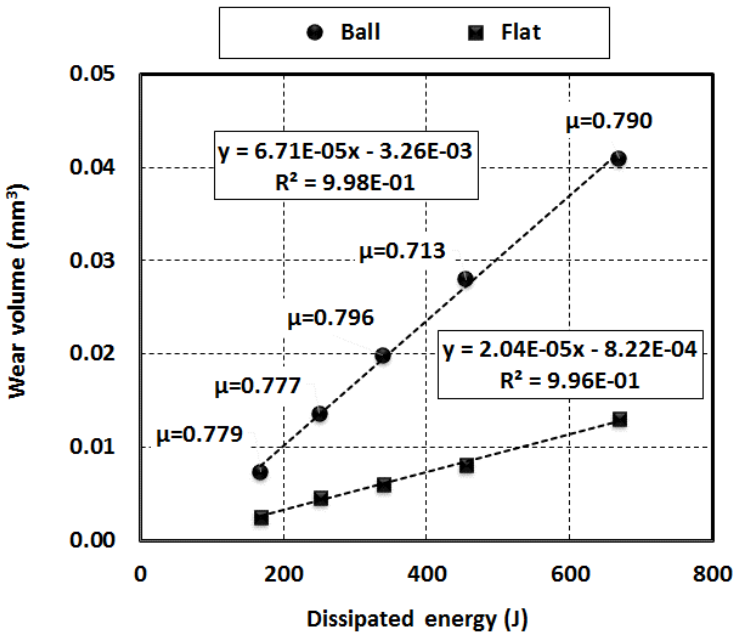

Figure 82 – Friction dissipated energy versus wear volume for the experimental reciprocating sliding tests.

Experimental results on both specimens present very good linear tendencies, one of the main aspects since the model uses a constant wear coefficient throughout the simulation.

Also, one of the material selection conditions was this linearity and the low adhesion between a contact pair.

The mean value and standard deviation were obtained by a linearization model described in (Ramalho, 2010), were the wear rate mean and standard deviation for the flat specimens are $k = 2.04 \times 10^{-5} \pm 7.73 \times 10^{-7}$ and for the spherical specimens are $k = 6.71 \times 10^{-5} \pm 1.83 \times 10^{-6}$. Both STD (standard deviation) values are at least one order of magnitude lower than the wear rates.

Wear obtained after performing the experimental tests was measured and then compared against the model results, regarding the total wear volume. Every test that underwent this process is represented in Table 35.

Table 35 - Reciprocating sliding wear correlation.

Load (N)/Nº Cycles	**Test**	**Wear volume (mm^3)**				
		7	10			15
		10000	5000	10000	20000	10000
Flat	**Experimental**	$4.60x10^{-3}$	$2.55x10^{-3}$	$6.00x10^{-3}$	$1.30x10^{-2}$	$8.10x10^{-3}$
	Model	$3.69x10^{-3}$	$2.40x10^{-3}$	$5.63x10^{-3}$	$1.21x10^{-2}$	$8.85x10^{-3}$
	Relative error (%)	-20%	-6%	-6%	-7%	9%
Ball	**Experimental**	$1.36x10^{-2}$	$7.35x10^{-3}$	$1.99x10^{-2}$	$4.10x10^{-2}$	$2.80x10^{-2}$
	Model	$1.16x10^{-2}$	$6.73x10^{-3}$	$1.68x10^{-2}$	$3.92x10^{-2}$	$2.67x10^{-2}$
	Relative error (%)	-15%	-8%	-15%	-4%	-5%

The total wear volume presents a very good correlation between the experimental and modelled values, although with the low severity, 7N test, there is a slight variation. This is most likely due to the irregularity of the wear scar along with the difference in friction-dissipated energy.

Figure 83 displays 3D images of the characteristic wear scar of both model and experimental results. The analysis of model performance can be achieved by comparing the two space representations as well as the total wear volume, although localized variations are better expressed with 2D section profiles.

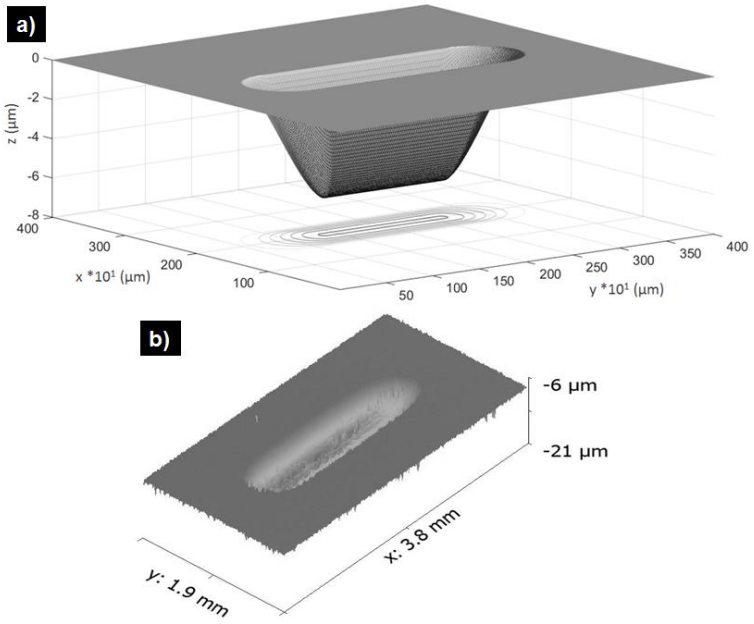

Figure 83 – Reciprocating sliding: a) model 3D representation and b) experimental 3D representation for 10N and 10,000 cycles.

As seen from Figure 84, presenting the 2D intermediate sections of both the model and experimental wear scars, the predictions are approximate to the real results. This relates fairly well on the depth and width of the scars. Note that these are intermediate sections for the purpose of maximum depth, length and width comparisons, but the borders as well as the scar morphology present some dissimilarities, as can be seen in the results.

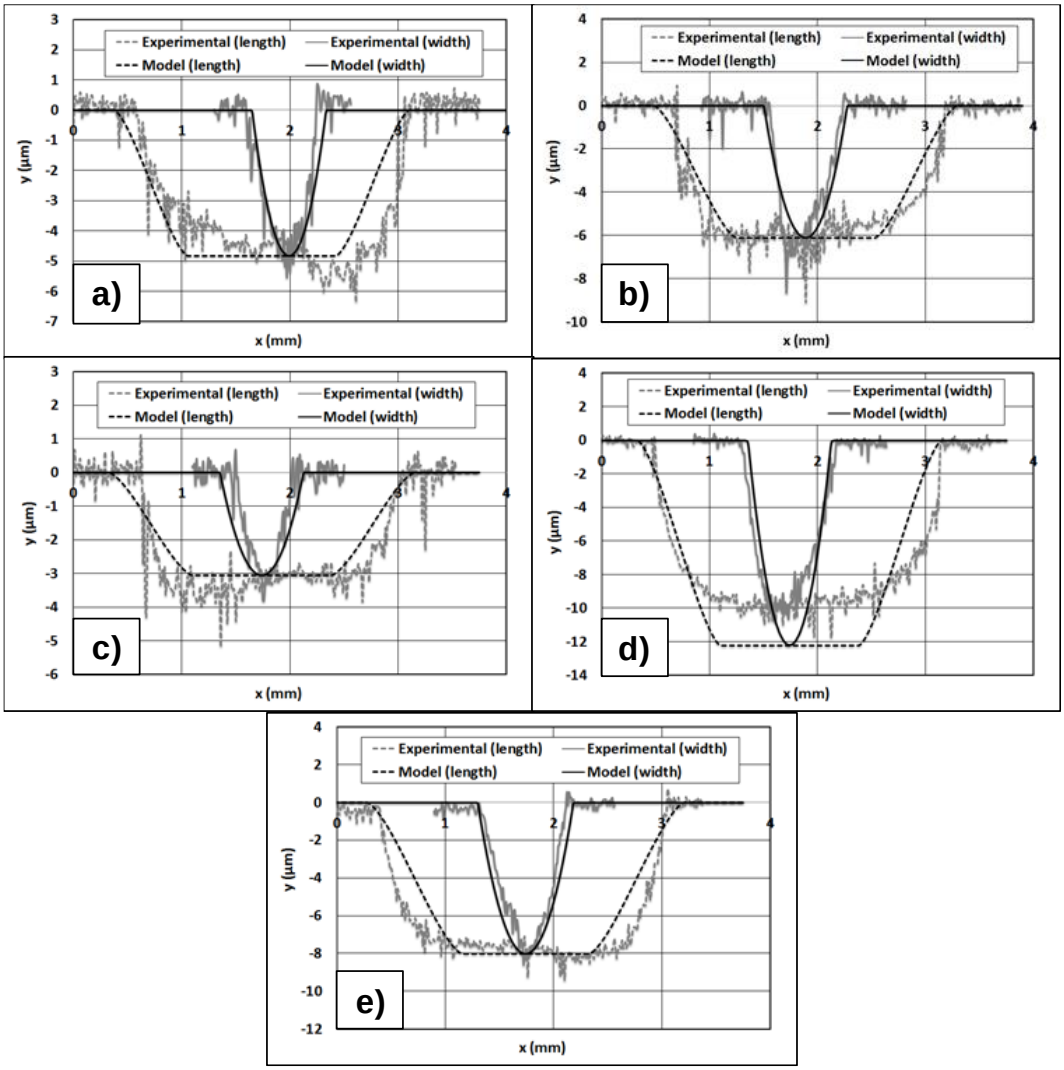

Figure 84 - Reciprocating sliding section comparison for: a) – 7N and 10000 cycles; b) – 10N and 10000 cycles; c) – 10N and 5000 cycles; d) – 20N and 20000 cycles; e) – 15N and 10000 cycles.

A more symmetrical experimental wear scar increases the correlation of the results, since the model only relies on geometrical relations to determine wear. This is evident in Figure 84 – a) and d).

The most interesting aspect, as it is the main purpose of the study, is the ability to define the general limits of the wear scar, but since the contact variation relies on an algorithm which dependents on the growth of the wear scar, specifically the depth, there can be a slight progress divergence as seen in Figure 84 – d), for the longest test performed. It is also important to mention that the said algorithm is common to every test and can be altered to include a sliding distance dependence that is not relevant in the present study.

Regarding the overall performance of the model, there are two main aspects that can affect the result. One is the of the steady state regime, or lack of it, leading to an irregular wear mark as shown in Figure 84 – a) for the lowest severity test. The other is the variation of the contacting body's geometry and subsequent contact (area, tension distribution, etc.), which are strongly dependent on wear evolution.

5.5.2. Reciprocating sliding retroactive application

The discretization applied is identical to the validation approach and all of the input tests parameters are specified in Table 36.

Table 36 – Reciprocating sliding input variables (retroactive application).

	Sphere AISI 52100	**Flat Specimen GJL 200**
E (GPa)	210	101
υ	0.3	0.26
Initial radius (mm)	5	∞
Normal Load (N)	10	
Duration (cycles)	5,000; 6,600; 8,500; 10,000;	
Stroke (mm)	2	
COF	0.428	
K (mm^3/J)	1.18×10^{-3}	

Initial shear contact stresses are represented dimensionless to the contact size in Figure 85. There is no significant increase of the τ_{zx} stresses towards the contact centre, intended for the present wear process.

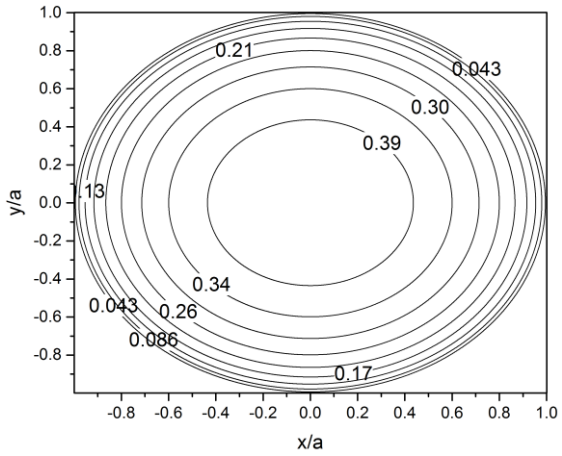

Figure 85 – Isolines for τ_{zx}/p_0 on the surface (Z=0) for the reciprocating sliding (retroactive application, μ=0.428).

The experimental results, displayed in Figure 86, show linear wear trends on both specimens although with dissimilar wear rates. Again, the localized wear variation of the ball will not be evaluated and therefore only for the flat specimens are the wear scar dimensions modelled.

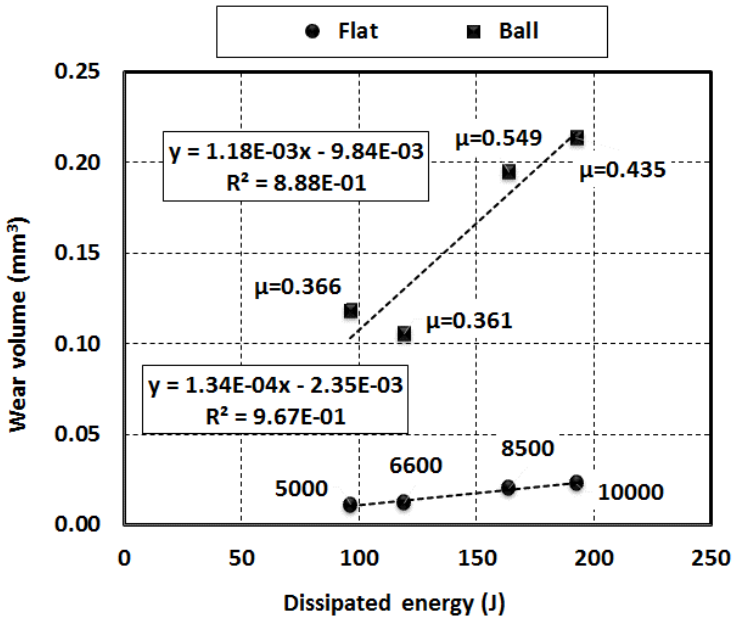

Figure 86 – Friction dissipated energy versus wear volume for the experimental reciprocating sliding tests (retroactive application).

The mean value and standard deviation were obtained by a linearization model described in (Ramalho, 2010), were the wear rate mean and standard deviation for the flat specimens are $k = 1.34 \times 10^{-4} \pm 1.75 \times 10^{-5}$ and for the spherical specimens are $k = 1.18 \times 10^{-3} \pm 2.95 \times 10^{-4}$. Both STD values are at least one order of magnitude lower than the wear rates.

Wear obtained after performing the experimental tests was measured and then compared against the model results, regarding the total wear volume, represented in Table 37.

Table 37 - Reciprocating sliding wear correlation (retroactive application).

Load (N)/Nº Cycles	**Test**	**Wear volume (mm^3)**			
		10			
		5,000	6,600	8,500	10,000
Flat	**Experimental**	$1.13x10^{-2}$	$1.22x10^{-2}$	$2.05x10^{-2}$	$2.31x10^{-2}$
	Model	$1.02x10^{-2}$	$1.17x10^{-2}$	$2.77x10^{-2}$	$2.27x10^{-2}$
	Relative error (%)	-10%	-4%	-14%	-2%
Ball	**Experimental**	$1.18x10^{-1}$	$1.06x10^{-1}$	$1.95x10^{-1}$	$2.14x10^{-1}$
	Model	$1.01x10^{-1}$	$1.14x10^{-1}$	$1.67x10^{-1}$	$2.11x10^{-1}$
	Relative error (%)	-15%	8%	-14%	-1%

The total wear volume presents a very good correlation between experimental and modelled values.

As seen from Figure 87, showing the 2D intermediate sections of both the model and experimental wear scars, the predictions are approximate to the real results, but the borders as well as the scar morphology present some dissimilarities, as can be seen from the results.

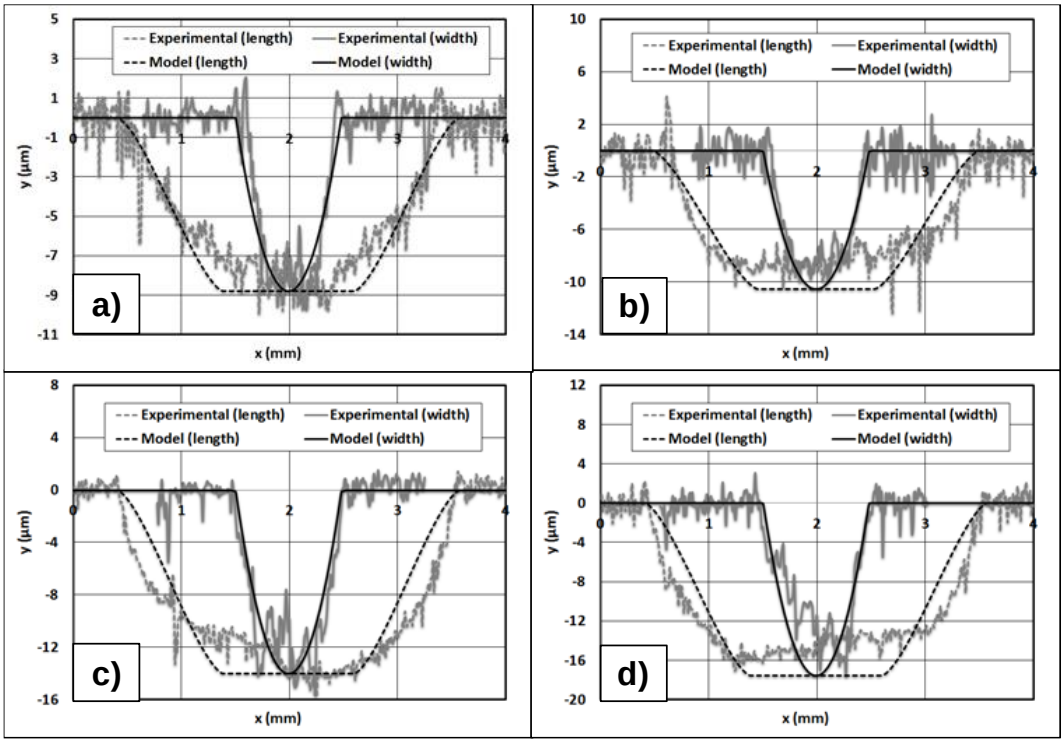

Figure 87 - Reciprocating sliding section comparison (retroactive application) for: a) – 5000 cycles; b) – 6600 cycles; c) – 8500 cycles; d) – 10000 cycles.

A more symmetrical experimental wear scar increases the correlation of the results since the model only relies on geometrical relations to determine wear. This is evident especially in Figure 87 – c).

Regarding the overall performance of the model, the results show acceptable predictions regarding both global and local wear. Also, model performance is detached or alienated from the nature of the contact pair and the test parameters.

5.5.3. Reciprocating fretting

This section features reciprocating fretting validation materials, an AISI 52100 sphere and an AISI M2 flat specimen. In the case of fretting, only the flat surface behaviour is simulated, due specifically to the partial slip condition resulting in wear. The initial shear contact stresses are represented as dimensionless to the contact size in Figure 88. There is no

significant increase of the τ_{zx} stresses towards the contact centre, due to the contact pair nature.

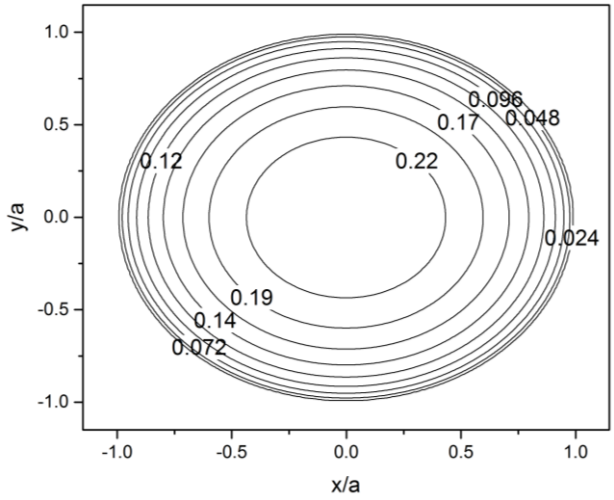

Figure 88 - Isolines for τ_{zx}/p_0 on the surface (Z=0) for fretting (μ=0.24).

Table 38 shows the energy dissipated by friction during all of the tests, modelled and experimental, and a good approximation was found by the method in use. Contrary to the reciprocating tests, the experimental dissipated energy for reciprocating fretting is determined by integration of the fretting loops, and if these are not in a near-perfect representation there is significant deviation, specifically the transition from partial to gross slip plateaus present in the 40 μm displacement test.

Table 38 - Reciprocating fretting energy dissipated by friction correlation.

Displacement (μm)	**Friction dissipated energy (J)**			
	20	40	50	60
Experimental	0.212	0.602	1.706	2.618
Model	0.202	0.670	1.5419	2.414
Relative error (%)	-5%	11%	-10%	-8%

Following are the results of the experimental fretting tests, regarding the flat specimen. Figure 89 – a) displays the wear volumes of each specimen and the global wear coefficient, while Figure 89 – b) shows a typical coefficient of friction evolution, in this case for 60 μm and the one used in the model.

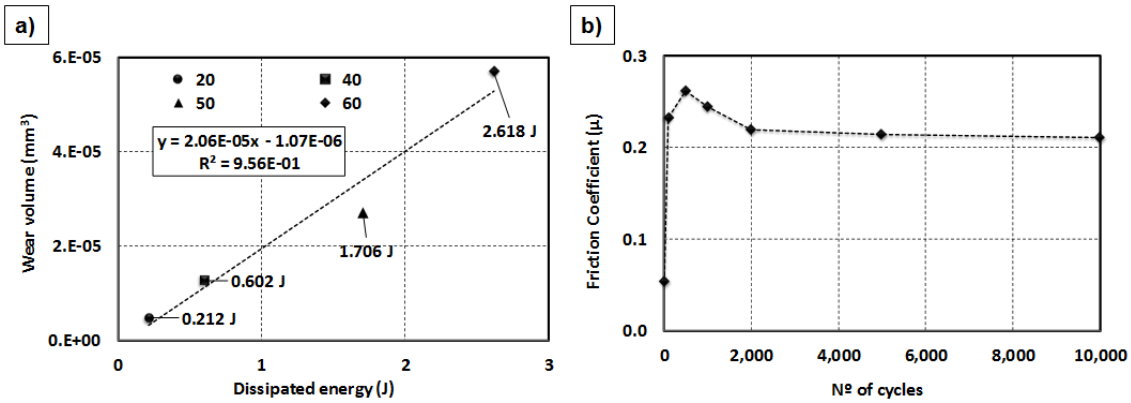

Figure 89 - Friction dissipated energy versus wear volume for the experimental fretting tests (a) and friction coefficient evolution for 60 µm (b).

The wear rate mean and standard deviation are $k = 2.6 \times 10^{-5} \pm 3.12 \times 10^{-6}$, also obtained by a linearization model described in (Ramalho, 2010), within the conditions for validation purposes.

As for the reciprocating fretting model simulations, the energetic wear rate is a relevant input parameter for approximate results. Table 39 shows the correlation between the model and experimental results with a maximum relative error of 16%, making the predictions of the total amount of wear acceptable.

Table 39 - Reciprocating fretting wear correlation.

	Wear volume (mm^3)	Displacement			
		20	40	50	60
Flat	**Experimental**	$4.80x10^{-6}$	$1.27x10^{-5}$	$2.71x10^{-5}$	$5.70x10^{-5}$
	Model	$4.11x10^{-6}$	$1.36x10^{-5}$	$3.14x10^{-5}$	$4.92x10^{-5}$
	Relative error (%)	-14%	7%	16%	-14%

The localized study of the fretting model performance aimed at the analysis of different fretting regimes in order to determine the suitability of a general approach. Partial and gross slip regimes were achieved through imposed displacement variation and the four conditions established. The lowest displacement, 20 µm, was mainly partial slip, the intermediate, 40 µm, was a mixed slip regime and the highest, 50 and 60 µm, mostly gross slip.

Figure 90 displays 3D images of the characteristic wear scars of both the model and experimental results. As seen on the reciprocating sliding, the analysis of model performance

can be achieved by comparing the two space representations as well as the total wear volume, although localized variations are better expressed with 2D section profiles.

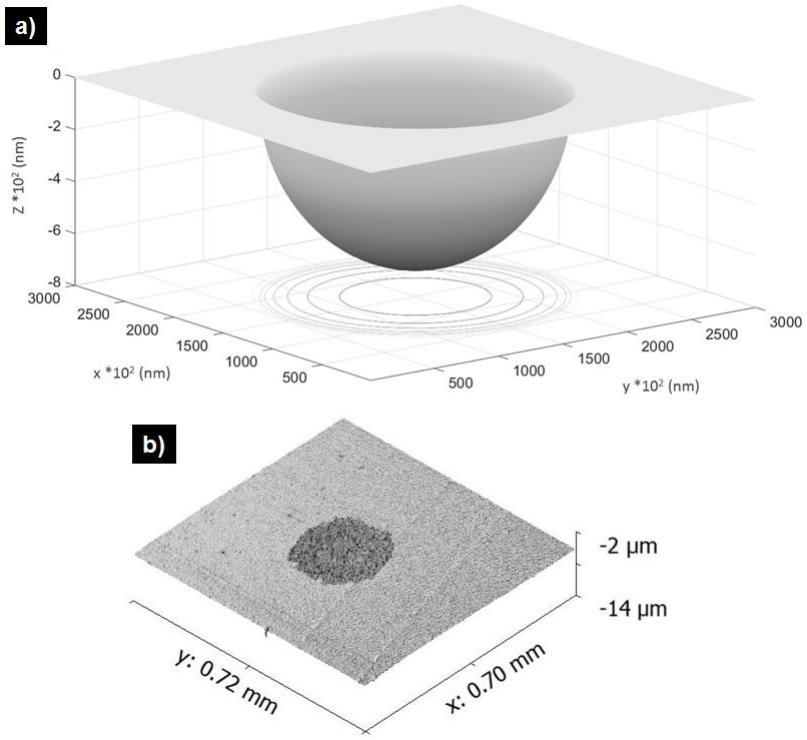

Figure 90 – Reciprocating sliding: a) model 3D representation and b) experimental 3D representation for 10N and 10000 cycles.

Comparing the predictions from friction-dissipated energy against wear, they follow the same tendencies with the exception of the 50 µm test. This is due to the variation in the wear scar and consequent wear volume, observed in Figure 92, as the biggest deviation in the linear tendency. This behaviour is evidenced in Figure 91 – e) and f) with the irregularities in the wear scar, a positive volume, the result of a random wear particle cluster.

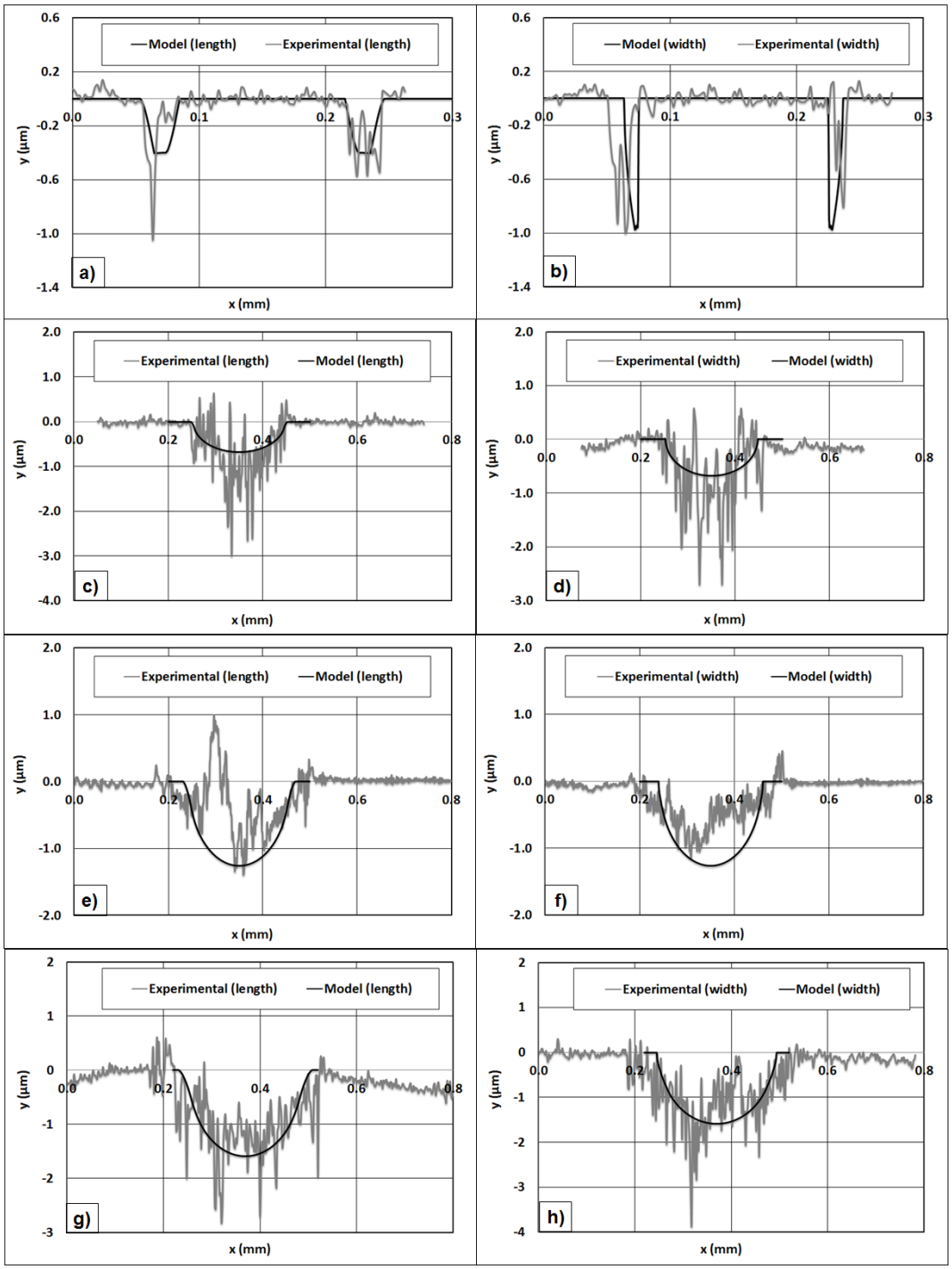

Figure 91 – Fretting section comparison of: a) - 20 µm length; b) - 20 µm width; c) - 40 µm length; d) - 40 µm width; e) - 50 µm length; f) - 50 µm width; g) - 60 µm length; h) - 60 µm width;

The partial slip condition, Figure 91 – a) and b), denoted a doughnut shape, as to be expected, and the location as well as the depth and width are within the predictions of the model. The nature of the more localized energy concentration during this regime is denoted in a maximum depth, even with a low global amount of wear.

A mixed slip regime was identified on the 40 µm, Figure 91 – c) and d), nevertheless the predominant regime was gross slip. Again, the major characteristics of the wear scar were identified, being the depth and width in both directions. Of course, here and in the gross slip regime tests there are irregularities in the scar, due to compacted debris and the proximity of the average detached particles to the surface morphology acquired, which was not obvious in the reciprocating sliding tests.

For the gross slip regime, two conditions were applied, 50 µm and 60 µm. Figure 91 – e) and f) display a good correlation between the model and experiment regarding depth and width. There are still some irregularities on the wear scar, due to agglomerated debris shown in Figure 92, which causes a peak on the experimental 2D profile, higher than the flat surface, and a high variation of wear volume, recorded on the total wear volume in Table 39.

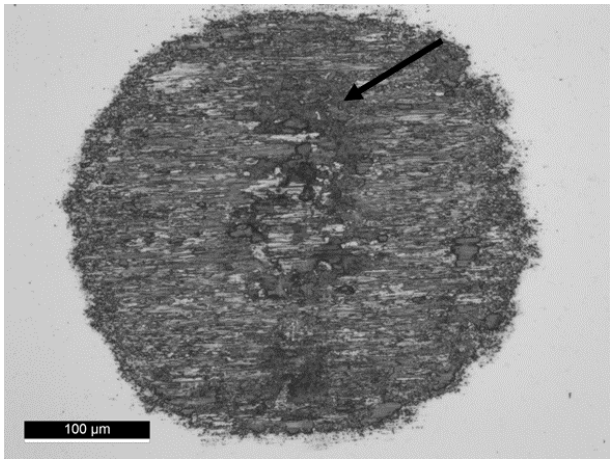

Figure 92 - Fretting of 50 µm flat specimen detail.

The gross slip regime tests, model and experimental, present a more similar average profile than the mixed slip regime, Figure 91 – g) and h), with the presence of some compacted debris formations. Specific scar characteristics such as the depth and widths of wear scars were well identified by the model.

The fretting model's overall performance matched the initial expectations, being primarily the localized wear evaluation and secondly the total wear volume.

5.5.4. Reciprocating Fretting retroactive application

The discretization applied was the same as that presented for the validation tests. The remaining input tests parameters are specified in Table 40.

Table 40 – Fretting input variables.

	Sphere AISI 304	**Flat Specimen AISI 304**
E (GPa)	210	210
υ	0.3	0.3
Initial radius (mm)	5	∞
Normal Load (N)	14	
Duration (cycles)	10,000	
Displacement (µm)	40;50;60	
COF	0.05;0.13;0.29;0.33;0.34;0.35	
K (mm^3/J)	6.295×10^{-5}	

The initial shear contact stresses are represented as dimensionless to the contact size in Figure 93. There is no significant increase of the τ_{zx} stresses towards the contact centre, due to the nature of the contact pair.

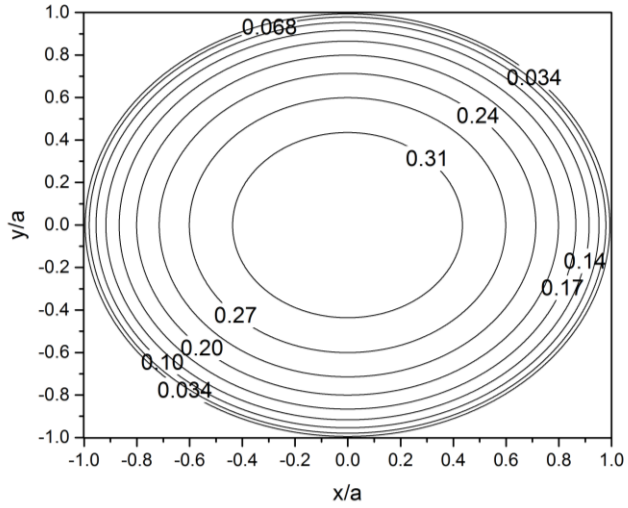

Figure 93 - Isolines for τzx/p0 on the surface (Z=0) for fretting (retroactive application, µ=0.33).

Figure 94 – a) displays the wear volumes of each specimen and the global wear coefficient, and Figure 94 – b) a typical coefficient of friction evolution, in this case for 60 µm and the one used in the model.

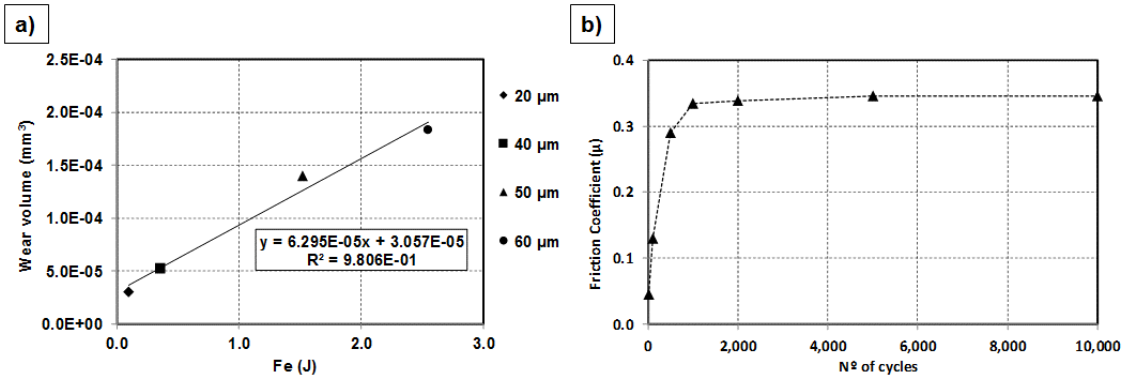

Figure 94 - Friction dissipated energy versus wear volume for the experimental fretting tests (a) and coefficient of friction evolution for 50 µm (b) (retroactive application).

Again, the mean value and standard deviation were obtained by the same linearization model, were the wear rate mean and standard deviation are $k = 6.3 \times 10^{-5} \pm 6.26 \times 10^{-6}$.

Table 41 shows the correlation between the model and experimental results. Due to a high value of the y intercept result of the running-in, almost half the wear rate, the partial-slip condition, 20 µm, was not considered for application.

Table 41 - Reciprocating fretting wear correlation (retroactive application).

	Wear volume (mm^3)	Displacement		
		40	50	60
Flat	**Experimental**	$5.30x10^{-5}$	$1.40x10^{-4}$	$1.83x10^{-4}$
	Model	$4.89x10^{-5}$	$1.09x10^{-4}$	$1.68x10^{-4}$
	Relative error (%)	8%	29%	9%

Figure 95 – a) and b) show the 2D profile comparisons between the experiment and model for 40 µm. Again, the major characteristics of the wear scar were identified, being the depth and width in both directions.

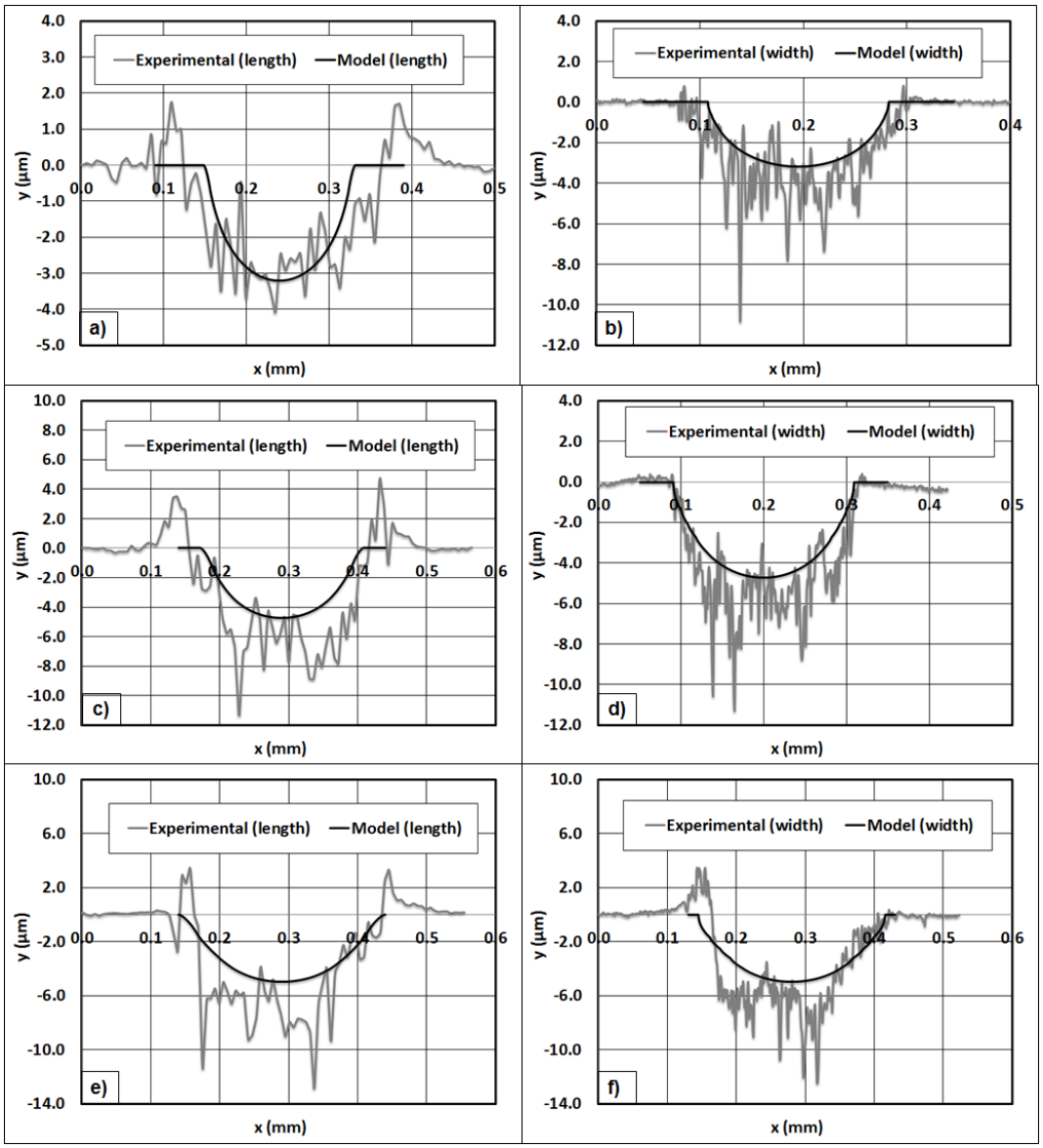

Figure 95 - Fretting section comparison (retroactive application) of: a) - 40 µm length; b) - 40 µm width; c) - 50 µm length; d) - 50 µm width; e) - 60 µm length; f) - 60 µm width.

The 50 µm and 60 µm profiles are compared in Figure 95 – c), d) and Figure 95 – e), f), respectively. There are still some irregularities on the wear scars due to asymmetrical experimental results, recorded on the total wear volume in Table 41, as every specimen presented a significant amount of plastic deformation, as evidenced in Figure 96.

A considerable difference in total wear volume is noted for the 50 µm displacement test, which can be explained by the higher deviation of the wear trend in this condition. Also, this is the only condition where the model result is smaller in every dimension/section.

The overall fretting model performance matched the initial expectations, being primarily the localized wear evaluation and secondly the total wear volume.

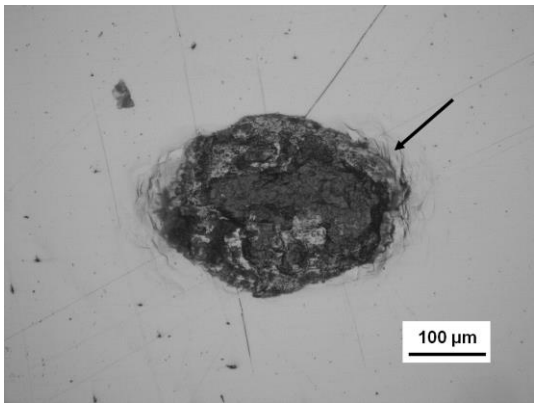

Figure 96 - Fretting of 50 µm flat wear mark (retroactive application).

5.6. BENCHMARK NOTES

In summation, the following premises were achieved:

- A Hertzian normal contact pressure and a friction stress field were used to determine the resulting contact stresses;
- The friction energy dissipated in the contact, resulting from the surface shear stresses applied in the same direction as imposed movement or tangential stresses on the *ZX* defined plane (τ_{zx}), was used to evaluate and determine wear.
- On the reciprocating sliding:
- Full slip regime imposed with decent global and local wear evaluations.
- On the reciprocating fretting:
- Partial slip and gross slip regime discerned and identified. The global and local wear variations were reasonably evaluated with good correlation between the model and experiment.
- The methodology is easy to implement on the model and the amount of input information is slim with just two significant factors, friction coefficient (average) and wear rate (average). Therefore, the model application is fast and reliable.

- The procedure is able to determine limit conditions (dimensions), catalogue performances between samples and produce rapid results for project purposes. The next step is the implementation of binary samples, coatings for example.
- However, unexpected wear irregularities as well as plastic deformation are not considered in the method, since this is an elastic model based on geometric contacts.
- One of the advantages of the wear model is the ability to incorporate a coefficient of friction evolution during the test, when the friction evolution of the contact pair is available.

6. SYNTHESIS AND CONCLUDING REMARKS

This final chapter resumes the significant contributions of the dissertation. The conclusions will be grouped in three sections; with and without electric current contribution and wear model. To further contribute to scientific knowledge, a future endeavour section will also be introduced.

6.1. ON FRETTING WITHOUT ELECTRIC CURRENT

- There is a regime separation through the 50% relative humidity line (linear regression of the 50% RH values). This means that, even with different coefficient of friction variation through the test, the wear volume versus friction-dissipated energy fits a linear evolution very well.
- The two regimes evidenced are low and high relative humidity. Low RH includes the 10% RH test and reducing atmosphere (nitrogen), in both of which the oxidation is reduced or even eliminated, leading to less wear for the same amount of friction-dissipated energy, as shown in the domain below the linear variation line in Figure 44. High RH tests are the 85% RH and the oxidizing atmosphere (oxygen) which promotes oxidation that leads to higher values of wear for the same amount of friction-dissipated energy, as shown in the domain above the linear variation line in Figure 44.

6.2. ON FRETTING WITH ELECTRIC CURRENT

- The introduction of electric current tends to increase the coefficient of friction and the amount of wear volume in the contact, with a significant increase at low current but also with low specific energy dissipated by the Joule effect wear rate.
- The average electric resistance is higher when the current is present due to the increase of oxidation of the wear particles.
- The net contribution of energy dissipated by the Joule effect to wear is three orders of magnitude lower than the friction-dissipated energy contribution.
- A synergetic wear model was presented. The total wear volume results from the summation of the mechanical wear (friction), a joule effect parcel of wear and an incremental factor of degradation due to the combined effect. The incremental factor

acts as a direct addition just by introducing electric current in the contact (equation 12).

- The dispersion and morphology of oxide layer dictates the behaviour on the contact, especially the fretting regime, altering the wear response, electric resistance, and energetic contributions.
- Higher sphere radius increases the resistance during the test, reaching a catastrophic failure quicker (as seen in Figure 54 and Table 23). For the cases studied, the smaller radius had at least 35% lower average impedance than the rest.
- Texturing was mainly to take advantage of blank spaces or dead volume between the sphere and dimple contacts while maintaining a large number of independent contacts.
- It stands out immediately the ability of any textured surface delaying the increase of resistance reaching much lower values during the tests. Comparing with the best non-texturized sample, the improvement of average impedance is at least 50% on any compared case.
- It is clear that beneficial effects can be achieved with both positive (dimples) and negative (hollows) textures. Dense textures can improve the impedance performance registering a decrease of 35% average impedance value. The negative texture can also improve the electric connection performance, with a decrease of 45% of average impedance when compared with the less dense texture, but only in the condition of non-saturation of the contact interface.
- Denser dimple textures tend to maintain lower impedance for a higher amount of time, especially due to the increase in independence of contacts.
- Knowing that they possess a similar contact area, same size sphere, the proximity of the depressions of a denser inverted texture caused the rapid depletion of empty space saturating the contact adding the limiting effect of the nearer depressions as no contact zones.
- The best performance test is a little difficult to identify since both the denser texture test and less dense inverted texture test showed good behaviours. The decisive circumstance would then be the final cycle performance which can indicate a longer test would benefit the denser texture solution.

6.3. WEAR PREDICTION MODEL

- A Hertzian normal contact pressure and a friction stress field were used to determine the resulting contact shear stresses and the resulting friction dissipated energy was used to evaluate wear;
- The model is capable of predicting reciprocating sliding and fretting wear, and their respective regimes, both global and locally;
- The methodology is easy to implement on the model and the amount of input information is slim with just two significant factors, coefficient of friction (average) and wear rate (average). There is also the possibility to implement the Archard's law instead of the energetic approach;
- One of the advantages of the wear model is the ability to incorporate a coefficient of friction evolution during the test, when the friction evolution of the contact pair is available.

6.4. FUTURE ENDEAVOURS

- The next step would be the integration of the synergetic model with the wear model, especially when predicting the total wear volume of contacts with electric current;
- Different texturization techniques, contact parameters and test conditions ought to be added to the study in order to, not only take advantage of these surfaces, but also to introduce improvements;
- Being nickel platted contacts and coin batteries one of the foundations of the work, an obvious evolution will be the characterization of the sole influence of this coating as for the introduction of relevant coating variations;

REFERENCES

Antler, 1985	Antler, M. Survey of Contact Fretting in Electrical Connectors. Components, Hybrids, and Manufacturing Technology, IEEE Transactions. Vol. 8: 87-104. 1985.
Antunes *et al.*, 2003	Antunes, P.V. and Ramalho, A. Study of abrasive resistance of composites for dental restoration by ball-cratering. Wear. Vol. 255: 990–998. 2003.
Antunes *et al.*, 2014	Antunes, P.V., Ramalho, A. and Carrilho, E.V.P. Mechanical and wear behaviours of nano and microfilled polymeric composite: Effect of filler fraction and size. Materials & Design. Vol.: 61: 50–60, September 2014.
Archard, 1953	Archard, J.F. Contact and rubbing of flat surfaces. Journal of Applied Physics. Vol. 24: 981. 1953.
Baets *et al.*, 1998	Baets, P., Kalacska, G., Strijckmans, K., Van de Velde, F. and Van Peteghem, A.P. Experimental study by means of thin layer activation of the humidity influence on the fretting wear of steel surfaces. Wear. Vol. 216: 131-137. 1998.
Bhushan, 2001	Bhushan, Bharat. Modern Tribology Handbook, Volume One, Principles of Tribology. CRC Press LLC. 2001.
Bishop & Associates Inc., 2012	Bishop & Associates Inc. Data Report.
Blau P.J., 2004	Blau, P., J. On the nature of running-in. Tribology International, Vol. 38: 1007-1012. 2004.
Blau, 2004	Blau, P., J. (Ed.), ASM Handbook. Friction, Lubrication and Wear Technology. Vol. 18 ASM, Materials Park, Ohio, USA, 2004.
Braun *et al.*, 2014	Braun, D., Greiner, C., Schneider, J. and Gumbsch, P. Efficiency of laser surface texturing in the reduction of friction under mixed lubrication. Tribology International. Vol. 77: 142–147. 2014.
Cai *et al.*, 2009	Cai, Z., Zhu, M., Zheng, J., Jin, X. and Zhou, Z. Torsional fretting behaviors of LZ50 steel in air and nitrogen. Tribology International. Vol. 42. 1676-1683. 2009.
Cai *et al.*, 2009	Cai, Z., Zhu, M., Shen, H. Zhou, Z. and Jin, X. Torsional fretting wear behaviour of 7075 aluminium alloy in various relative humidity environments. Wear. Vol. 267: 330-339. 2009.
CarMD Corp., 2012	CarMD Corp. Data Report.
Chaudhry *et al.*, 2013	Chaudhry, V. and Kailas, S.V. Damage quantification under sliding and seizure condition using first-of-a-kind fretting machine. Wear. Vol. 305: 140-154.2013.
Chaudhry *et al.*, 2013	Chaudhry, V. and Kailas, S.V. Fretting studies on self-mated stainless steel and chromium carbide coated surfaces under controlled environment conditions. Wear. Vol. 301: 524-539. 2013.
Chaudhry et al., 2014	Chaudhry, V., Simha, K.R.Y. and Kailas, S.V. Energy based approach for the evaluation of damage under partial slip and gross sliding condition. Wear, Vol. 315: 115-124. 2014.

Chen *et al.*, 2001 — Chen, R. Iwabuchi, A. and Shimizu, T. Effects of ambient pressure on fretting friction and wear behavior between SUS 304 steels. Wear. Vol. 249: 379-388. 2001.

Chen *et al.*, 2002 — Chen, H., Wu, P.Q., Quaeyhaegens, C., Xu, K.W., Stals, L.M., He, J.W. and Celis, J.P. Comparison of fretting wear of Cr-rich CrN and TiN coatings in air of different relative humidities. Wear. Vol. 253. 527-532. 2002.

Cruzado et al., 2012 — Cruzado, A., Urchegui, M.A., Gómez, X. Finite element modelling and experimental validation of fretting wear scars in thin steel wires. Wear, Vol. 289: 26-38. 2012.

de Wit *et al.*, 1998 — de Wit, E., Blanpain, B., Froyen, L. and Celis, J.P. The tribochemical behaviour of TiN-coatings during fretting wear. Wear. Vol. 217: 215-224. 1998.

English et al., 2015 — English, R. Ashkanfar, A. and Rothwell, G. A computational approach to fretting wear prediction at the head–stem taper junction of total hip replacements. Wear, Vol. 338-339: 210-220. 2015.

Esteves *et al.*, 2013 — Esteves, M., Ramalho, A., Ferreira, J. A. M. and Nobre, J. P. Tribological and Mechanical Behaviour of Epoxy/Nanoclay Composites. Tribology Letters. Vol.:52, Issue 1: 1-10. October 2013.

Esteves *et al.*, 2015 — Esteves, M., Ramalho, A. and Ramos, F. Fretting behaviour of the AISI 304 stainless steel under different atmosphere environments. Tribology International, Vol. 88,: 56-65. 2015.

Farrahi *et al.*, 1992 — Farrahi, G. H. and Maeder, G. An experimental study of fretting by means of x-ray diffraction. Fatigue & Fracture of Engineering Materials & Structures, Vol. 15: 1, 91-102, 1992.

Fernandes *et al.*, 2015 — Fernandes, F., Polcar, T., Loureiro, A. and Cavaleiro, A. Effect of the substrate dilution on the room and high temperature tribological behaviour of Ni-based coatings deposited by PTA on grey cast iron. Surface & Coatings Technology, Vol. 281: 11-19. 2015.

Fernández *et al.*, 2016 — Fernández, S., de Abril, O., Naranjo, F.B. and Gandía, J.J. High quality textured ZnO:Al surfaces obtained by a two-step wet-chemical etching method for applications in thin film silicon solar cells. Solar Energy Materials and Solar Cells. Vol. 78: 140–147. 2016.

Fouvry *et al.*, 1995 — Fouvry, S., Kapsa, Ph. and Vincent, L. Analysis of sliding behaviour for fretting loadings: determination of transition criteria. Wear. Vol. 185: 35-46. 1995.

Fouvry *et al.*, 1996 — Fouvry, S., Kapsa, Ph. and Vincent, L. Quantification of fretting damage. Wear. Vol. 200: 186-205. 1996.

Fouvry *et al.*, 2001 — Fouvry, S. and Kapsa, Ph. An energy description of hard coating wear mechanisms. Surface and Coatings Technology. Vol. 138: 141-148. 2001.

Fouvry *et al.*, 2003 — Fouvry, S., Liskiewicz, T., Kapsa, Ph., Hannel, S. and Sauger, E. An energy description of wear mechanisms and its applications to oscillating sliding contacts. Wear. Vol. 255: 287-298. 2003.

Fouvry *et al.*, 2006 — Fouvry, S., Fridrici, V., Langlade, C., Kapsa, Ph. and Vincent, L. Palliatives in fretting: A dynamical approach. Tribology International. Vol. 39: 1005-1015. 2006.

Fouvry *et al.*, 2011 — Fouvry, S., Jedrzejczyk, P. and Chalandon, P. Introduction of an exponential formulation to quantify the electrical endurance of micro-

contacts enduring fretting wear: Application to Sn, Ag and Au coatings. Wear. Vol. 271: 1524-1534. 2011.

Fu *et al.*, 2000 — Fu, Y., Wei, J. and Batchelor, A. W. Some considerations on the mitigation of fretting damage by the application of surface-modification technologies. Journal of Materials Processing Technology. Vol. 99: 231-245. 2000.

Garcin et al., 2015 — Garcin, S., Fouvry, S. and Heredia, S. A FEM fretting map modelling: Effect of surface wear on crack nucleation. Wear, Vol. 330-331: 145-159. 2015.

Ghosh *et al.*, 2013 — Ghosh, A., Leonard, B. and Sadeghi, F. A stress based damage mechanics model to simulate fretting wear of Hertzian line contact in partial slip. Wear. Vol. 307: 87-99. 2013.

Goto *et al.*, 1984 — Goto, H. and Buckley, D. H. Effect of humidity on fretting wear of several pure metals. NASA Technical Paper 2403. 1984.

Hamilton et al., 1966 — Hamilton, G. M. and Goodman, L. E. The Stress Field Created by a Circular Sliding Contact. Journal of Applied Mechanics, vol. 33, issue 2, pp. 371-376. 1966.

Hamilton et al., 1983 — Hamilton, G. M. Explicit Equations for the Stresses beneath a Sliding Spherical Contact. Proceedings of the Institution of Mechanical Engineers, Part C: Journal of Mechanical Engineering Science. Vol. 197 Issue 1: 53-59. January 1983.

Hanief et al., 2015 — Hanief, M. and Wani, M.F. Modelling and prediction of surface roughness for running-in wear using Gauss-Newton algorithm and ANN. Applied Surface Science Vol. 357:1573-1577. 2015.

Hannel *et al.*, 2001 — Hannel, S., Fouvry, S., Kapsa, Ph. and Vincent, L. The fretting sliding transition as a criterion for electrical contact performance. Wear. Vol. 249: 761-770. 2001.

Hirsch *et al.*, 2013 — Hirsch, M.R. and Neu, R.W. Influence of temperature on the fretting response between AISI 301 stainless steel and AISI 52100 steel. Tribology International. Vol. 68: 77-84. 2013.

Hua *et al.*, 2016 — Hua, X., Sun, J., Zhang, P., Ge, H., Yonghong, F., Jinghu, J. and Yin, B. Research on discriminating partition laser surface micro-texturing technology of engine cylinder. Tribology International. Vol. 98: 190–196. 2016.

Huq *et al.*, 1999 — Huq, M.Z. and Celis, J.P. Fretting wear of multilayered (Ti,Al)N/TiN coatings in air of different relative humidity. Wear. Vol. 225-229: 53-64. 1999.

Hurricks, 1970 — Hurricks, P.L. The mechanism of fretting – a review. Wear. Vol. 15: 389-409. 1970.

Jedrzejczyk *et al.*, 2009 — Jedrzejczyk, P., Fouvry, S. and Chalandon, P. A fast methodology to quantify electrical-contact behaviour under fretting loading conditions. Wear. Vol. 267: 1731-1740. 2009.

Johnson, 1985 — Johnson, K. L. Contact Mechanic. Cambridge University Press. 1985.

Kapsa *et al.*, 2005 — Kapsa, P., Fouvry, S. and Vincent, L. Basic Principles of Fretting. Wear – Materials, Mechanisms and Practice (Gwidon W. Stachowiak). John Wiley & Sons Ltd. 2005.

Kasarekar et al., 2007	Kasarekar, Aditya T., Bolander, Nathan W., Sadeghi, F. and Tseregounis, S. Modelling of fretting wear evolution in rough circular contacts in partial slip. International Journal of Mechanical Sciences, Vol. 49: 690-703. 2007.
Kato, 2000	Kato, K. Wear in relation to friction - a review. Wear. Vol. 241. 151-157. 2000.
Kato, 2002	Kato, K. Journal of Engineering Tribology – Proceedings Part J, 2002, Vol. 216, No. J6, ISSN 1350–6501.
Kim *et al.*, 2010	Kim, K. and Korsunsky, A.M. Dissipated energy and fretting damage in CoCrAlY-MoS2 coatings. Tribology International. Vol. 43: 676-684. 2010.
Klaffke *et al.*, 1998	Klaffke, D. and Skopp, A. Are thin hard coatings (TiN, DLC, diamond) beneficial in tribologically stressed vibrational contacts?-Effects of operational parameters and relative humidity. Surface and Coatings Technology. Vol. 98: 953-961. 1998.
Klaffke, 1995	Klaffke, D. On the repeatability of friction and wear results and on the influence of humidity in oscillating sliding tests of steel-steel pairings. Wear. Vol. 189: 117-121. 1995.
Korsunsky *et al.*, 2010	Korsunsky, A.M. and Kim, K. Dissipated energy and friction coefficient evolution during fretting wear of solid lubricant coatings. Tribology International. Vol. 43: 861-867. 2010.
Kubiak *et al.*, 2010	Kubiak, K.J., Mathia, T.G. and Fouvry, S. Interface roughness effect on friction map under fretting contact conditions. Tribology International. Vol. 43: 1500-1507. 2010.
Laporte *et al.*, 2014	Laporte, J., Perrinet, O. and Fouvry, S. Prediction of the electrical contact resistance endurance of silver-plated coatings subject to fretting wear, using a friction energy density approach. Wear. In Press, Corrected Proof. doi:10.1016/j.wear.2014.12.006.
Li *et al.*, 2011	Li, L., Etsion, I. and Talke, F.E. The effect of frequency on fretting in a micro-spherical contact. Wear. Vol. 270: 857-865. 2011.
Mattei et al., 2015	Mattei, L. and Di Puccio, F. Influence of the wear partition factor on wear evolution modelling of sliding surfaces. International Journal of Mechanical Sciences, Vol. 99:72-88. 2015.
McColl et al., 2004	McColl, I.R., Ding, J. and Leen, S.B. Finite element simulation and experimental validation of fretting wear. Wear, Vol. 256: 1114-1127. 2004.
Mindlin, 1949	Mindlin, R. D. Compliance of elastic bodies in contact. Journal of Applied Mechanics, vol. 16, 259-268. 1949.
Miranda *et al.*, 2014	Miranda, J.C. and Ramalho, A. Study of the effects of damage accumulation on wear. Wear, vol. 330-331, 79-84. 2015.
Mischler, 2008	Mischler, S. Triboelectrochemical techniques and interpretation methods in tribocorrosion: A comparative evaluation. Tribology International, Vol. 41, Issue 7: 573-583. July 2008.
Mohrbacher *et al.*, 1995	Mohrbacher, H., Blanpain, B., Celis, J.P., Roos, J.R., Stals, L. and Van Stappen, M. Oxidational wear of TIN coatings on tool steel and nitrided tool steel in unlubricated fretting. Wear. Vol. 188: 130-137. 1995.
Nachez *et al.*, 2006	Nachez, L., Gómez, B.J., Ferrón, J. and Feugeas, J. Surface modification of austenitic stainless steel on the surface of electric contact during low frequency current circulation. Thin Solid Films. Vol. 513: 206-211. 2006.

Pearson *et al.*, 2013	Pearson, S.R., Shipway, P.H., Abere, J.O. and Hewitt, R.A.A. The effect of temperature on wear and friction of a high strength steel in fretting. Wear. Vol. 303:622-631. 2013.
Prieto-López *et al.*, 2016	Prieto-López, L.O. and Williams, J.A. Switchable Adhesion Surfaces with Enhanced Performance Against Rough Counterfaces. Biomimetics. Micro- and Nano-Structured Bio-Inspired Surfaces. 1(1) 2. 2016.
Quinn, 1992	Quinn, T., F., J. Oxidational Wear Modelling: I. Wear. Vol. 153: 179-200. 15, March 1992.
Quinn, 1994	Quinn, T., F., J. Oxidational Wear Modelling Part II: The general theory of oxidational wear. Wear. Vol. 175: 199-208. June 1994.
Quinn, 1998	Quinn, T., F., J. Oxidational Wear Modelling Part III: The Effects of Speed and Elevated Temperatures. Wear. Vol. 216: 262-275. 1, April 1998.
Ramalho *et al.*, 2003	Ramalho, A. and Celis, J.-P. Fretting laboratory tests: Analysis of the mechanical response of test rigs. Tribology Letters. Vol. 14, No. 3, April 2003.
Ramalho *et al.*, 2006	Ramalho, A. and Miranda, J.C. The relationship between wear and dissipated energy in sliding systems. Wear, vol. 260, 361-367. 2006.
Ramalho, 2010	Ramalho, A. A reliability model for friction and wear experimental data. Wear. Vol. 269:, Issues 3-4: 213-223. June 2010.
Raman *et al.*, 2007	Raman, S.G.S. and Jayaprakash, M. Influence of plasma nitriding on plain fatigue and fretting fatigue behavior of AISI 304 austenitic stainless steel. Surface & Coatings Technology. Vol. 201: 5906-5911. 2007.
Ren *et al.*, 2014	Ren, W., Perrinet, P., Song, J. and Zhai, G. Effects of current load on wear and fretting corrosion of gold-plated electrical contacts. Tribology International. Vol. 70:75-82. 2014.
Ren *et al.*, 2015	Ren, W., Wang, P., Fu, Y., Pan, C. and Song, J. Effects of temperature on fretting corrosion behaviors of gold-plated copper alloy electrical contacts. Tribology International. Vol. 83: 1-11. 2015.
Rybiak *et al.*, 2010	Rybiak, R., Fouvry, S. and Bonnet, B. Fretting wear of stainless steels under variable temperature conditions: Introduction of a 'composite' wear law. Wear. Vol. 268: 413-423. 2010.
Sauger *et al.*, 2000	Sauger, E., Fouvry, S., Ponsonnet, L., Kapsa, Ph., Martin, J.M. and Vincent, L. Tribologically transformed structure in fretting. Wear. Vol. 245: 39-52. 2000.
Schouterden *et al.*, 1995	Schouterden, K., Blanpain, B., Celis , J.P. and Vingsbo O. Fretting of titanium nitride and diamond-like carbon coatings at high frequencies and low amplitude. Wear. Vol. 181-183: 86-93. 1995.
Slade, 2014	Slade, P. G. Electrical Contacts: Principles and Applications, Second edition. pp. 441-481. CRC Press LLC, 2014. Boca Raton.
Suh, 1978	Suh, N.P. The delamination theory of wear. Wear. Vol. 44: 1. 1978.
Trinh *et al.*, 2015	Trinh, K.E., Tsipenyuk, A., Varenberg, M., Rosenkranz, A., Souza, N. and Mücklich, F. Wear debris and electrical resistance in textured Sn-coated Cu contacts subjected to fretting. Wear. Vol. 344–345: 86–98. 2015.
van Dijk *et al.*, 2008	van Dijk, P., Kassman Rudolphi, Å. and Klaffke, D. Investigations on electrical contacts subjected to fretting motion. 21st International Conference on Electrical Contacts, Zurich, 2008.

Vander Voort *et al.*, 2004	Vander Voort, G.F. (Ed.), ASM Handbook. Metallography and Microstructures, vol. 9, ASM, Materials Park, Ohio, 2004.
Vilhena *et al.*, 2009	Vilhena, L.M., Sedlaček, M., Podgornik, B., Vižintin, J., Babnik, A. and Možina, J. Surface texturing by pulsed Nd:YAG laser. Tribology International. Vol. 42 Issue 10: 1496–1504. 2009.
Wang *et al.*, 2015	Wang, X., Giovannini, M., Xing, Y., Kang, M. and Ehmann, K. Fabrication and tribological behaviors of corner-cube-like dimple arrays produced by laser surface texturing on medical needles. Tribology International. Vol. 92: 553–558. 2015.
Wang *et al.*, 2016	Wang, Z., Wang, C., Wang, M. and Zhao, Q. Manipulation of tribological properties of stainless steel by picosecond laser texturing and quenching. Tribology International. Vol. 99: 14–22. 2016.
Woo Park *et al.*, 2009	Woo Park, Y., Ramesh Bapu, G.N.K. and Yong Lee, K. The influence of current load on fretting of electrical contacts. Tribology International. Vol. 42: 682-689. 2009.
Yilbas *et al.*, 2016	Yilbas, B.S. and Ali, H. Laser texturing of Hastelloy C276 alloy surface for improved hydrophobicity and friction coefficient. Optics and Lasers in Engineering. Vol. 78: 140–147. 2016.
Yousfi *et al.*, 2016	Yousfi, M., Mezghani, S., Demirci, I. and El Mansori, M. Tribological performances of elliptic and circular texture patterns produced by innovative honing process. Tribology International. Vol. 100: 255–262. 2016.
Zhang et al., 2015	Zhang, X., Shen, H, Liu, J., Deng, S., Li, X., Cai, Z. and Zhu, M. An efficient numerical model for predicting the torsional fretting wear considering real rough surface. Wear, Vol. 344-345: 32-45. 2015.
Zhou *et al.*, 2006	Zhou, Z. R., Nakazawa, K., Zhu, M. H., Maruyama, N., Kapsa, Ph and Vincent, L. Progress in fretting maps. Tribology International. Vol. 39(10): 1068-1073. 2006.
Zhu *et al.*, 2001	Zhu, M. H., Zhou, Z. R., Kapsa, Ph. and Vincent, L. An experimental investigation on composite fretting mode. Tribology International. Vol. 34(11): 733-738. 2001.
Zhu *et al.*,2011	Zhu, M. H. and Zhou, Z. R. On the mechanisms of various fretting wear modes. Tribology International. Vol. 44: 1378-1388. 2011.

ANNEX A

The following equations define the hertz contact dimensions and pressure:

$$\gamma = \left(\frac{((1-(\upsilon_1)^2)}{E_1}\right) + \left(\frac{((1-(\upsilon_2)^2)}{E_2}\right) \quad (1)$$

$$a = \left(\left(\frac{3}{4}\right) \times P \times \left(\frac{1}{(1/R_1)+(1/R_2)}\right) \times \gamma\right)^{(1/3)} \quad (2)$$

$$p_0 = \frac{(3P)}{(2\pi \times a^2)} \quad (3)$$

$$q_0 = \mu \times p_0 \quad (4)$$

$$r = (X^2 + Y^2)^{1/2} \quad (5)$$

The stress distribution is the result of a constant normal load *P*, alongside the *Z* axis, and an oscillating tangent load *Q*, coincident with the *X* axis, representing the friction force. Since the model uses the surface dissipated energy in the contact, friction dissipated energy, there is only the need to determine the general stress field for *Z=0*, which translates as the surface plane where the contact between the two specimens is established.

Hertz stress field distribution is due to the normal load and it's presented for the principal stresses on the contact plane (Z=0).

Hertz Stress Field

σ_x on the contact plain (Z=0):

$$\sigma_x = \left(\frac{p_0}{a}\right) \times \left(-a \times (1 + \upsilon_1) + \left(\frac{a}{2}\right)\right) \qquad r=0 \quad (6)$$

$$\sigma_x = \left(\frac{p_0}{a}\right) \times \left(\frac{(1-2\upsilon_1)\times(X^2-Y^2)\times a^3}{3r^4}\right) \qquad r\geq a \quad (7)$$

$$\sigma_x = \left(\frac{p_0}{a}\right) \times \left(\left(\frac{1}{r^2}\right) \times \left(\frac{X^2 - Y^2}{r^2}\right) \times \left(\frac{1 - 2\upsilon_1}{3} \times \left((a^2 - r^2)^{3/2} - a^3\right)\right) - (X^2 + 2\upsilon_1 \times Y^2) \times (a^2 - r^2)^{1/2}\right) \qquad r<a \quad (8)$$

σ_y on the contact plain (Z=0):

$$\sigma_y = \left(\frac{p_0}{a}\right) \times \left(-a \times (1 + \upsilon_1) + \left(\frac{a}{2}\right)\right) \qquad r=0 \quad (9)$$

$$\sigma_y = \left(\frac{p_0}{a}\right) \times \left(\frac{(1-2\upsilon_1)\times(Y^2-X^2)\times a^3}{3r^4}\right) \qquad r\geq a \quad (10)$$

$$\sigma_y = \left(\frac{p_0}{a}\right) \times \left(\left(\frac{1}{r^2}\right) \times \left(\frac{X^2 - Y^2}{r^2}\right) \times \left(\frac{1 - 2\upsilon_1}{3} \times \left((a^2 - r^2)^{3/2} - a^3\right)\right) - (Y^2 + 2\upsilon_1 \times X^2) \times (a^2 - r^2)^{1/2}\right) \qquad r<a \quad (11)$$

σ_z on the contact plain (Z=0):

$$\sigma_z = \left(\frac{p_0}{a}\right) \times (-a) \qquad r=0 \quad (12)$$

$$\sigma_z = 0 \qquad r \geq a \quad (13)$$

$$\sigma_z = -\left(\frac{p_0}{a}\right) \times \left(1 - \left(\frac{r}{a}\right)^2\right)^{1/2} \qquad r<0 \quad (14)$$

τ_{xy} on the contact plain (Z=0):

$$\tau_{xy} = 0 \qquad r=0 \quad (15)$$

$$\tau_{xy} = \left(\frac{p_0}{a}\right) \times \left(\frac{(1-2\upsilon_1)\times X\times Y\times 2a^3}{3r^4}\right) \qquad r \geq a \quad (16)$$

$$\tau_{xy} = -\left(\frac{p_0}{a}\right) \times \left(\frac{(1-2\upsilon_1)\times X\times Y}{r^4} \times \frac{2a^3}{3}\right) \qquad r<a \quad (17)$$

The friction stress field distribution is due to the tangential load and it's presented for the principal stresses on the contact plane (Z=0).

Friction Stress Field

σ_x on the contact plain (Z=0):

$$\sigma_x = 0 \qquad r=0 \quad (18)$$

$$\sigma_x = \left(\frac{q_0}{a}\right) \times \left(-X\left(1 + \frac{\upsilon_1}{4}\right) \times \left(\tan^{-1} \frac{a}{(r^2 - a^2)^{1/2}} \right) + \left(\frac{a \times X \times (r^2 - a^2)^{1/2}}{r^4} \right) \times \left(-\upsilon_1 \times (r^2 - a^2) \times \left(\frac{3}{2} - \frac{2X^2}{r^2} \right) + \frac{7\upsilon_1 \times r^2}{4} - 2\upsilon_1 \times X^2 + r^2 \right) \right) \qquad r>a \quad (19)$$

$$\sigma_x = \left(\frac{q_0}{a}\right) \times \left(-\frac{\pi \times X}{2} \times \frac{\upsilon_1}{4} + 1 \right) \qquad r \leq a \quad (20)$$

σ_y on the contact plain (Z=0):

$$\sigma_y = 0 \qquad r=0 \quad (21)$$

$$\sigma_y = \left(\frac{q_0}{a}\right) \times \left(-\frac{3}{4} X \times \upsilon_1 \times \left(\tan^{-1} \frac{a}{(r^2 - a^2)^{1/2}} \right) + \left(\frac{a \times X \times (r^2 - a^2)^{1/2}}{r^4} \right) \times \left(-\upsilon_1 \times a^2 \times \left(\frac{1}{2} - \frac{2Y^2}{r^2} \right) + \left(\frac{3}{4} \upsilon_1 \times r^2 \right) \right) \right) \quad r>a \quad (22)$$

$$\sigma_x = \left(\frac{q_0}{a}\right) \times \left(-\frac{3\pi \times \upsilon_1 \times X}{8} \right) \quad r \leq a \quad (23)$$

σ_z on the contact plain (Z=0):

$$\sigma_z = 0 \quad r=0 \quad (24)$$

$$\sigma_z = 0 \quad r>a \quad (25)$$

$$\sigma_z = 0 \quad r \leq a \quad (26)$$

τ_{zx} on the contact plain (Z=0):

$$\tau_{zx} = \left(\frac{q_0}{a}\right) \times (-a) \quad r=0 \quad (27)$$

$$\tau_{zx} = 0 \quad r>a \quad (28)$$

$$\tau_{zx} = \left(\frac{q_0}{a}\right) \times \left(-(a^2 - r^2)^{1/2} \right) \quad r \leq a \quad (29)$$

τ_{xy} on the contact plain (Z=0):

$$\tau_{xy} = 0 \qquad r=0 \quad (30)$$

$$\tau_{xy} = \left(\frac{q_0}{a}\right) \times \left(\frac{Y}{2} \times \left(\frac{\upsilon_1}{2} - 1\right) \times \tan^{-1}\left(\frac{a}{(r^2 - a^2)^{1/2}}\right) + \left(\frac{a \times Y \times (r^2 - a^2)^{1/2}}{r^4}\right) \times \left(-\upsilon_1 \times (r^2 - a^2) \times \left(\frac{1}{2} - \frac{2X^2}{r^2}\right) - 2\upsilon_1 \times X^2 + \upsilon_1 \times \frac{r^2}{4} + \frac{r^2}{2}\right)\right) \qquad r>a \quad (31)$$

$$\tau_{xy} = \left(\frac{q_0}{a}\right) \times \left(\frac{\pi \times Y}{4} \times \frac{\upsilon_1}{2} - 1\right) \qquad r \leq a \quad (32)$$

The contact of a sphere/cylindrical race geometry is represented by the following equations:

$$R_{eq} = \frac{R_1' \times R_2'}{2R_1' - R_2'} \quad (33)$$

$$A = \frac{\frac{1}{R_1'} - \frac{1}{R_2'}}{2} \quad (34)$$

$$B = \frac{1}{2R_1'} \quad (35)$$

Where R'_1 and R'_2 stand for the modified sphere and surface radius, respectively. The main difference is the introduction of a cylindrical race instead of flat surface.

$$n_a = 0.9739 \times \left(\frac{A}{B}\right)^{-0.392} \quad (36)$$

$$n_b = 0.9351 \times \left(\frac{A}{B}\right)^{0.2323} \quad (37)$$

$$a_1 = 1.145 \times n_a \times (P \times K' \times \gamma)^{1/3} \quad (38)$$

$$a_2 = 1.145 \times n_b \times (P \times K' \times \gamma)^{1/3} \quad (39)$$

$$a' = \frac{a_1 + a_2}{2} \quad (40)$$